DEVELOPMENT OF A NEAR-INFRARED PHOTOMETER FOR EARLY DETECTION OF TISSUE DISTRESS AT ANATOMICAL SITES PRONE TO PRESSURE ULCER

LUI KA HIM MICHAEL

M.Phil

The Hong Kong

Polytechnic University

2012

The Hong Kong Polytechnic University
Interdisciplinary Division of
Biomedical Engineering

Development of a Near-infrared Photometer for Early Detection of Tissue Distress at Anatomical Sites Prone to Pressure Ulcer

LUI KA HIM MICHAEL

A thesis submitted in partial fulfillment of
the requirements for the degree of
Master of Philosophy

December 2011

CERTIFICATE OF ORIGINALITY

I hereby declare that this thesis is my own work and that, to the best of my knowledge and belief, it reproduces no material previously published or written, nor material that has been accepted for the award of any other degree or diploma, except due acknowledgement has been made in the text.

_____(signed)

LUI Ka Him Michael (Name of student)

Abstract

Pressure ulcer increases the hospitalization time of non-ambulatory patients and induces heavy financial burden to health care institutions. To prevent the onset of pressure ulcer, clinicians rely on the measurements of skin blood flow and skin oxygenation to monitor the weight-bearing tissues. However, these assessment methods can only reveal the conditions of superficial tissues. Near infrared (NIR) spectroscopy has the potential to measure tissue oxygenation up to several centimeters below the skin surface. In this work, we developed a spatially resolved NIR photometer (λ = 690 and 830 nm) for tissue viability assessment. To ensure the applicability of the spatially resolved method, we examined the consistency of the linear relationship between the transport scattering coefficients $\left(\mu_s'(\lambda)\right)$ and wavelengths (λ) among subjects at the greater trochanter region (a common site for pressure ulcer). Our result showed that the inter-subject variation was 8.3% in 11 subjects which was lower than other reported results at different anatomical sites. This confirmed the consistency of wavelength dependence of $\mu_s'(\lambda)$ in the greater trochanter region among subjects and thus the spatially resolved method is suitable for use in tissue oxygenation measurements at the greater trochanter region. To validate our NIR photometer, a blood-Intralipid tissue phantom was developed. *In vitro* oxygen saturation measurements were conducted using this phantom and compared with results obtained from a commercially available blood gas analyzer. The result showed a high correlation (r^2 = 0.9718) between the measurements by

the two systems. The average tissue oxygen saturation measured by using our NIR photometer in healthy subjects' forearm was 71.4 ± 14.0%. This value was comparable to those measured by other NIR spectroscopic systems under similar conditions (63.9% to 72.1%). During passive exercise of the forearm muscle by continuous electrical stimulation, tissue oxygenation in the targeted muscle was found to decrease by 10.5 ± 5.4% of its resting values. Due to the limited power output of the laser system, the penetration depth of our NIR photometer was estimated to be 3.4 mm, which was much less than other commercial NIR spectroscopic systems. Further improvements have to be made to increase the penetration depth of our NIR photometer before it can be applied to assess the oxygenation of deep tissues that are prone to pressure ulcer.

Publications arising from the thesis

1. Lui MKH, Tam EWC. The use of spatially resolved near infrared spectroscopy in examination of tissue oxygenation in human finger. Proceedings of BME, Hong Kong, 2010. p. H-5.

2. Lui KH, Tam EWC. Evaluation of optical properties and tissue oxygenation of tissues overlying the greater trochanter. International Conferences on Caregiving, Disability, Aging and Technology, Toronto, 2011. p. 69557.

Acknowledgements

I would like to express my heartfelt gratitude to all those who in their own way have supported me during the course of this work. Sincere appreciation goes to:

Dr. Eric TAM, my supervisor, for his professional and tireless guidance, unfailing and continuous encouragement, invaluable comments and suggestions throughout this study. I am most impressed by Dr Tam's enthusiasm and passion towards pressure ulcer research. Undoubtedly, I am proud to have been his student.

Prof. Samuel LO, Prof. Chewyn CHAN, **Dr. Tony TO** and **Dr. Thomas LEE**, for providing the lab, supporting instruments as well as their encouragement and advice during my study.

Mr. Samy LEUNG and **Mr. Kung Chee CHEN** for their advice and guidance during my study.

Department of Health Technology and Informatics (HTI), for giving me the chance to study here and for my stipend during my study.

HTI colleagues, for their support and encouragement. I really treasure our friendships created in this period of time.

Last but not least, **my family** as well as **my friends in the Hong Kong Polytechnic University** and **Hong Kong Blind Sports Association** for their care, encouragement and spiritual support throughout all my studies.

Table of Contents

List of Figures

List of Tables

Abbreviation

CytOx	cytochrome oxidase
[CytOx]	Concentration of cytochrome oxidase
Hb	Deoxyhemoglobin
[Hb]	Concentration of deoxyhemoglobin
HbO_2	Oxyhaemoglobin
$[HbO_2]$	Concentration of oxyhemoglobin
LDF	Laser Doppler flowmetry
NIRS	Near-infrared spectroscopy
SCI	Spinal cord injured
S_tO_2	Tissue oxygen saturation
$TcPO_2$	Transcutaneous oxygen tension
tHb	Total hemoglobin
[tHb]	Concentration of total hemoglobin
TOI	Tissue oxygenation index
$\mu_a(690\ \text{nm})$	Absorption coefficient at wavelength 690 nm

$\mu_a(765\ \mathrm{nm})$	Absorption coefficient at wavelength 765 nm
$\mu_a(830\ \mathrm{nm})$	Absorption coefficient at wavelength 830 nm
$\mu_a(856\ \mathrm{nm})$	Absorption coefficient at wavelength 856 nm
μ_s	Scattering coefficient
$\mu_s(690\ \mathrm{nm})$	Scattering coefficient at wavelength 690 nm
$\mu_s(765\ \mathrm{nm})$	Scattering coefficient at wavelength 765 nm
$\mu_s(830\ \mathrm{nm})$	Scattering coefficient at wavelength 830 nm
$\mu_s(856\ \mathrm{nm})$	Scattering coefficient at wavelength 856 nm
μ_s'	Transport scattering coefficient
$\mu_s'(690\ \mathrm{nm})$	Transport scattering coefficient at wavelength 690 nm
$\mu_s'(765\ \mathrm{nm})$	Transport scattering coefficient at wavelength 765 nm
$\mu_s'(830\ \mathrm{nm})$	Transport scattering coefficient at wavelength 830 nm
$\mu_s'(856\ \mathrm{nm})$	Transport scattering coefficient at wavelength 856 nm
λ	Wavelength of light

Chapter 1

Introduction

Pressure ulcers are localized injuries to the skin and/or underlying tissues, usually occurs overlying bony prominence, as a result of pressure, or pressure in combination with shear and/or friction (1-3). Pressure ulcers are either originated at the skin surface or from deep tissues. Superficial ulcers are usually characterized by non-blanchable erythema and can be detected by skin inspection (4, 5). However, deep pressure ulcers involve the breakdown of tissues overlying bony prominence. If not realized, it could turn into a massive lesion that propagates towards the skin (1, 2, 6). This complication could also be life threatening. The incidence rates of pressure ulcer during hospitalization were ranged from 1.5% to 10.27% (7-9). However, for spinal cord injured patients and the elderly, the prevalence rates of pressure ulcer during hospitalization were 85% and 73% respectively. It has shown that patients with pressure ulcers would require extended hospitalization ranged from 7 to 50 days (9, 10). In 2006, it was reported that there were over 540 thousand adults in USA suffered from pressure ulcers and require hospitalization. This figure showed a 1.8-fold increase when compared to 1993. The total cost of pressure ulcers management has also exceeded US$11 billion (8). In terms of prevention, most of the currently used strategies and interventions were not totally effectual. With the growing financial burden associated with the treatment of pressure ulcers, there are strong urges to innovate new techniques for early detection of tissue distress.

The causation of pressure ulcers has been attributed to a number of risk factors including interfacial pressure (11-15), microclimate (i.e. temperature and humidity) at the tissue-supporting interface (16), reduction in mobility and pain sensation (17), tissue ischemia due to prolonged compression (18-21), tissue distortion resulting from shear stress and compression (22-25), aging (26, 27) as well as malnutrition (28, 29). Of all these factors, the effect of interfacial pressure, ischemia, shear and tissue distortion has been highlighted in literatures (1-3, 30). In clinical practice, interfacial pressure was commonly measured and used as a tissue distress indicator for pressure ulcer. However, interfacial pressure distribution cannot unveil the subcutaneous loading condition where deep pressure ulcer originates. In literature, several early studies have attempted to use tissue oxygenation as a parameter to quantify tissue viability (23, 31-34). Unfortunately, the instrumentations used for these studies all have very limited penetration depth. The oxygenation of deeper tissues particularly those overlying bony prominences, remains unrevealed.

In recent years, a number of studies have used near infrared (NIR) spectroscopy to monitor tissue oxygenation of the brain (35, 36) and muscles (37-42). The algorithm of NIR spectroscopy involves *in vivo* measurements on the absorption coefficients (μ_a) of the deep tissues at two or more wavelengths of near infrared light (43). Then, Beer Lambert's law was used to determine the oxyhemoglobin concentration ($[HbO_2]$) and deoxyhemoglobin concentration ([Hb]), total hemoglobin concentration ([tHb]) as well as tissue oxygen saturation (S_tO_2). The

concentrations of oxyhemoglobin and total hemoglobin as well as tissue oxygen saturation provide tissue oxygenation information including oxygen storage, blood supply and hemoglobin saturation level within the tissues. There are three methods used for the quantification of μ_a, including the time-resolved (TD) method (44), the multi-distance frequency domain (FD) method (45) and the spatially resolved (SR) method (46). Among these three methods, the SR method can be constructed with widely available commercial instrumentation and thus has higher potential to develop for home care usage. However, the applicability of SR method requires consistent wavelength dependence of the transport scattering coefficient $\left(\mu_s'(\lambda)\right)$ at wavelengths (λ) of NIR light in the examination region among subjects (46). Such wavelength dependence of $\mu_s'(\lambda)$ in forearm, scalp and calf muscle (47) have been established, but those at anatomical sites prone to the development of pressure ulcer have not been determined.

In the present study, we aimed to develop a NIR photometer using the spatially resolved method to assess the viability of tissues at anatomical sites that are at risk of pressure ulcer. Three investigations were undertaken in this work. To ensure that the SR method is applicable for use, we examined the consistency of wavelength dependence of the transport scattering coefficient $\mu_s'(\lambda)$ among subjects in the greater trochanter regions, which is a location at risk of pressure ulcer. Secondly, we developed a blood-Intralipid tissue phantom to validate tissue oxygenation measurements from our spatially resolved near infrared (SR-NIR) photometer.

Lastly, we examined the change of tissue oxygenation after electrically-stimulated exercise by *in vivo* measurements using the newly developed NIR photometer.

Chapter 2

Literature Reviews

2.1. The etiology of pressure ulcers

Pressure ulcers are localized areas of tissue breakdown in skin and/or underlying tissue resulting from prolonged unrelieved pressure (9). The onset of pressure ulcer is highly related to the amount of pressure acting on tissues and the duration of loading. Pressure ulcer usually occurs in tissues overlying bony prominence. Examples included the ischial tuberosities, sacrum, greater trochanters and the heel. Pressure ulcer can initiate either at the skin layer or from deep tissues. The causation of pressure ulcer has been attributed to many potential risk factors (1-3) including interfacial pressure (11-15); microclimate (i.e. temperature and humidity) at the supporting interface (16); reduction in mobility and pain sensation (17); shear and friction; tissue ischemia due to prolonged compression (18-21); tissue distortion resulting from shear stress and compression (22-25) as well as malnutrition (28, 29). In literature, many works have been published to address the effect of interfacial pressure, ischemia, shear and friction as well as tissue distortion on tissue damage (1-3, 30, 48, 49).

2.1.1. Effect of interfacial pressure

Prolonged unrelieved pressure has long been regarded as the primary cause of pressure ulcer. In early work, Husain (50) showed that pressure application of 100 mmHg for short duration (2 hours) only produced histological changes in tissues

(i.e. cellular extravasation and neurophilic infiltration) while prolonged compression (6 hours) with the same magnitude of pressure triggered tissue necrosis. This result suggested that there exists a threshold in pressure-time relationship where tissue injury will become irreversible. Clinically, common anatomical sites that are prone to pressure ulcer are tissues overlying bony prominence including ischial tuberosities, greater trochanters, sacrum, etc. Such regions are usually subjected to higher interfacial pressures (13, 15, 51). Many later studies have demonstrated that tissue breakdown occurs with high pressure loading for short duration of time and low pressure loading for prolonged period of time (11, 14, 52-56). This pressure-time relationship to which pressure ulcers develop was found to be parabolic (Figure 2.1). Many studies have observed that muscle was less tolerance to pressure than skin and fat (14, 52, 57). Linder-Ganz (58) investigated the muscle damage threshold by applying pressure (86 to 578 mmHg) directly on the rat limb at different time intervals (15-360 mins). Their result showed that the pressure-time curve of muscle injuries threshold was found to be in sigmoid function (Figure 2.2). This implied that there exists a finite pressure magnitude threshold for muscle damage evenly for short duration of loading (15-60 mins). In long exposure to pressure (2-6 hours), muscle could withstand the loading without damage at a tolerable pressure magnitude.

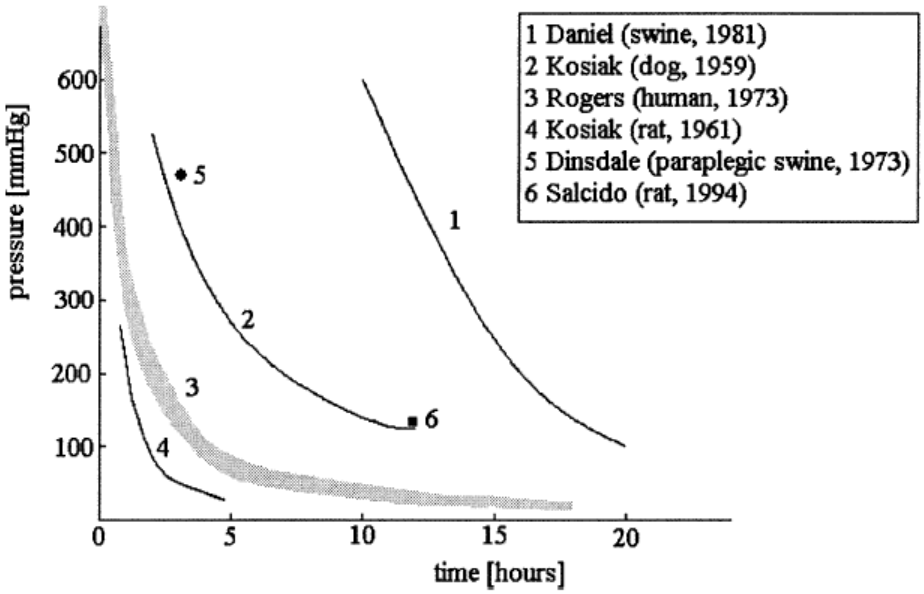

Figure 2.1 Pressure-time curves with regard to pressure ulcers formation in rat, dog, swine and human models (3). The area above the curves indicated the pressure and time that could cause tissue breakdown.

Pressure causes compressive and shear stress (1, 24, 59). Using a model constructed from imaging data obtained in human, the stress and strain conditions within tissues were estimated using computer modeling technique. With prescribed interfacial pressure distributions, superficial tissues closer to the skin were found have larger distortion while muscles and subcutaneous tissues near bony prominence were subjected to higher tensile stress (60-63).

High interfacial pressure could lead to localized tissue ischemia. Normal capillary pressures in upper and lower limbs were ranged from 16 mmHg to 33 mmHg (64) and from 12 mmHg to 32 mmHg respectively (65). In daily activities,

weight-bearing tissues could easily exceed such pressure limits causing capillaries to occlude. In fact, several studies have reported reduction of blood flow and tissue oxygen tension when external pressure was applied to tissues (31, 66-68).

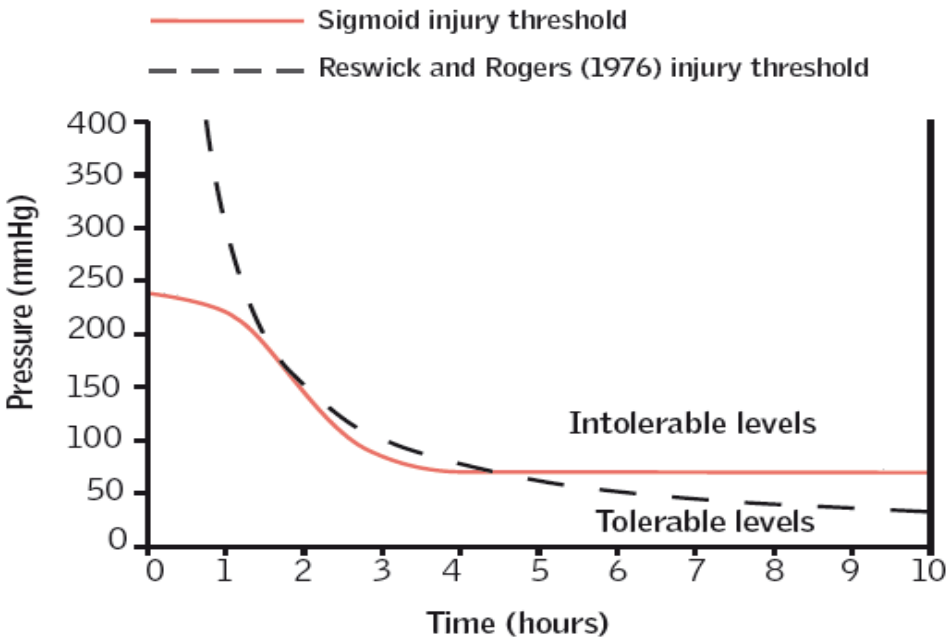

Figure 2.2 Sigmoid injury curve proposed by Linder-Ganz. For short period of loading (15-60 mins), pressures greater than 240 mmHg caused cell death in rat muscle tissue. For the intermediate loading duration (1-2 hrs), the pressure threshold was dropped from 240 mmHg to 67 mmHg. For long pressure exposure (2 hours or above), muscle could survive from damage when pressures loading below 67 mmHg (69).

2.1.2. Effect of shear

Shear stress occurs when a force tangential to the surface was applied to an object adhered to a stationary base. As a result to shearing, the object will deform and the amount of deformation is referred as shear strain. Depending on the interfacial

conditions (i.e. pressure and friction) and the geometry of the skeletal structure under loading, shear stress and strain experienced by tissues at different locations within the loaded tissues will vary (59, 70, 71). Under gravity, shear stress is unavoidable. Tissues near the skin will be subjected to compressive stress, whereas, both tensile and shear stresses were experienced by tissues near the skeletal structures (Figure 2.3). Oomens and coworkers (61) examined the shear strain at the skin, fat and deep muscle layers under seating condition. They reported that shear strain was highest in the skin and fat layer, followed by the area between deep muscles and bony prominence, and was lowest in the fat-muscle interface (Figure 2.4). One of the interesting finding from their results was that when softer (with higher μ value in elastic Ogden model) cushions were used, the shear strain at skin and fat layers were reduced. However, the shear strain between deep muscles and bony prominence was not reduced. Ceelen and coworkers (63) studied the relationship between shear strain and tissue damages in a rat model. By compressing the tibialis anterior region for 2 hours, Ceelen showed that the tissue damage in deep muscles increased after the maximum internal shear strain exceeded 0.75. This suggested that the shear may contribute to the tissue damage.

In literature, shear stress was also attributed to be a contributor of tissue ischemia. Shear stress caused stretching of the skin and underlying tissues. The stretched tissues may elongate the capillaries within tissues and reduced its cross section area (59, 70, 71). A number of studies have been conducted to determine the effect of

shear on vascular occlusion. Shear stress in these studies was usually estimated by the magnitude of external pressure loading using elastic theory. By using a rat model, Bennett and coworkers (72) demonstrated in rat that when shear stress was introduced, the required pressure for skin capillary occlusion can be reduced by 50%. Zhang and Roberts (25) also showed that skin blood flow was linearly reduced with the increase in shear stress. Using a finite element model based on the limb of rat, Linder-Ganz and Gefen (73) showed the total capillary cross section area was reduced to 46% with shear strain of 1.7 % to 8.8 % (overall deformation of the limb) under the same external applied pressure (120 kPa).

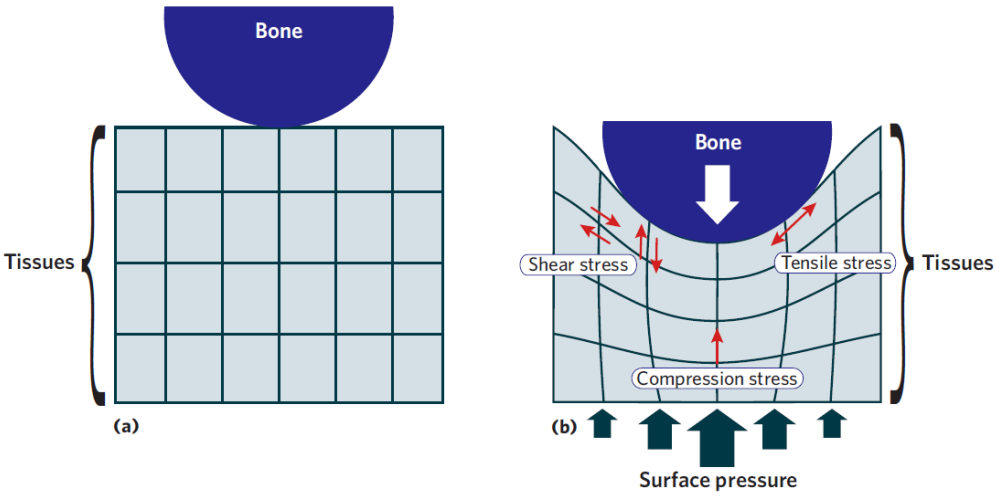

Figure 2.3 An example of shear in deep tissues. The interfacial pressures were unevenly distributed on the tissue at the bony prominence. Shear stresses were tangentially stretched and distorted tissue nearby (24).

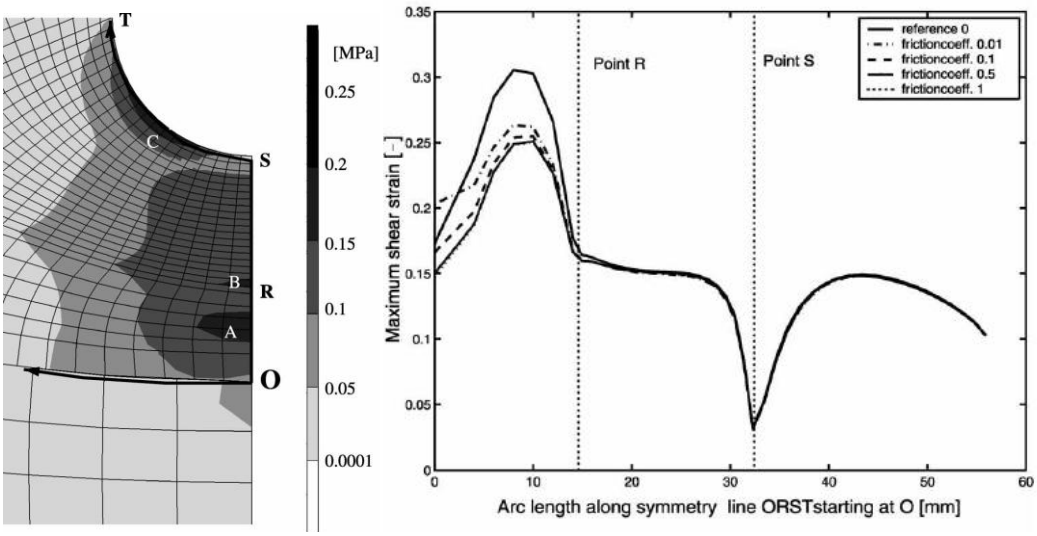

Figure 2.4 Maximum shear along line ORST starting at O where O is the skin-cushion interface, R is the fat-muscle interface and S is the muscle-bone interface. The shear strain on the skin and fat layer was lower when using softer cushions to support the body (61).

2.1.3. Effect of ischemia

Ischemia is defined as the restriction of blood supply to tissues. When tissues are subjected to compressive and shear stresses, the capillary could be partial or totally collapsed. Complete lacking or insufficient supply of oxygen and nutrient delivered to tissues cannot sustain the need of normal cellular activity. This status is called hypoxia. The cells of the hypoxic tissues cannot produce sufficient energy by aerobic metabolism. Instead, the ischemic tissues perform anaerobic metabolism that required less oxygen supply. During anaerobic metabolism, cells deplete their glucose and adenosine triphosphate (ATP) deposits as well as produce lactic acid. If

the depletion of ATP and glucose or accumulation of lactic acid get beyond a certain threshold, cellular death can result (74).

During prolonged ischemia, oxygen debt in tissues causes the conversion of dehydrogenase (XDH) to xanthine oxidase (XO) and produces hypoxanthine and xanthine through the breakdown of ATP. Once the oxygen molecules are reintroduced to tissues during reperfusion, hypoxanthine and xanthine can activate the reaction of oxygen molecules and XO to produce toxic reactive oxygen metabolites like superoxide and hydrogen peroxide. Although this reaction does not occur during ischemia (oxygen molecules are not yet reintroduced to the ischemic tissues), these potential toxic substrates can continuously produce and accumulate in tissues during ischemia (75, 76).

When external pressure is removed after prolonged occlusion, blood flow will restore. Oxygen is reintroduced to the ischemic tissues. During reactive hyperemia, blood vessels will dilate to increase the blood supply. However, as mentioned in previous section, potential toxic substrates may be accumulated within the ischemia tissues. This substrates will react with reperfused oxygen molecules to form toxic reactive oxygen metabolites leading to tissues breakdown (21). Moreover, oxygen-derived free radicals will be produced during reactive hyperemia. If reactive hyperemia was sustained for a long duration, these free radicals could accumulate to a high concentration and exceeded the capacity of

constitutive free radical scavenging mechanisms (75, 77). As a result, it will produce a cyto-toxic effect on tissues and cause further damages (76, 78, 79).

2.1.4. Effect of tissue distortion

Compressive and shear stresses contribute to the tissue distortion. In recent years, a number of published studies have proposed that excessive tissue deformation could play a key role in the development of pressure ulcers. Direct mechanical insult to cell and impaired diffusion of essential molecules in tissues with excessive deformation were postulated as mechanisms to pressure ulcer formation (80-84). Figure 2.5 shows the proposed pathway of tissue breakdown resulting from tissue deformation. When compressive or shear stresses were applied to tissues, cells in the tissues would suffer different level of distortion. This may lead to the disruption of cell membrane. The degree of membrane disruption determines the trigger point to cell death. When the disruption is less than 1 micron, no cell death would occur. The disrupted membrane would be resealed spontaneously since the reformation of normal lipid bilayers structure can return to the lowest energy state. Cell death occurs when cell membrane disruption is beyond 1 micron. As the membrane cannot be resealed spontaneously, calcium ions flowed into the cell and increased the intracellular concentration. The inflow of calcium ions were detected by particular organelles in the cell. At certain threshold of calcium ion concentration, exocytosis will be initiated and cell death will result (85).

The viability of tissue relies on adequate blood supply which brings along oxygen and nutrients. Recently, the effect of impaired diffusion of metabolites within deformed tissue was studied using tissue-engineered bio-artificial muscles. Gefen and coworkers (83) examined the diffusion capacity of fluorescently labeled dextran molecules (10 kDa, 20 kDa and 150 kDa) in deformed engineering muscles. The diffusion rate of such molecules was on average reduced by 47% when the tissues were subjected to compressive strains of 53% to 60%. The result suggested that there may be impaired diffusion of molecules with large molecular weight, such as hormones and biomarkers, which could have substantial influence to tissue metabolism. This may affect the cellular activities in the deformed tissues. In another study, van Nierop et al. (84) showed that the diffusion capacity of small molecules was not affected in large deformation. They used MRI to measure the rate of water diffusion in compressed rat limb. They found that the water diffusion rate in tibialis anterior and gastrocnemius muscle were reduced by 7.2% and 5.9% respectively under large shear strain of 67%. This suggested that the diffusion of some important molecules like oxygen and carbon dioxide, which are smaller or of similar size to water (18 Da), may not be affected in the deformed tissues.

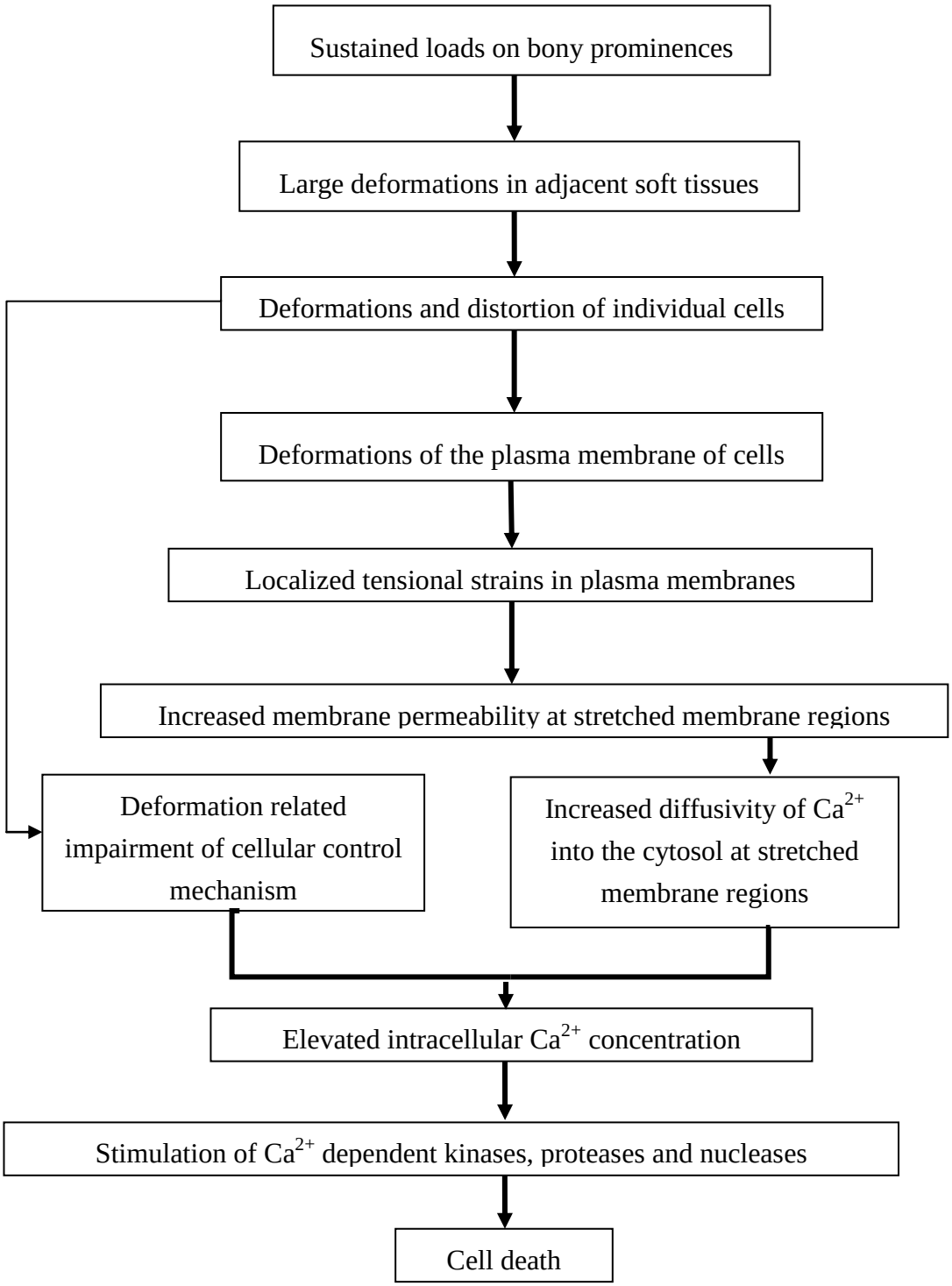

Figure 2.5 Proposed mechanism of deformation-induced tissue damage (86)

2.2. Preventive measures of pressure ulcer

Preventive measures of pressure ulcer are intended to minimize the effect of the risk factors mentioned in previous section. In clinical practice, several risk assessment tools like the Norton and Braden scales are commonly used to assess the risk of pressure ulcer in individual patients (87). For patients at high risk of pressure ulcers, efforts have been concentrated to reduce the magnitude and duration of pressure and shear exposures. To achieve this, attempts were made to evenly distribute the interfacial pressure over the entire support surface. This is to eliminate any localized high pressure points that may be induced during different sitting and lying postures (12, 88, 89). For example, it has been shown that localized high pressure can be found at the greater trochanter during 90° side-lying and at the sacrum during a semi-recumbent posture. In addition, bed elevation should be reduced to prevent shearing resulted from a semi-recumbent posture (90). Regular position changes can relieve external pressure loading to a particular region (13). Defloor (91) found that by repositioning the body every 2 hours during 4 weeks hospitalization, incidence rates of pressure ulcer can be reduced from 20% to 14.3% when compared to those without such intervention. In fact, the 2-hours rule of turning are commonly adopted for handling immobilized patients in clinical practice. Alternating Pressure System also provides an alternating way for frequent pressure redistribution. The system usually contains a number of air sacs. These sacs are aligned in predetermined patterns. Activation of these sacs is programmed

to follow a specific time-sequence (Figure 2.6). This allows tissues at the supporting surface to take turns to have pressure relief (92, 93).

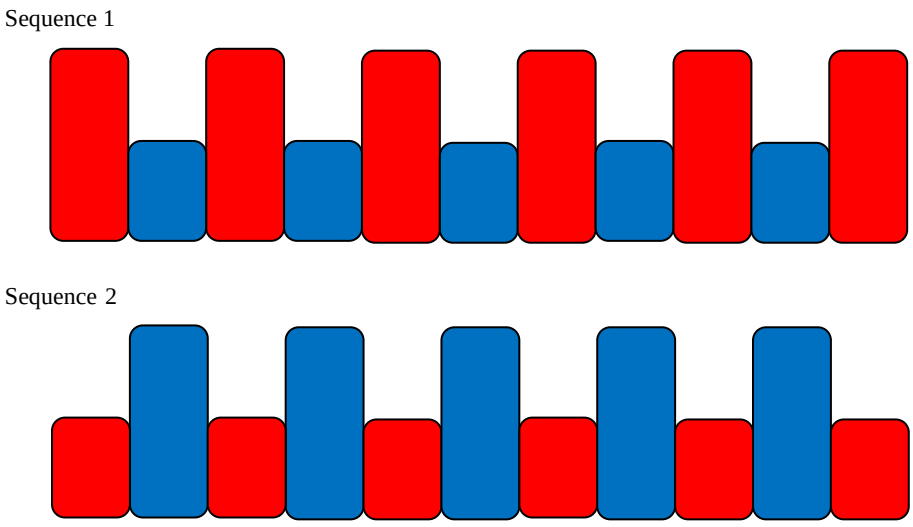

Figure 2.6 An example of a simple Alternating Pressure System. In Sequence 1, the red sacs inflated to support the body weight and pressure relief on surface located in the region of blue sacs. In Sequence 2, the blue sacs take the role to support the body weight and pressure relief of tissues on the location of red sacs. The two sequence shift alternatively after a period of time.

Another key factor on pressure redistribution relates to the material properties of body supporting system. The body supporting system should be able to relieve pressure and shear stress as well as controlling the microclimate. Normally, the degree of immersion and envelopment will determine the interfacial pressure condition. Immersion refers to whether the body can sink into the supporting surface. Soft materials can allow higher level of immersion, but it could cause

“bottom-out” if the cushion is not thick enough. Envelopment refers to the conformability of the supporting surface against the irregular body contours (94). Several types of supporting systems, which claimed to have good immersion and envelopment characteristics, have been suggested for clinical use. These included visco-elastic foam, air or gel filled systems and air fluidized systems (16, 95, 96).

Frequent body repositioning together with the use of pressure relieving supports have shown to better reduce the incidence rate of pressure ulcers for long term hospitalized patients (3, 95, 97). In a 4-week study, Defloor et al. (91) showed that when combined body repositioning and using pressure relieving mattress, the incidence rate of pressure ulcer was reduced to 3%. Another 5-week study by Vanderwee et al. showed that the pressure ulcer incidence rates were reduced from 21.2% to 16.4% after combined interventions using pressure reducing mattress and frequent repositioning (i.e. 2-hours lateral position and 4-hours supine position) (98).

2.3. Assessment of tissue viability

Early detection of tissue distress allows immediate protection regimes to take place and prevents further damages to occur. Unfortunately, current clinical techniques were unable to detect pressure ulcers originated from deep tissues and patients that have reduced pain sensations may not realize that his/her tissues have become vulnerable. Therefore, it was necessary to have a quantitative tool to assess the viability of tissues at anatomical areas that are prone to pressure ulcer.

Tissue oxygenation has long been suggested as an indicator to reflect tissue viability (31, 34). Oxygen is essential for cellular activities. Belkin et al. (99) examined skeletal muscle injury in ischemic rat limb. By assessing the quantity of triphenyltetrazolium chloride (TTC) using spectrophotometric analysis, Belkin found that the amount of TTC reduction in the ischemic limb relative to non-ischemic limb indicates the amount of muscle injuries. The result showed that muscle injuries started after 3 hours of ischemia and continuous to progress for another 3 hours towards the end of experiment. Besides, several early studies have made use of tissue oxygenation measurements to evaluate the risk of pressure ulcers formation (31-33, 100, 101). Bader (31) used transcutaneous oxygen tension ($TcPO_2$) as an indicator to monitor tissue recovery after pressure relief. He showed that in healthy subjects, $TcPO_2$ started to restore immediately after removal of external loading and returned to baseline after two minutes while debilitated patients can only have partial recovery within the same period of time. However, when repetitive loadings were applied, Bader noted an adaptive effect on $TcPO_2$ changes. In healthy subjects, reduction of $TcPO_2$ was reduced with successive loading cycles. Whereas for debilitated patients, $TcPO_2$ was unable to return to baseline before the next loading cycle. This caused a continuous reduction of tissue oxygenation level. In addition to the use of transcutaneous oxygen tension as a measure of tissue viability, other researchers also utilized laser Doppler flowmetry to assess skin blood flow and relate the measurements to tissue insults (32, 100, 101). However, due to the limited penetration power of both laser Doppler

flowmetry and $TcPO_2$ techniques, the viability of deep tissues overlying bony prominence may not be revealed. Near infrared spectroscopy can assess the oxygenation states of deeper tissues and has the potential to use for early detection of deep tissue injuries.

2.4. Principles and limitations of current tissue oxygenation evaluation techniques

Laser Doppler flowmetry, transcutaneous oxygen tension measurement and visible light diffuse reflectance spectrometry has been used for the evaluation of tissue oxygenation in pressure ulcer researches (18, 19, 25, 31, 33, 100, 102, 103). This section will describe the principle and limitation of these techniques in tissue oxygenation evaluation.

2.4.1. Laser Doppler flowmetry

Laser Doppler flowmetry (LDF) is an optical, non-invasive method used to monitor microvascular blood flow in the skin level. The method begins by applying a monochromatic light to illuminate the targeted tissue. The incident light will be back-scattered by the moving red blood cells in the bloodstream within illuminated region causing a frequency shift. This change was measured in arbitrary unit reflecting the perfusion status of the tissue. The perfusion flux is linearly related to the velocity of the moving red blood cells (v_{RBC}) as well as their concentration ([RBC]) (104):

$$\text{Perfusion flux} = v_{RBC} \times [\text{RBC}] \quad [1]$$

In clinical situation, LDF technique has been used to monitor the perfusion status of tissues that are prone to pressure ulcers (71, 72, 106). Recently Li et al. (102) utilized LDF to examine the vasomotion in spinal cord injured (SCI) rats. By applying frequency spectral analysis on the acquired LDF signals, information related to vasomotion can be obtained. Vasomotion is the spontaneous oscillation of blood vessels by dilation and constriction. It does not depend on heart beat, innervations or respiration. There are five frequency intervals of oscillation related to metabolic (0.01-0.05 Hz), neurogenic (0.05-0.15 Hz), myogenic (0.15-0.4 Hz), respiratory (0.4-2 Hz) and cardiac (2-5 Hz) activities. By using laser Doppler flowmetry to monitor the vasomotion, Li et al. showed that the amplitude of the LDF signal within the frequency range representing neurogenic activities in SCI rats was significantly lowered than that of normal rats. In the study, the SCI rats were observed with reduced reactive hyperemic response after release of loading on the trochanter region. This suggested that reduction of neurogenic activities may be related to the decrease of reactive hyperemic response of SCI rats leading to a delay of the recovery of tissue oxygen level from hypoxic state.

There are several limitations associated with the use of LDF for blood flow measurement (105-107). First, the perfusion flux is only an arbitrary value for blood flow. The value in "no flow" condition is undefined. Second, the

measurement depth is unclear. It was generally believed that the signal was from the capillaries of the dermal papillae located 1 to 2 mm from the skin surface. Third, LDF measurement is sensitive to motion artifacts and the contact pressure of the sensor probe to skin. As a result, LDF is not suitable for measurements during dynamic body activities (105-107).

2.4.2. Transcutaneous oxygen tension measurement

The transcutaneous oxygen tension ($TcPO_2$) measurement is a non-invasive measurement and was developed as an alternative to invasive oxygenation measurement using catheter-tip blood gas electrode. The measurement principle of $TcPO_2$ depends on the permeability of oxygen in skin and its good correlation with arterial oxygen tension (PaO_2). Measurements require pre-heating the skin to 45 ℃ to enhance oxygen perfusion by vasodilatation. Oxygen molecules diffusing from capillaries will enter the electrode placed on the skin surface. At the $TcPO_2$ sensor, oxygen molecules undergo a chemical reaction, generating a current flow between 400 mV to 800 mV. This voltage represents the $TcPO_2$ level of the tissue at the measurement site. Normal $TcPO_2$ values have been shown to range between 45 and 95 mmHg (108). The higher of $TcPO_2$ value, the better the perfusion of oxygen in tissues.

The $TcPO_2$ parameter can also be used to represent the efficiency of oxygen delivery to the skin (109). In comparison to healthy subjects, several studies have demonstrated a lower resting $TcPO_2$ level at the sacrum, greater trochanter and

ischial tuberosities of spinal cord injured patients (18, 110). It has also been shown that $TcPO_2$ level was reduced when tissues were subjected to pressure and shear loading (23, 67). The duration for $TcPO_2$ to regain baseline after removal of loading was found to be longer in paraplegic patients. Clinically, $TcPO_2$ has also been used as a measurement parameter for the evaluation of different pressure relief products (33, 100).

Similar to laser Doppler flowmetry, $TcPO_2$ only reveal the oxygenation condition of superficial tissues (109). Besides, this technique does not reflect the actual oxygen content in the measurement area as oxygen may be diffused from the vascular network next to the measurement site.

2.4.3. Visible light diffuse reflectance spectroscopy

The visible light diffuse reflectance spectroscopy measures the absorption spectrum of visible light at the investigation site. This spectrum can be used to calculate the hemoglobin index (HbI) and tissue oxygenation index (OXI) which are associated with tissue oxygenation. These two indices were first developed by Feather (111) and then modified by Harrison (1992). In the visible light region, the absorption spectrum of oxyhemoglobin and deoxyhemoglobin are different (Figure 2.7). The absorption spectrum of oxyhemoglobin contains double peaks while that of deoxyhemoglobin contains a single peak. There are five isosbestic points at which absorbance of the two spectra are the same. The slopes among the isosbestic points represent the similarity between the absorption spectrum measured by visible light

diffuse reflectance spectroscopy and the spectrum of pure oxyhemoglobin as well as the spectrum of pure deoxyhemoglobin. The HbI and OXI were calculated by following equations.

$$\mathrm{HbI} = \left[\left(\frac{E_{\lambda 2} - E_{\lambda 1}}{\lambda_2 - \lambda_1}\right) + \left(\frac{E_{\lambda 3} - E_{\lambda 1}}{\lambda_3 - \lambda_1}\right) + \left(\frac{E_{\lambda 3} - E_{\lambda 4}}{\lambda_4 - \lambda_3}\right) + \left(\frac{E_{\lambda 4} - E_{\lambda 5}}{\lambda_5 - \lambda_4}\right)\right] \times 100 \quad [2]$$

$$\mathrm{OXI} = \left[\left(\frac{E_{\lambda 5} - E_{\lambda 4}}{\lambda_5 - \lambda_4}\right) - \left(\frac{E_{\lambda 4} - E_{\lambda 3}}{\lambda_4 - \lambda_3}\right)\right] \times \frac{100}{\mathrm{HbI}} \quad [3]$$

where $E_{\lambda x}$ is the absorbance at the wavelength of x^{th} isosbestic point.

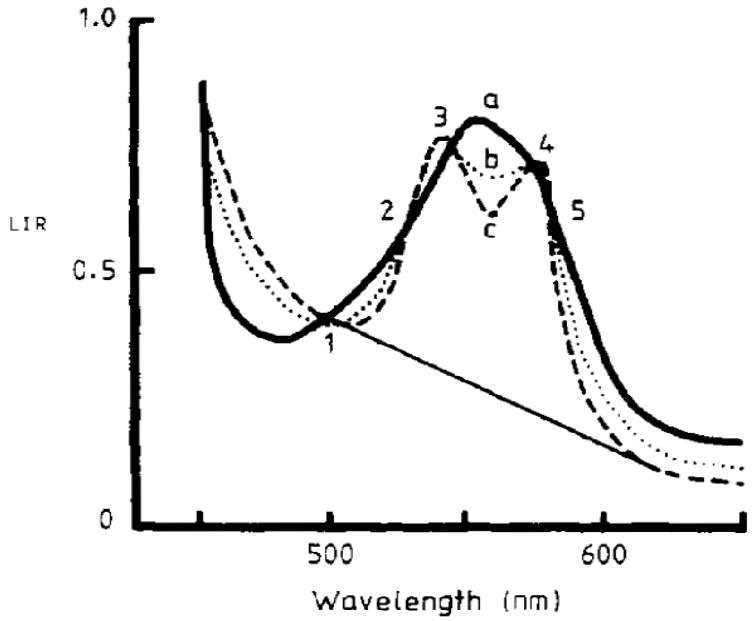

Figure 2.7 The five isosbestic points are intersection points between curves of deoxygenated hemoglobin (a), 60% oxygenated hemoglobin (b) and fully oxygenated hemoglobin (c) (111).

Compared to LDF and $TcPO_2$ measurements, the visible light diffuse reflectance spectrometry can directly measure the hemoglobin oxygenation. A number of studies have used visible light diffuse reflectance spectrometry to evaluate the effect of compressive loading on tissue oxygenation in both healthy subjects and patients at high risk of pressure ulcers (19, 112, 113). However, this technique also has some inherited limitations. Visible light is highly absorbed in biological tissues. Since the absorption of melanin and hemoglobin were comparable (114), individuals with darker skin pigments will affect the measurement accuracy of visible light diffuse reflectance spectroscopy. Besides, the penetration depth of the visible light could only reach several millimeters up to the dermis level (115).

2.5. Fundamental of tissue optic

Light is an electromagnetic radiation characterized by intensity, wavelength, propagation direction and polarization. When light propagates in a single medium or passes from one medium to another medium, its magnitude, frequency and phase may change. These properties can be applied to medical diagnosis and therapeutic applications. Indeed, absorption and scattering of light are often utilized to determine *in vivo* conditions in tissues, like blood oxygenation. This session will describe these optical properties and introduce two important coefficients related to light propagation in tissues, namely the absorption coefficient and transport scattering coefficient.

2.5.1. Absorption

Absorption is an interaction between the light and absorbing molecules in a medium. Light energy is transferred into chemical or thermal energy during propagation along the medium. These energies are being absorbed and the light intensity is reduced along the propagation path. Consider a collimated beam of light at wavelength λ with intensity I_0 propagates along a homogeneous non-scattering medium of thickness (L) with a single absorber (Figure 2.8), the transmitted light intensity will be given by:

$$I(\lambda) = I_0(\lambda)e^{-\mu_a(\lambda)L} \quad [4]$$

where $\mu_a(\lambda)$ is the absorption coefficient of medium at wavelength, λ.

The absorbance (A) and transmittance (T) of this media are expressed as:

$$T(\lambda) = \ln\frac{I(\lambda)}{I_0(\lambda)} = -\mu_a(\lambda)L \quad [5]$$

$$A(\lambda) = \ln\frac{1}{T(\lambda)} = \mu_a(\lambda)L \quad [6]$$

Beer (116) measured the attenuation of light in different concentrations of red dye. By including the concentration of the absorber, equation [6] becomes:

$$A(\lambda) = \alpha(\lambda)CL \qquad [7]$$

where $\alpha(\lambda)$ and C are the specific absorption coefficient and the concentration of particular absorbing molecules

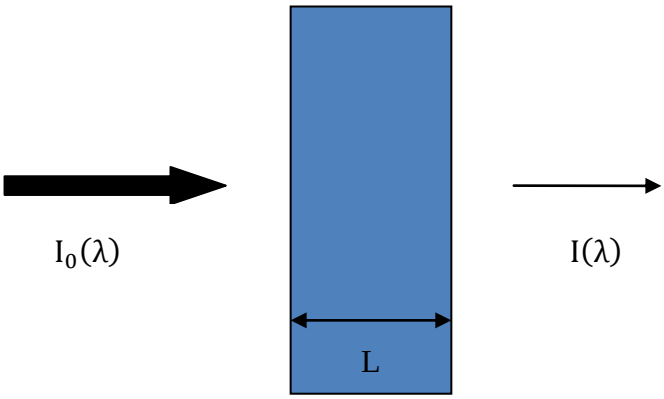

Figure 2.8 Attenuation of light after passing through a non-scattering, absorbing medium.

In biological tissues, molecules that absorbed light are called chromophores. Each chromophore has its own specific absorption spectrum. Examples of common chromophores included water, cytochrome c oxidase, hemoglobin, melanin and lipid. Of all known chromophores, hemoglobin dominates the light absorption of blood in the near infrared region. Hemoglobin is a protein made up of 4 possible protein chains, α, β, γ and δ. More than 97% of human hemoglobin is in hemoglobin-A form which contains 2α and 2β chain. Each hemoglobin molecule contains one iron ion. Under particular condition, oxygen molecules physically bind to the iron ion in the hemoglobin molecules and form oxyhemoglobins. The absorption properties of hemoglobin vary after oxygenation. In the near infrared

region, oxyhemoglobin is a stronger absorber at 650 nm than deoxyhemoglobin. However, as wavelength increases, the specific absorption coefficient of oxyhemoglobin will gradually decrease. In contrast, the absorption of deoxygenated hemoglobin starts with low absorption at shorter wavelengths and then slightly increases with longer wavelengths. The two absorption spectra meet at an isosbestic point around 800 nm (Figure 2.9).

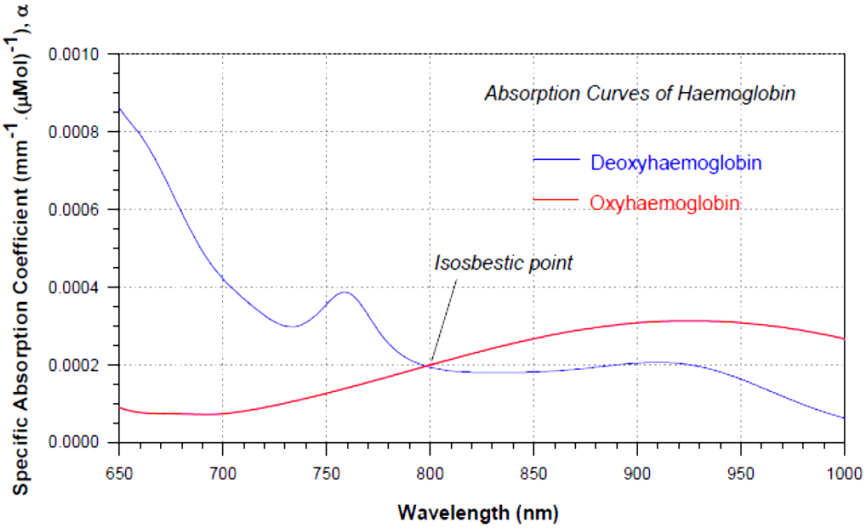

Figure 2.9 Specific absorption spectra of oxyhemoglobin and deoxyhemoglobin (117).

2.5.2. Scattering

Scattering is an interaction that changes the direction of light when light propagates along a medium. There are two types of scattering events: elastic and inelastic. Elastic scattering changes the direction of light while inelastic scattering changes

the wavelength of the incident light. From here onwards, all the "scattering" terms in the later part of this thesis are referred to "elastic scattering". For inelastic scattering, since it only occurs outside the near infrared region, thus it is not considered here. Theoretically, all substances cause light to scatter, but the effect on light distortion depends on the wavelength of the incident light, the concentration of the particle and its size, as well as the mismatch of refractive index between the particle and the media (118). In biological tissues, lysosomes, vesicles and mitochondria dominate most of the scattering events in near infrared light.

When a collimated beam of light at wavelength λ with intensity I_0 propagates along a thin homogeneous and non-absorbing medium with length L, the transmitted intensity of the light can be determined by the following equation:

$$I(\lambda) = I_0(\lambda)e^{-\mu_s(\lambda)L} \qquad [8]$$

where $\mu_s(\lambda)$ is the scattering coefficient of medium at wavelength λ.

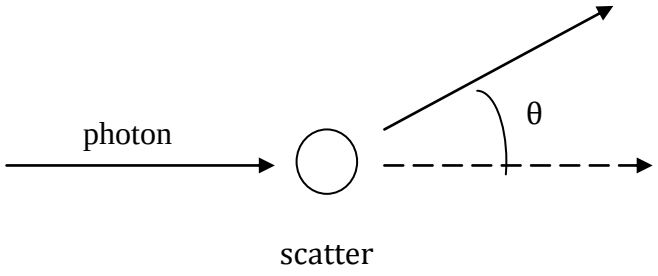

Figure 2.10 An illustration of a single scattering event of photon. A single photon is scattered by a scatter with deflection angle θ.

For every single scattering event (Figure 2.10), photons are randomly deflected at different angles (θ). The possibility of light retained in the forward direction $(\cos\theta)$ after a single scattering event can be quantified by the anisotropic factor or average cosine of scatter (g). The anisotropic factor describes whether the light is dispersed more likely to propagate forward (g = 1), isotropic (g = 0) or backwards (g = -1) after the scattering event. In literature, the anisotropic factor in biological tissues was ranged between 0.69 and 0.99 (119). Higher anisotropic factor value implies deeper penetration of light into the biological tissues. The deeper penetration of light, more anisotropic scattering events occur in random directions. When scattering is dominated over absorption (i.e. near infrared light in biological tissues), multiple steps of anisotropic scattering will occur in random directions before the incident light reaches an absorber. The resultant scattering is equivalent to a few steps of isotropic scattering (120) (Figure 2.11) which can be quantified by the transport scattering coefficient (μ_s'). Equation [10] shows the relationship among the transport scattering coefficient, the anisotropic factor and the scattering coefficient.

$$I_0(\lambda) = I(\lambda)e^{-\mu_s'(\lambda)L} \quad [9]$$

$$\mu_s'(\lambda) = (1-g)\mu_s(\lambda) \quad [10]$$

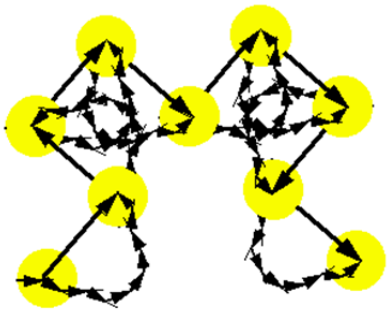

Figure 2.11 A diagram shows the anisotropic scattering events (small black arrows) before reaching the absorber (yellow ball). The deflected light direction of anisotropic scattering events from one to another absorber was random and the consequence was equivalent to a single isotropic event (large black arrows), which the probabilities of all scattered light directions were equal (121).

2.6. Principle of near infrared spectroscopy

Near infrared (NIR) spectroscopy was first demonstrated by Jobsis (122) to perform *in-vivo* measurement of brain oxygenation changes in the intact cat's head. By illuminating NIR light to tissues and measuring the back scattered light at a distance from the light source, Jobsis observed that changes in the concentration of oxyhemoglobin ($[HbO_2]$), deoxyhemoglobin ([Hb]) and the oxidized form of cytochrome oxidase ([CytOx]) caused different attenuation of NIR light. In reviewing the development of NIR spectroscopy, Deply and Cope (123) pointed out that due to the low concentration of CytOx in tissues, the contribution of overall absorption of NIR light by CytOx was much less than that of haemoglobin. Thus, NIR light absorption was mainly dependent on $[HbO_2]$ and [Hb]. Deply and Cope also pointed out that NIR light attenuation in illuminated tissues was not solely due to the absorption of chromophores, but also resulted from light scattering. The

relationship between the light attenuation, absorption and scattering coefficients was shown in following equation:

$$\ln \frac{I(\lambda)}{I_0(\lambda)} = \left(\mu_a(\lambda) + \mu_s'(\lambda)\right)L \qquad [11]$$

where $I(\lambda)$ is the intensity of back scattered light, $I_0(\lambda)$ is the intensity of light sources, $\mu_a(\lambda)$ is absorption coefficient, $\mu_s'(\lambda)$ is the transport scattering coefficient and L is the distance of light travelled in the tissues.

Without the effect of scattering, the estimation of chromophores' concentrations can be calculated based on the Beer Lambert's Law. The Beer Lambert's law states that the total light absorption is equal to the sum of individual absorption by different absorbers in the non-scattering medium (equation [12]).

$$\mu_a(\lambda) = \sum_{i=1}^{n} \varepsilon_i(\lambda)[C_i] \qquad [12]$$

where n is number of chromophore in the medium of light propagation, $[C_i]$ is the concentration of the i^{th} chromophore and $\varepsilon_i(\lambda)$ is the specific absorption coefficient of i^{th} chromophore at wavelength λ.

To evaluate the concentration of each chromophore, the number of different wavelengths of light used should be equal or more than the number of tissue chromophores. Since the main absorbers of NIR light in biological tissues are oxyhemoglobin and deoxyhemoglobin, at least two wavelengths of NIR light should be used to quantify the [HbO_2] and [Hb] (equation [13] & [14]).

$$\mu_a(\lambda_1) = \varepsilon_{Hb}(\lambda_1)[Hb] + \varepsilon_{HbO_2}(\lambda_1)[HbO_2] \quad [13]$$

$$\mu_a(\lambda_2) = \varepsilon_{Hb}(\lambda_2)[Hb] + \varepsilon_{HbO_2}(\lambda_2)[HbO_2] \quad [14]$$

By solving the equation [13] and [14], the [HbO_2] and [Hb] can be calculated:

$$[Hb] = \frac{\varepsilon_{HbO_2}(\lambda_2)\mu_a(\lambda_1) - \varepsilon_{HbO_2}(\lambda_1)\mu_a(\lambda_2)}{\varepsilon_{Hb}(\lambda_1)\varepsilon_{HbO_2}(\lambda_2) - \varepsilon_{Hb}(\lambda_2)\varepsilon_{HbO_2}(\lambda_1)} \quad [15]$$

$$[HbO_2] = \frac{\varepsilon_{Hb}(\lambda_2)\mu_a(\lambda_1) - \varepsilon_{Hb}(\lambda_1)\mu_a(\lambda_2)}{\varepsilon_{Hb}(\lambda_2)\varepsilon_{HbO_2}(\lambda_1) - \varepsilon_{Hb}(\lambda_1)\varepsilon_{HbO_2}(\lambda_2)} \quad [16]$$

The tissues oxygen saturation (S_tO_2) can then be determined using equation [17]:

$$S_tO_2 = \frac{[HbO_2]}{[HbO_2] + [Hb]} \times 100\% \quad [17]$$

Further S_tO_2 can be determined by substituting equation [15] and [16] into equation [17].

$$S_tO_2 = \frac{\varepsilon_{Hb}(\lambda_2)\frac{\mu_a(\lambda_1)}{\mu_a(\lambda_2)} - \varepsilon_{Hb}(\lambda_1)}{\left(\varepsilon_{Hb}(\lambda_2) - \varepsilon_{HbO_2}(\lambda_2)\right)\frac{\mu_a(\lambda_1)}{\mu_a(\lambda_2)} - \left(\varepsilon_{Hb}(\lambda_1) - \varepsilon_{HbO_2}(\lambda_1)\right)} \times 100\% \quad [18]$$

Concerning the combined effect of absorption and scattering of light in tissues as mentioned by Deply and Cope, it was reported that the *in vitro* measurement of $\mu_s'(\lambda)$ (ranged from 5 to 100 cm^{-1}) was hundred times of $\mu_a(\lambda)$ (ranged from 0.05 to 0.2 cm^{-1}) in the NIR region (119), indicating that the scattering of NIR light is dominant in biological tissues. To account for the light loss and the extract distance travelled in tissues due to scattering, the Beer Lambert's law was modified by adding a constant term (G) and diffusion path-length factor (D):

$$A(\lambda) = \ln\frac{I(\lambda)}{I_0(\lambda)} = \mu_a(\lambda)Dd + G \quad [19]$$

where $A(\lambda)$ is absorbance and d is sources-detector distance.

Equation [19] assumes that the scattering term is constant over the entire time of measurement and the diffusion path-length factor was found to 4.3 (124). Therefore, the relative changes of the absorbance at a particular wavelength can be expressed by equation [20]:

$$\Delta A(\lambda) = \Delta\mu_a(\lambda)4.3d \quad [20]$$

In a two wavelengths near infrared spectroscopy, the changes of the absorption coefficient at specific wavelengths are related to the changes in the [Hb] and [HbO_2]:

$$\Delta\mu_a(\lambda_1) = \frac{\Delta A(\lambda_1)}{4.3d} = \varepsilon_{Hb}(\lambda_1)\Delta[Hb] + \varepsilon_{HbO_2}(\lambda_1)\Delta[HbO_2] \quad [21]$$

$$\Delta\mu_a(\lambda_2) = \frac{\Delta A(\lambda_2)}{4.3d} = \varepsilon_{Hb}(\lambda_2)\Delta[Hb] + \varepsilon_{HbO_2}(\lambda_2)\Delta[HbO_2] \quad [22]$$

Solving equation [21] and [22], the changes in the [HbO_2] and [Hb] can be expressed by the following equations:

$$\Delta[Hb] = \frac{1}{4.3d}\left(\frac{\varepsilon_{HbO_2}(\lambda_2)\Delta A(\lambda_1) - \varepsilon_{HbO_2}(\lambda_1)\Delta A(\lambda_2)}{\varepsilon_{Hb}(\lambda_1)\varepsilon_{HbO_2}(\lambda_2) - \varepsilon_{Hb}(\lambda_2)\varepsilon_{HbO_2}(\lambda_1)}\right) \quad [23]$$

$$\Delta[HbO_2] = \frac{1}{4.3d}\left(\frac{\varepsilon_{Hb}(\lambda_2)\Delta A(\lambda_1) - \varepsilon_{Hb}(\lambda_1)\Delta A(\lambda_2)}{\varepsilon_{Hb}(\lambda_2)\varepsilon_{HbO_2}(\lambda_1) - \varepsilon_{Hb}(\lambda_1)\varepsilon_{HbO_2}(\lambda_2)}\right) \quad [24]$$

However, the modification of the Beer Lambert's Law can only determine the relative change of [Hb] and [HbO_2]. Absolute measurement of tissue oxygenation cannot be determined. To solve this, three methods have been later developed, namely time-resolved method, multi-distance frequency-domain method and spatially resolved method (43, 123).

2.6.1. Time-resolved method

The time-resolved method was first proposed by Patterson (44). He proposed that the temporal spreading of light after passing through the tissues can reflect the tissues optical properties (i.e. absorption coefficient and transport scattering coefficient). The method requires using pulsed laser sources with very short pulsed width (down to picosecond) to illuminate the tissues and received the light response by a high-frequency photodetector. The theory was based upon the following diffusion equation with isotropic point source (equation [25]):

$$R(\rho, t) = (4\pi Dc)^{-\frac{3}{2}} z_0 t^{-\frac{5}{2}} e^{(-\mu_a ct)} e^{\left(-\frac{\rho^2 + z_0^2}{4Dct}\right)} \quad [25]$$

where $R(\rho, t)$ is the reflected intensity, t is time, c is the speed of light in tissue, ρ is the source-detector distance D is the diffusion coefficient,

$$D = \frac{1}{3[\mu_a + \mu_s(1-g)]} = \frac{1}{3(\mu_a + \mu_s')} \quad [26]$$

z_0 is the initial scattering depth

$$z_0 = \frac{1}{\mu_s'} \quad [27]$$

After natural logarithm and differentiation of the equation [25] and assuming that $\rho^2 \gg z_0^2$, it becomes:

$$\frac{d}{dt}\ln R(\rho,t) = -\frac{5}{2t} - \mu_a c + \frac{\rho^2}{4Dct^2} \quad [28]$$

When time trend goes to infinity in equation [28], the expression becomes,

$$\lim_{t\to\infty}\frac{d}{dt}\ln R(\rho,t) = -\mu_a c \quad [29]$$

The μ_a can be found by the asymptotic slope of the $\ln R(\rho,t)$ vs. time curve

$$\mu_a = \frac{-1}{c}\left(\lim_{t\to\infty}\frac{d}{dt}\ln R(\rho,t)\right) \quad [30]$$

The μ_s' can be calculated by substituting the μ_a resulted in equation [30] and time (t_{max}) during maximum value of $\ln R(\rho,t)$ into equation [31]

$$\mu_s' = \frac{1}{3\rho^2}(4\mu_a c^2 t_{max}^2 + 10ct_{max}) - \mu_a \quad [31]$$

where

$$\frac{d}{dt}\ln R(\rho, t_{max}) = 0 \qquad [32]$$

2.6.2. Multi-distances frequency-domain method

Fishkin and Gratton (125) derived the expressions of phase shift ($\mathbf{\Phi}$), average intensity ($\mathbf{I_{dc}}$) and amplitude of oscillated intensity ($\mathbf{I_{ac}}$) when multi-sinusoidal light sources illuminated the tissues at different distances from the detector (Figure 2.12). The expressions for $\mathbf{\Phi}$, $\mathbf{I_{dc}}$ and $\mathbf{I_{ac}}$ can be obtained by first solving the expression of the photon density $\big(U(r,t)\big)$ and photon current density $\big(J(r,t)\big)$ from diffusion approximation to Boltzmann equation:

$$\frac{\partial U(r,t)}{\partial t} + \gamma\mu_a U(r,t) + \nabla J(r,t) = q_0(r,t) \qquad [33]$$

$$\nabla U(r,t) + \frac{3\,\partial J(r,t)}{r^2\,\partial t} + \frac{J(r,t)}{\gamma D} = 0 \qquad [34]$$

where $U(r,t)$ is the photon density, $J(r,t)$ is the photon current density, D is the diffusion coefficient, $q_0(r,t)$ is the photon sources function, and

$$U(r,t) = [U(r)]_{dc} + [U(r)]_{ac} e^{[-i(\omega t+\varepsilon)]} \qquad [35]$$

$$J(r,t) = [J(r)]_{dc} + [J(r)]_{ac} e^{[-i(\omega t+\varepsilon)]} \qquad [36]$$

$$D = \frac{1}{3(\mu_a + \mu_s')} \quad [37]$$

$$q_0(r,t) = \delta(r)S\left[1 + Ae^{-i(\omega t+\varepsilon)}\right] \quad [38]$$

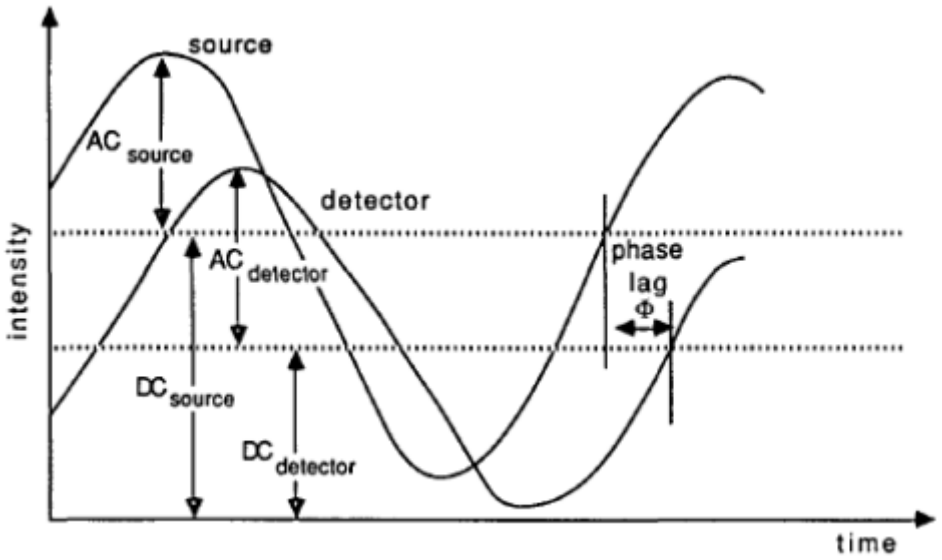

Figure 2.12 The phase (Φ), average intensity (DC detector intensity, I_{dc}) and amplitude of oscillated intensity (AC detector intensity, I_{ac}) were used in frequency domain method.

The expressions of phase ($\mathbf{\Phi}$), average intensity ($\mathbf{I_{dc}}$) and amplitude of oscillated intensity ($\mathbf{I_{ac}}$) were given by:

$$\Phi = \tan^{-1}\left(\frac{\mathrm{Im}[U(r)]_{ac}}{\mathrm{Re}[U(r)]_{ac}}\right) \quad [39]$$

$$I_{dc} = [U(r)]_{dc} \quad [40]$$

$$I_{ac} = \sqrt{(\mathrm{Re}[U(r)]_{ac})^2 + (\mathrm{Im}[U(r)]_{ac})^2} \quad [41]$$

where $\mathrm{Re}[U(r)]_{ac}$ and $\mathrm{Im}[U(r)]_{ac}$ are the real and imagery part of $[U(r)]_{ac}$.

By solving equation [33] and [34] and substituting into equation [39] – [41], it becomes equation [42] – [44]:

$$\Phi = \left[\left(\frac{\gamma^2\mu_a^2 + \omega^2}{\gamma^2 D^2}\right)^{\frac{1}{4}} \sin\left[\frac{1}{2}\tan^{-1}\left(\frac{\omega}{\gamma\mu_a}\right)\right]\right] r \quad [42]$$

$$\ln(rI_{dc}) = -\left(\frac{\mu_a}{D}\right)^{\frac{1}{2}} r + \ln\left(\frac{S}{4\pi\gamma D}\right) \quad [43]$$

$$\ln(rI_{ac}) = -\left(\frac{\gamma^2\mu_a^2 + \omega^2}{\gamma^2 D^2}\right)^{\frac{1}{4}} \cos\left[\frac{1}{2}\tan^{-1}\left(\frac{\omega}{\gamma\mu_a}\right)\right] r + \ln\left(\frac{SA}{4\pi\gamma D}\right) \quad [44]$$

where S_Φ, S_{dc} and S_{ac} are the slopes of above equation [42]-[44]

$$S_\Phi = \left(\frac{\gamma^2\mu_a^2 + \omega^2}{\gamma^2 D^2}\right)^{\frac{1}{4}} \sin\left[\frac{1}{2}\tan^{-1}\left(\frac{\omega}{\gamma\mu_a}\right)\right] \quad [45]$$

$$S_{dc} = -\left(\frac{\mu_a}{D}\right)^{\frac{1}{2}} \quad [46]$$

$$S_{ac} = -\left(\frac{\gamma^2\mu_a^2 + \omega^2}{\gamma^2 D^2}\right)^{\frac{1}{4}} \cos\left[\frac{1}{2}\tan^{-1}\left(\frac{\omega}{\gamma\mu_a}\right)\right] \quad [47]$$

Equation [45]-[47] can then be used to calculate the absorption coefficient (μ_a) and transport scattering coefficient (μ_s').

Using the equation [45] and [47], the absorption coefficient (μ_a) and transport scattering coefficient (μ_s') became equation [48] and [49]:

$$\mu_a = \frac{\omega}{2\gamma}\left(\frac{S_\Phi}{S_{ac}} - \frac{S_{ac}}{S_\Phi}\right) \quad [48]$$

$$\mu_s' = \frac{S_{ac}^2 - S_\Phi^2}{3\mu_a} \quad [49]$$

Using the equation [45] and [46], the absorption coefficient (μ_a) and transport scattering coefficient (μ_s') became equation [50] and [51]:

$$\mu_a = \frac{\omega}{2\gamma}\left[\left(\frac{S_\Phi^2}{S_{dc}^2} - \frac{1}{2}\right)^2 - \frac{1}{4}\right]^{-\frac{1}{2}} \quad [50]$$

$$\mu_s' = \frac{S_{dc}^2}{3\mu_a} \quad [51]$$

Using the equation [46] and [47], the absorption coefficient (μ_a) and transport scattering coefficient (μ_s') became equation [52] and [53]:

$$\mu_a = \frac{\omega}{2\gamma}\left[\left(\frac{S_{ac}^2}{S_{dc}^2} + \frac{1}{2}\right)^2 - \frac{1}{4}\right]^{-\frac{1}{2}} \quad [52]$$

$$\mu_s' = \frac{S_{dc}^2}{3\mu_a} \quad [53]$$

2.6.3. Spatially-resolved method

Matcher (46) proposed that $\mu_a(\lambda)$ can be evaluated if $\mu_s'(\lambda)$ is known. Using diffusion theory, with $\rho \gg z_0$, the expression of the spatial dependence of the reflected intensity becomes equation [54]:

$$R(\rho, \lambda) = z_0 e^{-\mu_{eff}(\lambda)\rho}\left(\mu_{eff}(\lambda) + \frac{1}{\rho}\right) \quad [54]$$

where ρ is the source-detector separation distance, $\mu_{eff}(\lambda)$ is the effective attenuation coefficient and z_0 is the depth where all incident photons are isotropically scattered:

$$z_0 = \frac{1}{\mu_s'(\lambda)} \quad [55]$$

$$\mu_{eff}(\lambda) = \sqrt{3\mu_a(\lambda)\left(\mu_a(\lambda) + \mu_s'(\lambda)\right)} \approx \sqrt{3\mu_a(\lambda)\mu_s'(\lambda)} \quad [56]$$

After the natural logarithm of the equation [54] and differentiating it with respect to ρ , the equation becomes:

$$\frac{\partial \ln\big(R(\rho,\lambda)\big)}{\partial \rho} = -\mu_{eff}\rho + \ln\left(\mu_{eff} + \frac{1}{\rho}\right) \quad [57]$$

As $\mu_{eff} \gg \frac{1}{\rho}$ and $\rho \gg z_0$, $\ln\left(\mu_{eff} + \frac{1}{\rho}\right)$ is the non-linear part of the equation and can be approximated to $\ln\left(\mu_{eff} + \frac{1}{\rho_0}\right)$, therefore

$$\frac{\partial}{\partial \rho}\left[\ln\left(\mu_{eff} + \frac{1}{\rho}\right)\right] \to 0 \quad [58]$$

Then, equation [57] becomes

$$\frac{\partial \ln\big(R(\rho,\lambda)\big)}{\partial \rho} = -\mu_{eff}\rho \quad [59]$$

The relationship between absorbance changes and the reflected intensity at different source-detector distance is:

$$\frac{\partial A(\rho,\lambda)}{\partial \rho} = -\frac{\partial \ln\big(R(\rho,\lambda)\big)}{\partial \rho} \quad [60]$$

Substituting equation [60] into equation [59],

$$\frac{\partial A(\rho,\lambda)}{\partial \rho} = \mu_{eff}\rho \qquad [61]$$

Substituting equation [56] into equation [61], the expression becomes equation [62]:

$$\mu_a(\lambda) = \frac{1}{3\mu_s'(\lambda)}\left(\frac{\partial A(\rho,\lambda)}{\partial \rho} - \frac{2}{\rho}\right)^2 \qquad [62]$$

Therefore, by measuring the absorbance change in different source-detector distance (i.e. $\frac{\partial A}{\partial \rho}$) and with known μ_s' value, $\mu_a(\lambda)$ can be approximated. In a later study by Matcher (47), he performed *in vivo* measures of μ_s' from 760 nm to 900 nm in adult forearm, scalp and calf muscle using time-resolved near infrared spectroscopy. Matcher found that there was linear relationship between $\mu_s'(\lambda)$ and λ. The ratio of $\frac{\mu_s'(\lambda_1)}{\mu_s'(\lambda_2)}$ were about constant among subjects in these regions. The second part of near infrared spectroscopy makes use of $\frac{\mu_a(\lambda_1)}{\mu_a(\lambda_2)}$ to calculate the tissue oxygen saturation. Since $\mu_a(\lambda)$ is inversely proportion to $\mu_s'(\lambda)$ (see equation [62]), it suggested that spatially resolved spectroscopy can also be used to evaluate tissue oxygen saturation once the ratio of $\frac{\mu_s'(\lambda_1)}{\mu_s'(\lambda_2)}$ is known.

2.6.4. Sampling depth

The separation distance between the light source and the detector is an important factor which determines the penetration ability of the NIR spectrometer. Soft tissues are multiple scatters. The detected light comes from multiple optical pathways originated from the light source. Some pathways are more likely than others. Prediction of pathways which have high probabilities of photons passing through, will affect the mean penetration depth of the measurement. Weiss and his colleagues (126) predicted the mean depth of the optical pathways and its relationship with the source-detector separation using Monte Carlo simulations. Cui and Chance (127) measured the mean penetration depth in a tissue phantom under different source-detector separations. Their result showed that the propagation pathway of the incident photons follow a banana shape pathway trajectory towards the detector (Figure 2.13). This propagation reached its maximum depth at the mid-point of the source-detector distance. At this mid-point, the photon density reached the maximum at the depth closed to half of source-detector separation distance. They also showed that the mean penetration depth was approximately equal to half of source-detector separation distance.

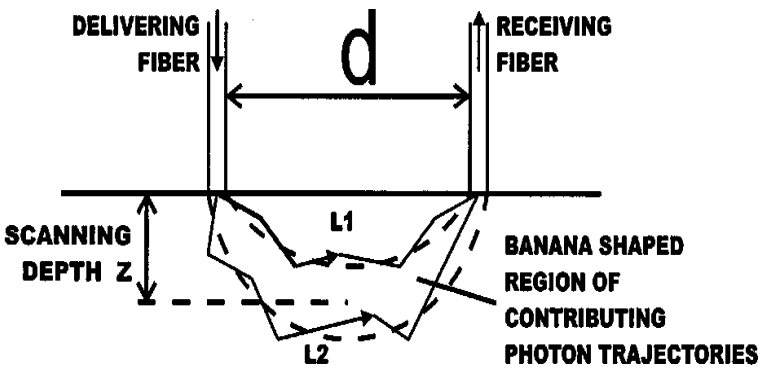

Figure 2.13 The banana shape photon migration region in this source and detector fibers configuration (128).

Feng et al.(129) derived the expression of the photon migration path distribution in a multiple scattering media and verified it using Monte Carlo simulation as well as diffusion theory. In a multiple scattering medium, when light propagates in weak absorption limit ($\delta \gg d$), the expression of the sampling depth is:

$$\text{sampling depth} = \frac{d}{2\sqrt{2}} \qquad [63]$$

When the light propagates in strong absorption limit ($\delta \ll d$), the expression of the sampling depth is

$$\text{sampling depth} = \frac{\sqrt{\delta d}}{2} \qquad [64]$$

where d is the source-detector distance and δ is the penetration depth, defined by:

$$\delta = \frac{1}{\sqrt{3\mu_a(\mu_a + \mu_s')}} = \frac{1}{\sqrt{3\mu_a\mu_s'}} \quad [65]$$

Meglinskii and Matcher (130) modelled the propagation of light with different source-detector distances. The model contained seven tissue layers, including the horny layer, epidermis, dermis with capillary loops, dermis with surface plexus of vessels, dermis, dermis with depth plexus of vessels and hypodermic fat. The optical properties used were obtained from the literature (131). The source-detector distances used were 250, 400 and 800 μm. Meglinskii et al. found that the sampling depth was linearly related to the source-detector distances and this relationship was not affect by the different composition of tissue layers.

By manipulating the source-detector distance of the sensor probe, NIR spectroscopy could provide tissue oxygenation measurement at specific sampling depth with maximum reaching 2 cm depending on the optical properties of the examined region (40, 123, 132, 133). Therefore, this technique has potential for tissue oxygenation monitoring and can be used to assess the viability of tissues for pressure ulcer prevention.

Chapter 3

Methodology

There are three methods to determine oxygen dependent chromophore concentrations in near infrared spectroscopy. These included the time resolved (TD) method, multi-distance frequency domain (FD) method and spatially resolved (SR) method. Of these three methods, the technical requirement of the SR method requires lower cost instrumentations and thus has the potential to develop into a home care device for tissue viability monitoring. To adopt this method for measurement, it requires a linear relationship between the transport scattering coefficients $\left(\mu_s'(\lambda)\right)$ and the wavelength of illuminating light sources (λ) among individual subjects at the examination location. That means the inter-subject variations of transport scattering coefficient ratio at any two wavelengths $\left(\frac{\mu_s'(\lambda_1)}{\mu_s'(\lambda_2)}\right)$ should be as low as possible, such that error introduced to the tissue oxygen saturation calculation can be minimized. In literature, the relationship of transport scattering coefficient and wavelength has been found to be linear in forearm, calf muscle and scalp (47). However, for the anatomical sites of our interest (i.e. areas at high risk of pressure ulcers), such information were not available. Therefore, before the development of our NIR photometer using SR method, an investigation was conducted to evaluate the consistency of $\frac{\mu_s'(\lambda_1)}{\mu_s'(\lambda_2)}$ in the greater trochanter region among subjects using multi-distance frequency domain method. If the inter-subject variation of $\frac{\mu_s'(\lambda_1)}{\mu_s'(\lambda_2)}$ was low, the SR method can be applicable at the greater

trochanter region. Upon the development of the spatially resolved near infrared (SR-NIR) photometer, *in vitro* and *in vivo* experiments were conducted to evaluate the accuracy and the sensitivity of the instrument. Lastly, to examine the response of newly developed photometer to tissue oxygenation changes, *in vivo* measurements were conducted on the forearm before and after a 15 minutes passive exercise through electrical muscle stimulation.

3.1. Evaluation of optical properties, hemoglobin concentration and tissue oxygen saturation in forearm and greater trochanter

3.1.1. Experimental design

Two experiments were performed in this part of the study. All the measurements were performed using a NIR spectrophotometer (Imagent, ISS, USA). The optical probe of the spectrophotometer consists of four transmitters. These transmitters were affixed at 2, 2.5, 3 and 3.5 cm away from the receiver. At each transmitter, two laser diodes emit NIR light at peak wavelengths of 690 nm and 830 nm. A total eight laser diodes were irradiated sequentially with modulation frequency at 110 MHz. The sampling rate of the spectrophotometer is 14.9 Hz. A total of eight parameters including absorption coefficients at 690 nm $\left(\mu_a(690\ \mathrm{nm})\right)$ and 830 nm $\left(\mu_a(830\ \mathrm{nm})\right)$, transport scattering coefficients at 690 nm $\left(\mu_s'(690\ \mathrm{nm})\right)$ and 830 nm $\left(\mu_s'(830\ \mathrm{nm})\right)$, concentrations of oxyhemoglobin ([HbO_2]) and deoxyhemoglobin ([Hb]), total hemoglobin concentration ([tHb]) as well as the tissue oxygen saturation (S_tO_2) were determined by the spectrophotometer using

multi-distance frequency domain method. Before each experiment, calibration was performed by placing the fiber optic probe on a solid phantom (Imagent, ISS, USA) with specific $\mu_a(690\ \text{nm})$ of 0.135 mm^{-1}, $\mu_a(830\ \text{nm})$ of 0.131 mm^{-1}, $\mu_s'(690\ \text{nm})$ of 5 mm^{-1} and $\mu_s'(830\ \text{nm})$ of 4.3 mm^{-1}.

In experiment 1, we examined the optical properties, hemoglobin concentrations and tissue oxygen saturation of both left and right forearms. The result was then compared with reported values from literature to ensure reliability of the instrumentation (47). In experiment 2, measurements of the same parameters were acquired at the left and right greater trochanters. The aim was to examine the consistency of $\frac{\mu_s'(690\ \text{nm})}{\mu_s'(830\ \text{nm})}$ among individual subjects which determines the applicability of using SR method in S_tO_2 measurement at the greater trochanter region.

3.1.2. Measurement on forearm

A total of nine healthy male subjects (aged 22.3 ± 1.6 years old) were recruited for the experiment (Table 3.1). Prior to the experiment, subjects were asked to take 15 minutes rest in a room with temperature set to 25 ℃. They were informed of the details of the experiment and the testing protocol. Verbal consents were obtained before the experiment commenced. During the experiment, subjects were asked to lie supine on an examination bed (Figure 3.1). The measurement probe was affixed on the belly of the flexor digitorum superficialis during wrist flexion. The NIR

spectroscopic measurements from each side of the forearm were taken alternately for 3.5 minutes duration each. Three measurements were obtained on each side of the forearm.

Table 3.1
Subject characteristics in experiment 1.

	Age	Height (m)	Weight(kg)	BMI(kgm^{-2})
subject 1	21	1.63	60	22.6
subject 2	21	1.65	59	21.7
subject 3	21	1.66	61	22.1
subject 4	21	1.82	58	17.5
subject 5	21	1.63	58	21.8
subject 6	24	1.69	60	21
subject 7	24	1.69	63	22.1
subject 8	24	1.63	58	21.8
subject 9	24	1.65	65	22.6
Mean	22.3	1.67	60.2	21.5
Std	1.6	0.06	2.4	1.6

Figure 3.1 Experimental set-up of the forearm measurement. The probe was put on the belly of flexor digitorum superficialis (muscle for wrist flexion) and was affixed by double-sided adhesive tape (red arrow).

3.1.3. Measurement on the greater trochanter

In this part of the experiment, eleven healthy male subjects (aged 22.5 ± 1.8 years old) were recruited (Table 3.2). Eight of them also participated in the experiment described in 3.1.2. Before the experiment, subjects were allowed to rest for 15 minutes in a room with temperature set at 25 ℃. Then, they were asked to adopt a side-lying posture (Figure 3.2). To determine the exact location of the greater trochanter, B-mode ultrasound (SonoSite, Inc., USA) was used to facilitate the fixation of the optical probe (Figure 3.3). The thickness of the tissue overlying the greater trochanter was also recorded (Figure 3.4). Measurements were taken on tissues over both left and right greater trochanter alternately. Measurements of above mentioned parameters were determined from 3.5 minutes of data acquisitions and these measurements were repeated for 3 times in both left and

right limbs. In between measurements, subjects were allowed to resume supine lying for 5 minutes to relieve any loading of tissues at the measurement site (31). Afterwards, the subjects were asked to re-adopt the same side-lying posture with measurement on the opposite side. These procedures were repeated for 3 times.

Table 3.2

Subject characteristics in experiment 2.

					Soft tissue thickness	
	Age	Height (m)	Weight(kg)	BMI(kgm^{-2})	Left	Right
subject 1	26	1.83	72	21.5	2.27	2.6
subject 2	24	1.63	58	21.8	1.1	1.43
subject 3	24	1.69	63	22.1	1.33	1.15
subject 4	22	1.73	61	20.4	1.26	1.15
subject 5	22	1.71	68	23.3	2.09	1.85
subject 6	24	1.69	60	21.0	1.44	1.58
subject 7	21	1.63	58	21.8	1.36	1.33
subject 8	21	1.82	58	17.5	1.45	1.21
subject 9	21	1.66	61	22.1	1.57	1.38
subject 10	21	1.65	59	21.7	1.38	1.21
subject 11	21	1.63	60	22.6	1.4	1.68
mean	22.5	1.7	61.6	21.4	1.51	1.51
Std	1.8	0.07	4.5	1.5	0.35	0.43

Figure 3.2 Experimental set-up of the greater trochanter measurement. The probe was directly contact the skin surface of greater trochanter region located by ultrasound imaging and was affixed by double-sided adhesive tape (red arrow).

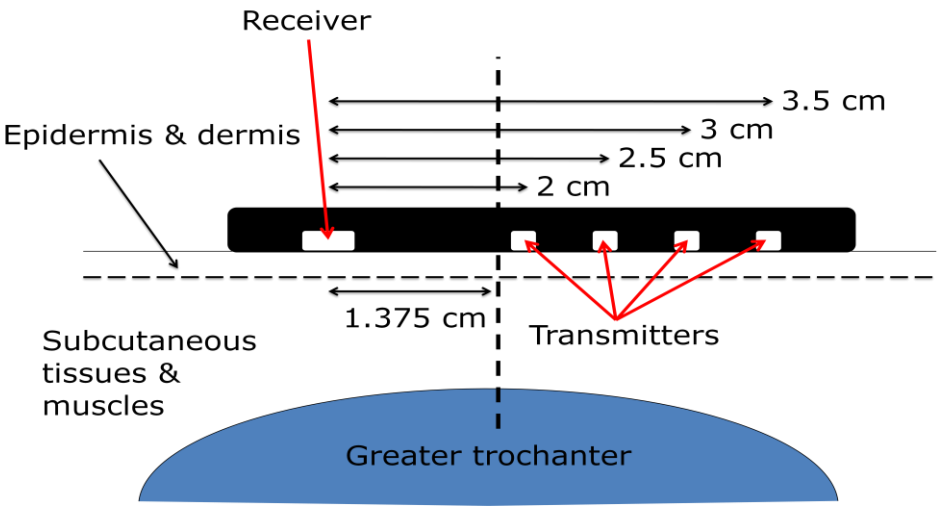

Figure 3.3 An illustration showing the location of measuring probe on greater trochanter. The middle point of average source-detector distance (1.375 cm from the receiver) was aligned with the most superficial point of the greater trochanter based on the ultrasound image.

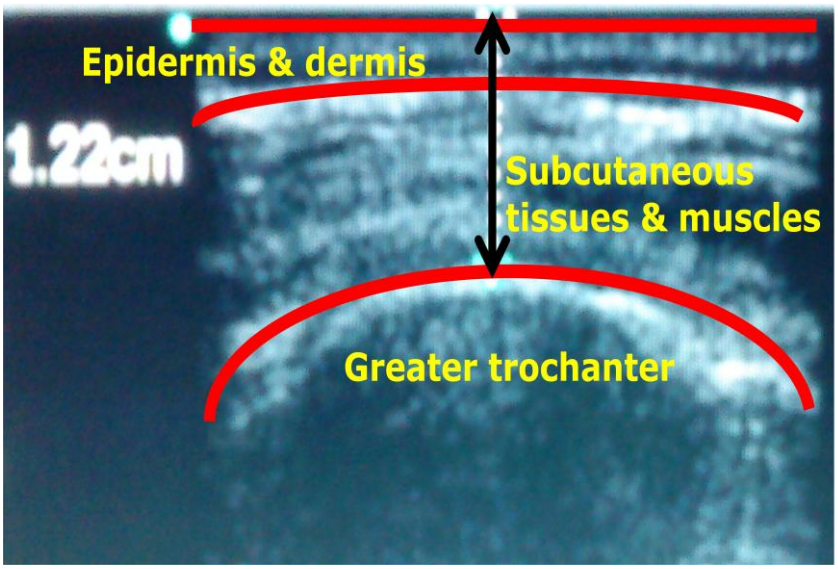

Figure 3.4 An example of thickness measurement in ultrasound image. The thickness was measured from the epidermis surface to the outer point of the greater trochanter (black arrow).

3.1.4. Data analysis

The data of all parameters recorded during each trial were averaged. Paired *t*-tests were performed to compare the parameters between the left and right forearm as well as between tissues overlying the left and right greater trochanter. Independent *t*-tests were examined between the forearm flexor digitorum superficial tissues and tissues overlying greater trochanter.

3.2. Development of the spatially resolved Near Infrared (SR-NIR) photometer

A SR-NIR photometer was constructed for tissue oxygenation measurement. Figure 3.5 showed the configuration of the required instrumentation. The measurement probe contained an optical fiber connected to a laser source, which was located at 6.5 mm and 13 mm away from two photodetectors. Based on the equation [63] from Feng et al. (129), the sampling depth was $\frac{\sqrt{2}}{4}$ times of average source-detector distance (i.e. 3.4 mm). Since the skin thicknesses of forearm and thigh were on average 1.3 mm (ranged from 0.6 to 1.7 mm, data from 75 females and 65 males, 104 subjects under 65 years old and 36 subjects over 65 years old) (134) and 1.55 mm (ranged from 1.49 to 1.72 mm, data from 205 women and 137 men aged 18–70 years including Caucasian, Asian and Black) (135), we believed that the sampling depth of this photometer could reach the subcutaneous tissues underlying the dermis. The maximum source-detector distance that we used in this study was limited by the magnitude of the reflected signal obtained from our tissue phantom (details will be explained in section 3.3.).

In our setup, the required near infrared light was delivered from a commercial near infrared spectrophotometer (Oxymon, Artinis Medical Systems B.V., Nederlands). This spectrophotometer contained two “CLASS I” lasers with wavelengths at 856 ± 10 nm and 765 ± 15 nm. The peak laser powers emitted at the fiber tip (2.8 mm diameter) are 5.5 and 5.4 W at 856 and 765 nm respectively. These lasers were

pulsed at 4 kHz with 70 ns of full width at half maximum. The first pulse was from the laser at 856nm, followed by the one at 765 nm with a phase difference of 50 μs. These lasers were pulsed at short duration in order to lower down the light absorption in the illuminated tissues in which light energy was converted to heat.

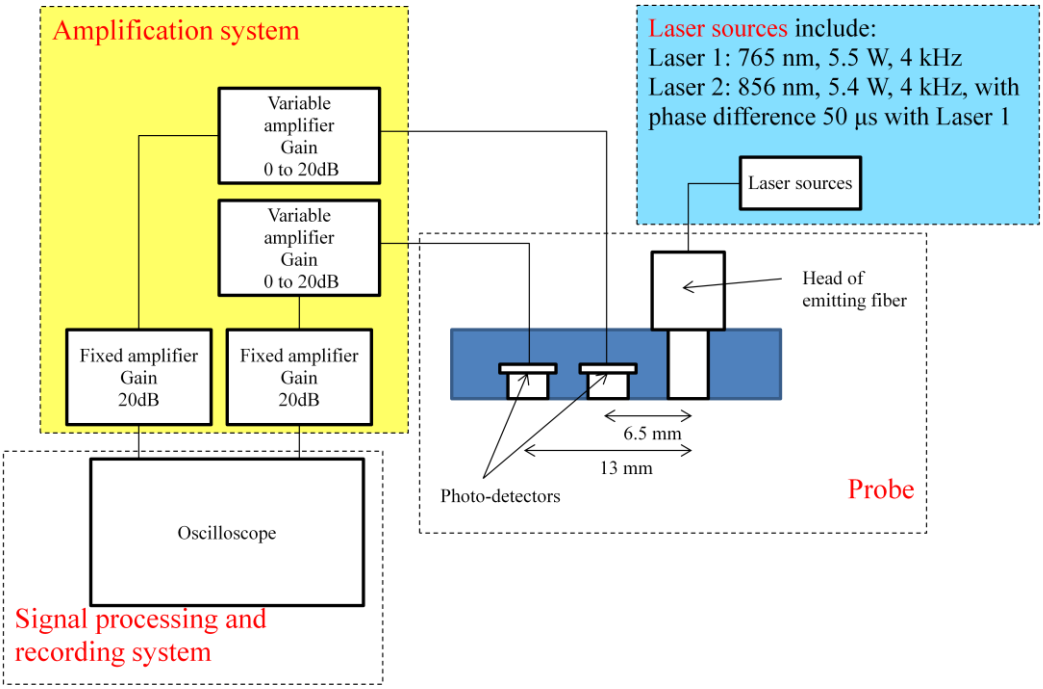

Figure 3.5 The system configuration of the SR-NIR photometer.

The diffuse reflected light after travelling along the tissues was received by the two photodetectors (OSI series 5T, OSI Optoelectronics, Malaysia) with operation range in near infrared region (Figure 3.6). The light passed through a glass window, followed by a focal lens and finally focused to the 1 mm^2 sensing area in each photodetector. Voltage responses ranged from 0 to 12 V was generated according to

the received light intensity. The voltage signal was then amplified by a variable amplifier (0 to 20 dB gain) and a fixed amplifier (20 dB gain) to ensure the output signals from the two photodetectors have the same amplification. The waveforms of these two signals were then recorded by an oscilloscope. In order to improve the signal to noise ratio, we averaged 128 waveforms acquired from each detector.

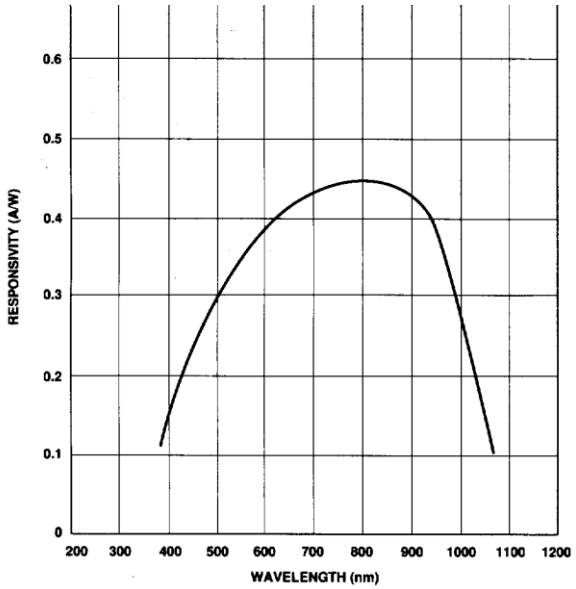

Figure 3.6 The spectral characteristics of the photodetectors. The operation voltage is ranged from 0 to 12V. The voltage response of the photodetectors to light wavelength is highest in near-infrared region, 700 to 900nm.The voltage response of light at 765 nm is similar to that at 856 nm (OSI series 5T, OSI Optoelectronics, Malaysia).

The peak values of the averaged waveform from each photodetectors were extracted using MATLAB R2008a (Mathworks, USA). These values represent the reflected light intensities at 765 nm and 856 nm from the illuminated tissues. By

using spatial resolved method, the acquired values can form four equations based on equations [60] and [62]. These equations can then be used to evaluate the absorption coefficient at 765 nm, $\mu_a(765\ \mathrm{nm})$ and the absorption coefficient at 856nm, $\mu_a(865\ \mathrm{nm})$. The four simultaneous equations were:

$$\frac{\partial \mathrm{A}(765\ \mathrm{nm})}{\partial \rho} = \left(\frac{\ln \mathrm{R}(6.5\ \mathrm{mm}, 765\ \mathrm{nm}) - \ln \mathrm{R}(13\ \mathrm{mm}, 765\ \mathrm{nm})}{\partial \rho}\right) \qquad [66]$$

$$\frac{\partial \mathrm{A}(856\ \mathrm{nm})}{\partial \rho} = \left(\frac{\ln \mathrm{R}(6.5\ \mathrm{mm}, 856\ \mathrm{nm}) - \ln \mathrm{R}(13\ \mathrm{mm}, 856\ \mathrm{nm})}{\partial \rho}\right) \qquad [67]$$

$$\mu_a(765\ \mathrm{nm}) = \frac{1}{3\mu_s'(765\ \mathrm{nm})}\left(\frac{\partial \mathrm{A}(765\ \mathrm{nm})}{\partial \rho} - \frac{2}{\rho}\right)^2 \qquad [68]$$

$$\mu_a(856\ \mathrm{nm}) = \frac{1}{3\mu_s'(856\ \mathrm{nm})}\left(\frac{\partial \mathrm{A}(856\ \mathrm{nm})}{\partial \rho} - \frac{2}{\rho}\right)^2 \qquad [69]$$

where $\mathrm{R}(13\ \mathrm{mm}, 765\ \mathrm{nm})$ and $\mathrm{R}(6.5\ \mathrm{mm}, 765\ \mathrm{nm})$ are the reflected light intensities at wavelength of 765 nm measured at source-detector distance of 6.5 mm and 13 mm respectively, $\mathrm{R}(13\ \mathrm{mm}, 856\ \mathrm{nm})$ and $\mathrm{R}(6.5\ \mathrm{mm}, 856\ \mathrm{nm})$ are the reflected light intensities at wavelength of 856 nm measured at source-detector distance of 6.5 mm and 13 mm respectively. $\partial\rho$ is the difference of source-detector distances (i.e. 6.5 mm mm in our setup), ρ is the average value of source-detector distances (i.e. 9.5 mm in our setup). Thereafter, tissues oxygen saturation (S_tO_2) can be calculated by equation [70]-[74] based on equation [18]:

$$S_tO_2 = \frac{a_1 \frac{\mu_a(765\ \text{nm})}{\mu_a(856\ \text{nm})} - a_2}{a_3 \frac{\mu_a(765\ \text{nm})}{\mu_a(856\ \text{nm})} - a_4} \times 100\% \quad [70]$$

$$a_1 = \varepsilon_{Hb}(856\ \text{nm}) \quad [71]$$

$$a_2 = \varepsilon_{Hb}(765\ \text{nm}) \quad [72]$$

$$a_3 = \left(\varepsilon_{Hb}(856\ \text{nm}) - \varepsilon_{HbO_2}(856\ \text{nm})\right) \quad [73]$$

$$a_4 = \left(\varepsilon_{Hb}(765\ \text{nm}) - \varepsilon_{HbO_2}(765\ \text{nm})\right) \quad [74]$$

where the values of $\varepsilon_{HbO_2}(765\ \text{nm})$, $\varepsilon_{Hb}(765\ \text{nm})$, $\varepsilon_{HbO_2}(856\ \text{nm})$ and $\varepsilon_{Hb}(856\ \text{nm})$ are 0.36597, 0.14749 and 0.1823 $\mu M^{-1}mm^{-1}$ respectively. These values are adopted from the *in vitro* measurement by Cope (117), which were commonly adopted by other NIR spectroscopic systems (37, 41, 42, 136).

3.3. Validation of tissue oxygen saturation measurement of the SR-NIR photometer in blood-Intralipid tissue phantom using blood gas analyzer

To validate the tissue oxygen saturation measured by the newly developed SR-NIR photometer, a tissue phantom composed of fresh human blood and Intralipid-10%

was constructed according to Suzuki (137). Ethical approval was granted by Human Subjects Ethics Sub-committee of Hong Kong Polytechnic University. In literatures, several materials have been used to simulate the scattering properties of tissue. These included milk, polymer microspheres, quartz glass microspheres, Intralipid-10%, Titanium dioxide (TiO_2) and Aluminium oxide (Al_2O_3) powder (138-142). Of all these scattering materials, Intralipid-10% was chosen because it is commercially available and more economical. In order to conduct our experiment, we have made several modifications in our tissue phantom. First, the concentration of Intralipid-10% was from 50 mlL^{-1} to 60 mlL^{-1}. The modification was performed to allow our phantom to have transport scattering coefficient (μ_s') similar to the greater trochanter region. The $\mu_s'(756\ \mathrm{nm})$ and $\mu_s'(856\ \mathrm{nm})$ in our tissue phantom were 6.7 cm^{-1} and 5.9 cm^{-1} respectively. These values were calculated using the equation [10] as well as [75] and [76] by van Staveren (143) , which were also used in other related studies (144-146):

$$\mu_s(\lambda) = 16\lambda^{-2.4}[\mathrm{Intralipid}] \quad [75]$$

$$g(\lambda) = 1.1 - 0.58\lambda \quad [76]$$

where $[\mathrm{Intralipid}]$ is the volume fraction of Intralipid-10%, the units of $\mu_s(\lambda)$, λ and $[\mathrm{Intralipid}]$ are mm^{-1}, μm and mlL^{-1}

Second, owing to the limitations of the available blood gas analyzer (GEM Premier 3000, Instrumentation Laboratory, USA), we have to use plasma instead of saline solution to dilute the blood for our phantom. Moreover, the analyzer also restricted the blood cell volume to above 15% for measurement of oxygen saturation. In this case, our blood sample can only be diluted to half of the whole blood concentration (normal blood cell volume was about 40%). This limitation could induce much higher NIR light absorption than normal tissues and thus the penetration depth of the device would be reduced.

Figure 3.7-3.9 showed the experimental set-up. Before the experiment, the gas switches of Chamber 1 and 2 were opened to allow nitrogen gas to perfuse the two chambers for 10 minutes. Afterwards, all gas switches were closed. Then, 150 ml of fresh whole blood was extracted from a human donor and stored in heparin tubes. 100 ml of whole blood was immediately centrifuged at 3000 rpm for 15 minutes. 50 ml of plasma on superficial layer after centrifugation was extracted and the remaining 50 ml residual was discharged. The plasma together with the 50 ml of whole blood were mixed and transferred to the container in Chamber 1. The delivery was done by using syringe and needle in order to prevent contact with air. The blood sample was stirred at 50 rpm in the container inside Chamber 1. After 10 minutes, 47 ml of plasma diluted blood from Chamber 1 and 3 ml Intralipid-10% were extracted and transferred to the container in Chamber 2. The overall

concentration of Intralipid-10% in blood-Intralipid mixture was 60 mlL^{-1}. The mixture in Chamber 2 was also stirred at 50 rpm.

After 10 minutes of stirring, data recording was begun. Three 0.3 ml plasma diluted blood samples were sequentially extracted from Chamber 1 for oxygen saturation measurement using a blood gas analyzer (GEM Premier 3000, Instrumentation Laboratory, US) (Figure 3.10). At the same time, 20 datasets of blood oxygenation measurements were acquired by the new SR-NIR photometer from the blood-Intralipid phantom in Chamber 2. Under the same controlled environment in Chamber 1 and 2, the changes of oxygen level in blood samples within the two chambers due to cellular metabolism were assumed to be the same. Blood oxygen saturation was checked with the blood gas analyzer every 30 minutes using 3 blood samples from Chamber 1. When the oxygen saturation was reduced by 5%, another 20 datasets of oxygenation measurements using the SR-NIR photometer were recorded on the blood-Intralipid phantom. This procedure was repeated until there was no further decrease in blood oxygenation beyond 5% within 4 hours. Then, the chambers were opened to expose the blood samples to air for 30 minutes and blood oxygenations of the two solutions were measured using the SR-NIR photometer as well as the blood gas analyzer. Tissue oxygen saturations of the blood-Intralipid tissue phantom at different time points were calculated using the acquired datasets from the SR-NIR photometer with the method described in section 3.2. The results were compared with those obtained from the blood gas analyzer.

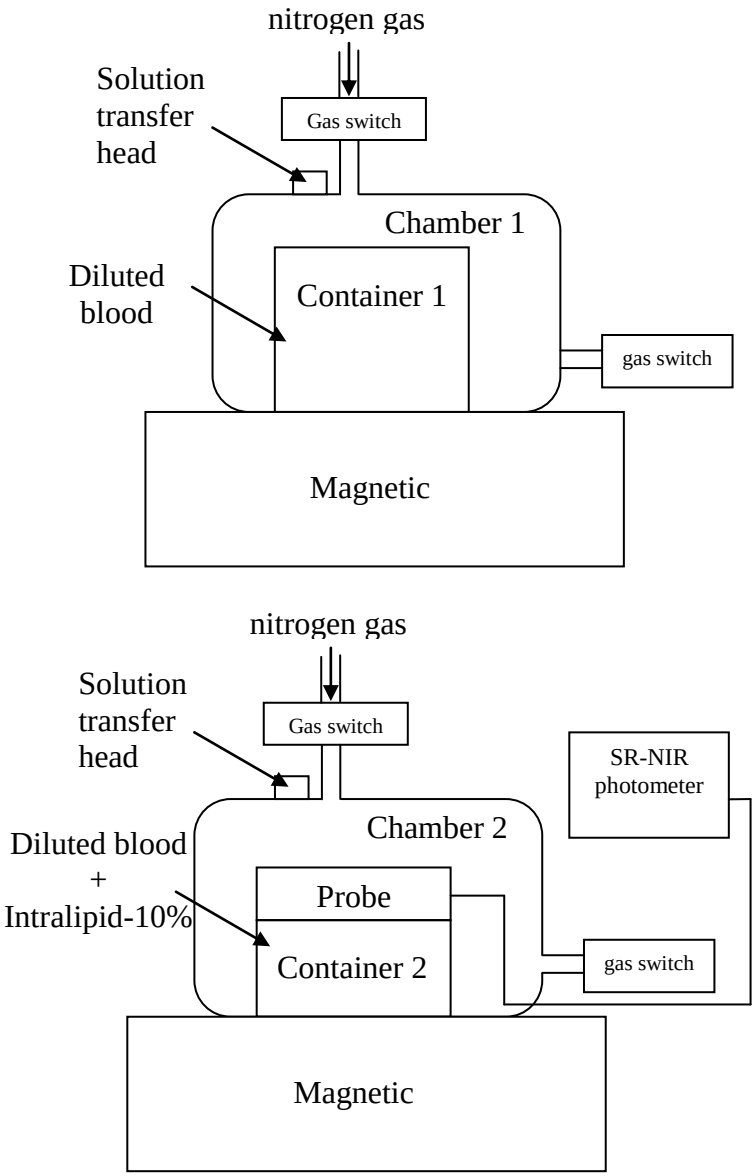

Figure 3.7 A diagram of the tissue phantom. There were two closed chambers (Chamber 1 and Chamber 2) separately on two magnetic stirrers. Inside Chamber 1, there was a 120 ml container containing the diluted blood mixture and magnetic stirrer bar. Inside Chamber 2, there was a 50 ml container containing the diluted blood-Intralipid mixture and magnetic stirrer bar.

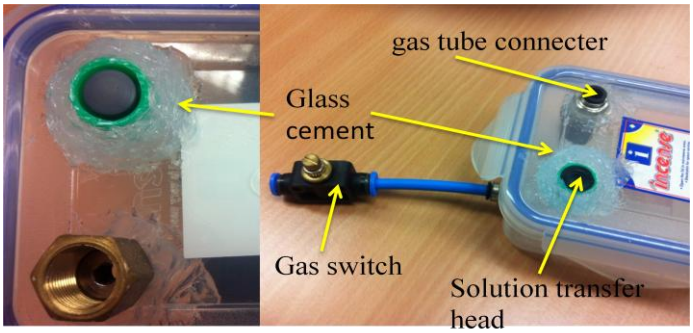

Figure 3.8 The design of Chamber 1 and Chamber 2. The cover of each chamber was inserted with a solution transfer head and a gas tube connector. A gas tube connector was also inserted to the size of the chamber. All the edges were filled with glass cement to prevent gas leakage. The gas tube connector in the cover was connected to a gas switch and then to nitrogen compressed gas cylinder (R-size nitrogen gas, Hong Kong Oxygen Acetylene Ltd, Hong Kong). The gas tube connector in chamber side was connected to a gas switch for gas outlet. The solution transfer head was a heparin tube cap. The transfer of any solution was done only by using syringes and needles. The whole system ensured there wasn't any contact between the solution and air from environment. The maximum size of needles (21 gauges) was used in each transfer of solution in order to avoid lying of the blood cells when the blood passed through the needle.

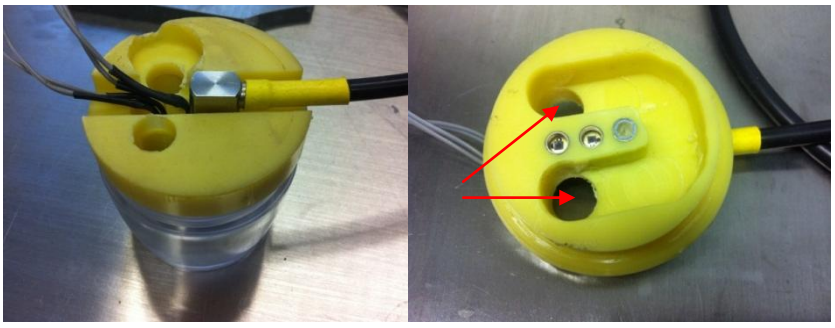

Figure 3.9 The design of probe and container 2 in Chamber 2. The source fiber and photodetectors were held on the cover of the container at source-detector distances of 6.5 mm and 13 mm. The positions of holes (red arrows) were concentric with needle transfer head and gas tips on the cover of Chamber 2.

Figure 3.10 A diagram illustrating the measurement in blood gas analyzer. The probe of the blood gas analyzer extracted 150 μl samples from the syringe and measured the oxygen saturation. Tissue oxygen saturation of the blood sample was determined automatically by the blood gas analyzer.

3.4. Examination of forearm flexor muscle oxygenation before and after electrical muscle stimulation using SR-NIR photometer

To evaluate the performance of the SR-NIR photometer, eleven healthy subjects (4 males and 7 females) aged 21.5 ± 1.4 years old were recruited to participate in the experiment (Table 3.3). They were asked not to engage in any vigorous exercise within 24 hours before the experiments. Before measurements were conducted, they were asked to have 15 minutes rest. They were informed of the testing protocol and verbal consents were obtained. Room temperature was set to 25 ℃. With their right arms positioned comfortably on a table, the sensor probe of the SR-NIR photometer was affixed onto the surface of flexor digitorum superficialis using

double-sided adhesive tape. Baseline measurements of muscle oxygenation were estimated from 15 datasets. The location of the sensor probe was carefully marked before it was temporary removed. Then, 15 minutes of passive exercise was applied to the flexor digitorum superficialis by electrical muscle stimulation (Figure 3.11). After such exercise, the sensor probe was reattached to conduct tissue oxygenation measurement again.

Tissue oxygen saturation was then calculated using the algorithm mentioned in section 3.2. Based on the equation from Matcher (47), the $\mu_s'(756\ \text{nm})$ and $\mu_s'(856\ \text{nm})$ of forearm were 7.1 cm^{-1} and 6.6 cm^{-1}, respectively. Paired *t*-test was performed to compare the oxygen saturation before and after the passive exercise.

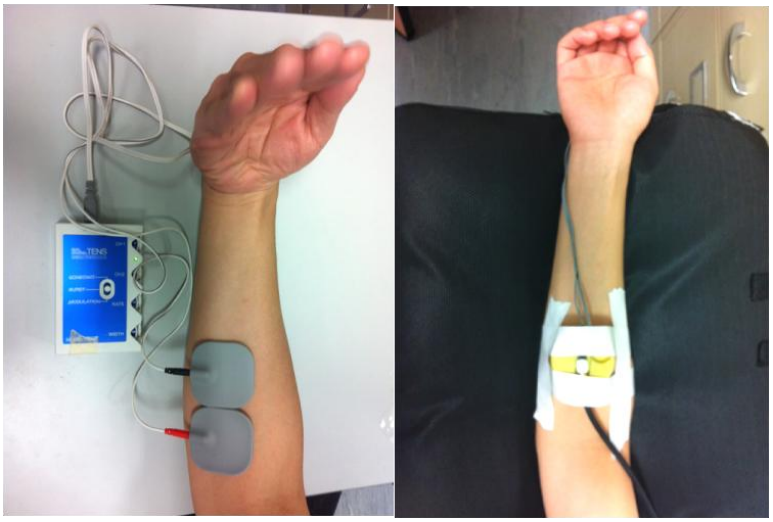

Figure 3.11 The position of electrical stimulation pads and the probe of the SR-NIR photometer. Electric pulse at 20 Hz was used to stimulate the muscles. The amplitude of the pulse was set until there were the successive passive wrist flexion.

Table 3.3

Subject characteristics in forearm examination.

	Age	Gender	Height (m)	Weight (kg)	BMI (kgm^{-2})
subject 1	23	M	1.68	63	22.3
subject 2	21	F	1.55	45	18.7
subject 3	25	F	1.62	48	18.3
subject 4	20	F	1.6	52	20.3
subject 5	21	F	1.59	47	18.6
subject 6	21	F	1.55	50	20.8
subject 7	21	F	1.58	45	18.0
subject 8	21	F	1.6	54	21.1
subject 9	21	M	1.66	68	24.7
subject 10	21	M	1.65	64	23.5
subject 11	22	M	1.69	65	22.8
Mean	21.5		1.62	54.6	20.8
Std	1.4		0.05	8.7	2.3

Chapter 4

Results

4.1. Evaluation of optical properties, hemoglobin concentration and tissue oxygen saturation in forearm and greater trochanter

The absorption coefficients (μ_a), transport scattering coefficients ($\mu_s'(690\ \text{nm})$ and (μ_s') of tissues at the forearm and greater trochanter regions using laser irradiation at 690 nm and 830 nm and the associated blood oxygenation parameters including: concentrations of oxyhemoglobin and deoxyhemoglobin ([HbO_2] and [Hb]), total hemoglobin concentration ([tHb]) as well as the tissue oxygen saturation (S_tO_2) were shown in Table 4.1 and Table 4.2 respectively. Comparisons of these parameters between the left and right side using paired *t*-test showed no significant difference (p>0.05) except the concentration of oxyheomglobin ([HbO_2]) at the greater trochanter (p=0.047), where the right side was significantly higher.

To examine the variation of tissue optical properties, hemoglobin concentrations and tissue oxygen saturation between different anatomical sites, independent *t*-test was used to perform statistical evaluations (Table 4.3). The results showed that all the measured parameters were anatomical site dependent. The $\mu_a(690\text{nm})$ and $\mu_a(830\text{nm})$ in forearm were on average 0.20 ± 0.03 cm^{-1} and 0.21 ± 0.02 cm^{-1}, which were 2.9-fold and 2.6-fold of those in greater trochanter (on average 0.07 ± 0.03 cm^{-1} and 0.08 ± 0.03 cm^{-1} respectively. The $\mu_s'(690\text{nm})$ and $\mu_s'(830\text{nm})$ in

greater trochanter were approximately 7.2 ± 1.7 cm^{-1} and 6.5 ± 1.6 cm^{-1}, which were 1.5-fold and 2.1-fold of those in forearm (4.7 ± 0.5 cm^{-1} and 3.1 ± 0.3 cm^{-1} respectively). The [HbO_2], [Hb] and [tHb] in the forearm were 3.5-fold, 2.3-fold and 2.6-fold of those in greater trochanter. The S_tO_2 in greater trochanter was 1.1-fold of those in forearm. Table 4.4 and Table 4.5 showed the mean, standard deviation and range of all the measured tissue optical properties, hemoglobin concentrations and tissue oxygen saturation in forearm and greater trochanter regions. According to our findings, the ratio of the transport scattering coefficients at the two wavelengths, $\frac{\mu_s'(690\ \mathrm{nm})}{\mu_s'(830\ \mathrm{nm})}$ showed consistent among eleven subjects measured from the greater trochanter. The range of deviation from its average value was 13% to 19%. The standard deviation of this parameter in greater trochanter among eleven subjects region was 0.09, which was 8.3% of the average value. This inter-subject variation was comparable to those found in other regions (forearm, scalp and calf muscle) as reported by Matcher (28% in forearm, 13% in scalp and 21% in calf muscle) (47).

Table 4.1

Comparison of the tissues optical properties, hemoglobin concentrations and tissue oxygen saturation between left and right forearm (n = 9).

Parameters	Left	Right	Percentage difference
$\mu_a(690nm)$	0.2 ± 0.03 cm^{-1}	0.2 ±0.04 cm^{-1}	2.9 ± 17.7%
$\mu_a(830nm)$	0.2 ± 0.02 cm^{-1}	0.2 ± 0.04 cm^{-1}	1.6 ± 13.4%
$\mu_s'(690\ nm)$	4.8 ± 0.4 cm^{-1}	4.5 ± 0.9 cm^{-1}	7.4 ± 14.5%
$\mu_s'(830\ nm)$	3.3 ± 0.3 cm^{-1}	3 ± 0.6 cm^{-1}	10.8 ± 19.4%
$\mu_s'(690\ nm)/\mu_s'(830\ nm)$	1.48 ± 0.10	1.52± 0.14	-2.5 ± 7.8%
[Hb]	32.7 ± 6.5 μM	32.7 ± 4.2 μM	-0.3 ± 14.4%
$[HbO_2]$	60.4 ± 7.8 μM	62.2 ± 9.7 μM	-2 ± 13.3%
[tHb]	93.1 ± 10.5 μM	94.9 ± 12.6 μM	-1.4 ± 10.9%
S_tO_2	64.8 ± 5.1%	65.3 ± 2.9%	-0.8 ± 6.1%

Table 4.2

Comparison of the tissue optical properties, hemoglobin concentrations and tissue oxygen saturation between left and right greater trochanter (n = 11).

Parameters	Left	Right	Percentage difference
Tissue thickness	1.51 ± 0.35 cm	1.51 ± 0.43 cm	2.4 ± 15.1%
$\mu_a(690nm)$	0.06 ± 0.03 cm^{-1}	0.07 ±0.04 cm^{-1}	-5 ± 26.3%
$\mu_a(830nm)$	0.07 ± 0.03 cm^{-1}	0.09 ± 0.04 cm^{-1}	-9.4 ± 25.2%
$\mu_s'(690\ nm)$	7.1 ± 1.7 cm^{-1}	7.0 ± 1.6 cm^{-1}	1.9 ± 17.5%
$\mu_s'(830\ nm)$	6.6 ± 1.5 cm^{-1}	6.5 ± 1.4 cm^{-1}	1 ± 14.4%
$\mu_s'(690\ nm)/\mu_s'(830\ nm)$	1.09 ± 0.09	1.08 ± 0.1	0.6 ± 4.3%
[Hb]	8.6 ± 4.6 μM	9.6 ± 5.5 μM	-1.5 ± 30.3%
$[HbO_2]$	23.4 ± 9.4 μM	28.4 ± 13.2 μM	-10.9 ± 26.4%
[tHb]	31.9 ± 12.8 μM	38.1 ± 17.9 μM	-9 ± 25.1%
S_tO_2	73.7 ± 7.5%	75.6 ± 6.5%	-2.4 ± 6.4%

Table 4.3

Comparison of tissue optical properties, hemoglobin concentrations and tissue oxygen saturation between forearm and greater trochanter (n = 8).

Parameters	Average left and right forearm	Average left and right greater trochanter	Percentage difference
$\mu_a(690nm)$	0.20 ± 0.03 cm^{-1}	0.07 ± 0.03 cm^{-1}	-67.9 ± 11.2%
$\mu_a(830nm)$	0.21 ± 0.02 cm^{-1}	0.08 ± 0.03 cm^{-1}	-60.3 ± 13%
$\mu_s'(690\ nm)$	4.7 ± 0.5 cm^{-1}	7.2 ± 1.7 cm^{-1}	55.4 ± 41.9%
$\mu_s'(830\ nm)$	3.1 ± 0.3 cm^{-1}	6.5 ± 1.6 cm^{-1}	110.9 ± 53.3%
$\mu_s'(690\ nm)/\mu_s'(830\ nm)$	1.51 ± 0.08	1.10 ± 0.08	-27.2 ± 3%
$[Hb]$	33.0 ± 5.0 μM	9.4 ± 4.0 μM	-71.8 ± 10.1%
$[HbO_2]$	61.5 ± 7.0 μM	26.9 ± 10.3 μM	-56.8 ± 13.3%
$[tHb]$	94.5 ± 9.7 μM	36.4 ± 13.2 μM	-61.9 ± 12.2%
S_tO_2	65.0 ± 3.5%	74.2 ± 5.6%	14.2 ± 5.4%

Table 4.4

Mean, standard deviation and range of the tissues optical properties, hemoglobin concentrations and tissue oxygen saturation of forearm.

Parameters	Mean ± std	Range
$\mu_a(690nm)$	0.20 ± 0.03 cm^{-1}	0.16 cm^{-1} to 0.23 cm^{-1}
$\mu_a(830nm)$	0.20 ± 0.03 cm^{-1}	0.16 cm^{-1} to 0.24 cm^{-1}
$\mu_s'(690\ nm)$	4.6 ± 0.7 cm^{-1}	2.7 cm^{-1} to 3.8 cm^{-1}
$\mu_s'(830\ nm)$	3.1 ± 0.5 cm^{-1}	4.1 cm^{-1} to 5.9 cm^{-1}
$\mu_s'(690\ nm)/\mu_s'(830\ nm)$	1.50 ± 0.12	1.35 to 1.66
$[Hb]$	32.8 ± 4.7 Mm	26 μM to 39 μM.
$[HbO_2]$	61.2 ± 6.7 μM	48 μM to 72 μM
$[tHb]$	93.9 ± 9.3 μM	74 μM to 104 μM
S_tO_2	65.0 ± 4.1%	60.6 % to 71.1%

std = standard deviation

Table 4.5

Mean, standard deviation and range of the tissues optical properties, hemoglobin concentrations and tissue oxygen saturation of greater trochanter.

Parameters	Mean ± std	Range
Tissue thickness	1.51 ± 0.4 cm	1.1 cm to 2.6 cm
$\mu_a(690nm)$	0.06 ± 0.03 cm^{-1}	0.02 cm^{-1} to 0.11 cm^{-1}
$\mu_a(830nm)$	0.07 ± 0.03 cm^{-1}	0.04 cm^{-1} to 0.13 cm^{-1}
$\mu_s'(690\ nm)$	7.0 ± 1.7 cm^{-1}	5.0 cm^{-1} to 9.6 cm^{-1}
$\mu_s'(830\ nm)$	6.5 ± 1.5 cm^{-1}	5.3 cm^{-1} to 10.5 cm^{-1}
$\mu_s'(690\ nm)/\mu_s'(830\ nm)$	1.08 ± 0.09	0.89 to 1.22
[Hb]	8.6 ± 4.6 μM	2 μM to 19 μM
$[HbO_2]$	23.4 ± 9.4 μM	4 μM to 43 μM
[tHb]	31.9 ± 12.8 μM	9 μM to 51 μM
S_tO_2	74.6 ± 7.0%	66.4% to 88.0%

std = standard deviation

4.2. Validation of tissue oxygen saturation measurement of the SR-NIR photometer using a blood-Intralipid tissue phantom and by blood gas analyzer

Tissue oxygen saturation measurements obtained at different time points from the blood-Intralipid phantom and whole blood using the newly developed SR-NIR photometer and a commercial blood gas analyzer were listed in Table 4.6. Figure 4.1 showed the comparison of oxygen saturations measured from the SR-NIR photometer and the blood gas analyzer. The correlation coefficient (r^2) between the two measurements was 0.9718. Figure 4.2-4.8 showed the oxygen saturation values measured by SR-NIR photometer and the blood gas analyzer at the same time internal. Deviations from the values of blood gas analyzer were within 5% and the

maximum deviation was 7.5%.

Table 4.6

Tissue oxygen saturation measured by blood gas analyzer and the SR-NIR photometer.

The blood gas analyzer	The SR-NIR photometer
90.3 ± 2.1%	90.9 ± 3.1%
82.0 ± 1.0%	81.1 ± 2.3%
74.7 ± 1.5%	75.2 ± 2.2%
65.9 ± 1.2%	65.9 ± 2.0%
62.0 ± 3.0%	61.7 ± 2.0%
58.0 ± 1.0%	55.7 ± 1.6%
96.7 ± 0.6%	97.0 ± 1.9%

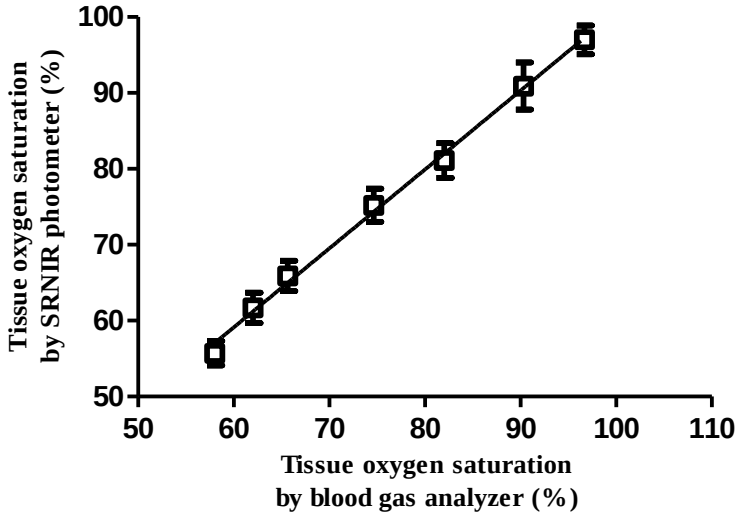

Figure 4.1 Comparison of oxygen saturation values measured by the SR-NIR photometer and blood gas analyzer.

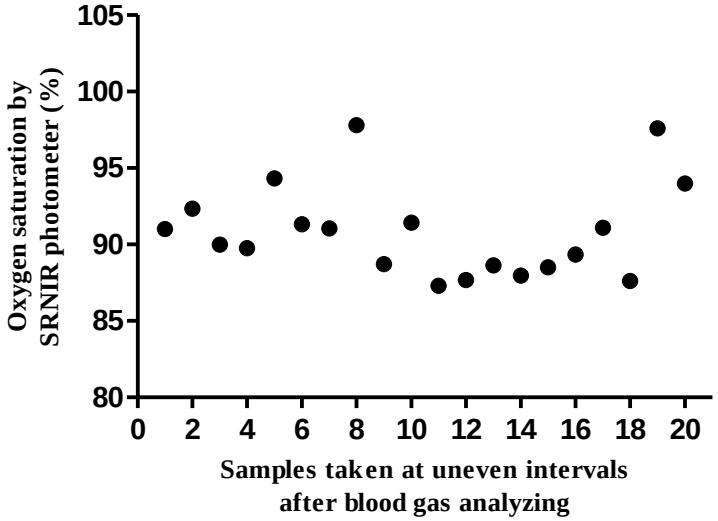

Figure 4.2 The oxygen saturation values measured by the SR-NIR photometer (90.9 ± 3.1%) when the blood oxygen saturation was at 90.3%. The deviations were ranged from -3.0% to 7.5% (n = 20).

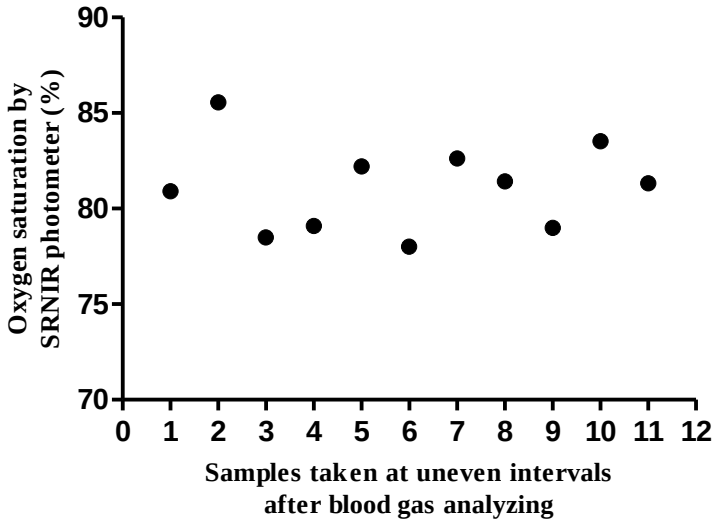

Figure 4.3 The oxygen saturation values measured by the SR-NIR photometer (81.1 ± 2.3%) when the blood oxygen saturation was at 82.0%. The deviations were ranged from -4.0% to 3.6% (n = 11, less than 20 data sets due to human mistake in recording data from the oscilloscope).

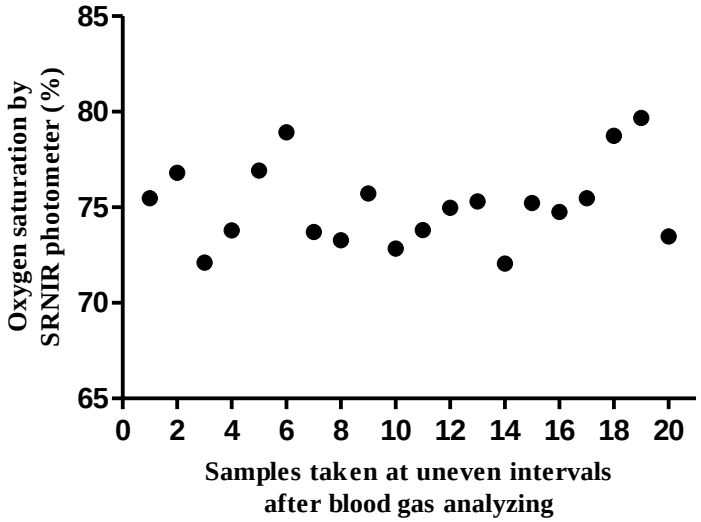

Figure 4.4 The oxygen saturation values measured by the SR-NIR photometer (75.2 ± 2.2%) when the blood oxygen saturation was at 74.7%. The deviations was ranged from -2.6% to 5.0% (n = 20).

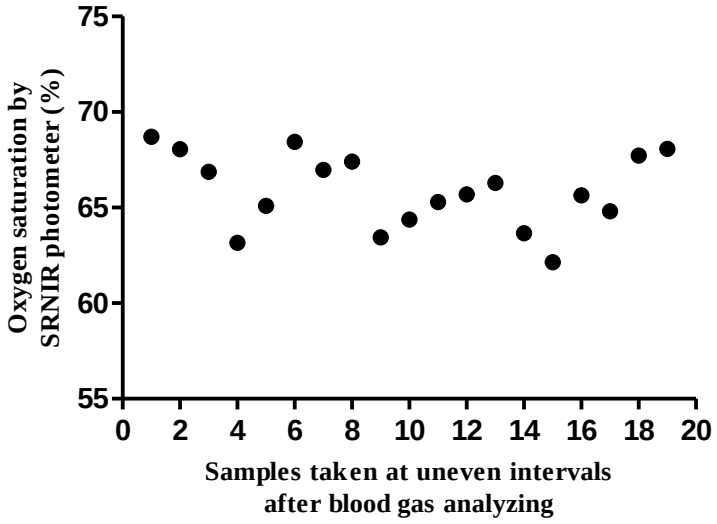

Figure 4.5 The oxygen saturation values measured by the SR-NIR photometer (65.9 ± 2.0%) when the blood oxygen saturation was at 65.7%. The deviations were ranged from -3.5% to 3.0% (n = 20).

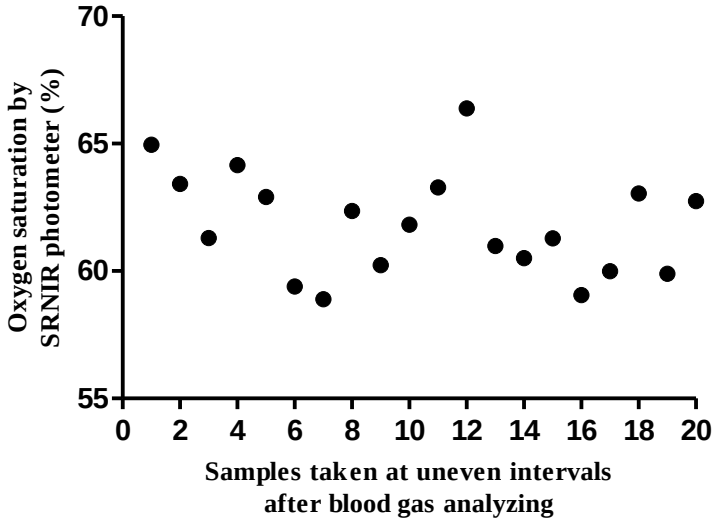

Figure 4.6 The oxygen saturation values measured by the SR-NIR photometer (61.7 ± 2.0%) when the blood oxygen saturation was at 62.0%. The deviations were ranged from -3.1% to 4.4% (n = 20).

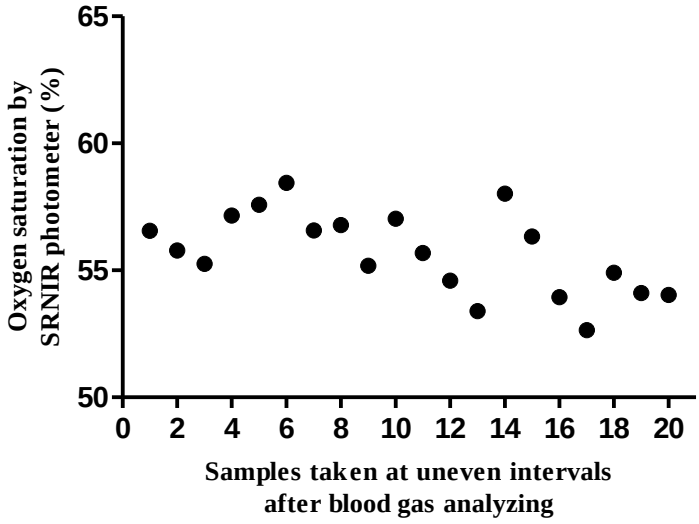

Figure 4.7 The oxygen saturation values measured by the SR-NIR photometer (55.7 ± 1.6%) when the blood oxygen saturation was at 58.0%. The deviations were ranged from -5.3% to 0.4% (n = 20).

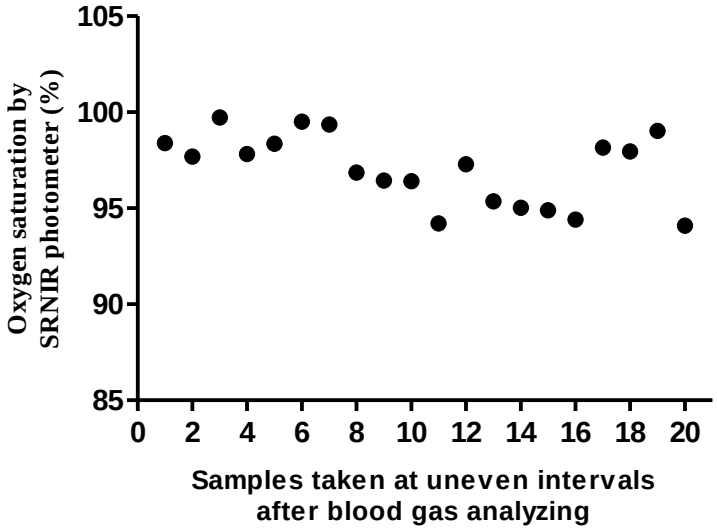

Figure 4.8 The oxygen saturation values measured by the SR-NIR photometer (97.0 ± 1.9%) when the blood oxygen saturation was at 96.7%. The deviations were ranged from -2.6% to 3.1% (n = 20).

4.3. Examination of forearm flexor muscle oxygenation before and after electrical muscle stimulation using SR-NIR photometer

Before passive exercise was conducted, the resting value of tissue oxygen saturation in forearm was determined. The S_tO_2 among subjects were ranged from 51.9% to 104.7% (n = 11) (Table 4.7). After 15 minutes of passive exercise induced by electrical muscle stimulation, the average tissues oxygen saturation decreased significantly (p = 0.001) from 71.4 ± 14.0% to 63.9 ± 9.7% (Figure 4.9). Figure 4.9-4.20 showed the S_tO_2 variations among subjects

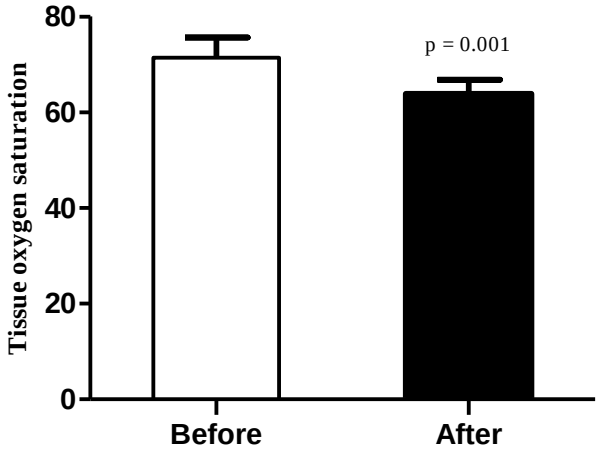

Figure 4.9 Tissue oxygen saturation in forearm before and after electrical stimulation induced muscle contraction (n =11).

Table 4.7

The tissue oxygen saturation of each subject before and after electrical stimulation induced muscle contraction.

Subject no	Before	After
subject 1	70.8 ± 1.0%	59.6 ± 2.0%
subject 2	66.1 ± 1.6%	61.0 ± 1.3%
subject 3	70.6 ± 1.6%	57.8 ± 2.6%
subject 4	63.9 ± 1.4%	60.8 ± 2.0%
subject 5	65.4 ± 1.8%	62.9 ± 1.8%
subject 6	68.6 ± 1.5%	61.5 ± 1.8%
subject 7	66.2 ± 2.2%	61.3 ± 1.4%
subject 8	68.0 ± 1.2%	63.0 ± 1.8%
subject 9	89.2 ± 4.0%	78.5 ± 2.5%
subject 10	104.7 ± 1.3%	85.6 ± 3.5%
subject 11	51.9 ± 2.4%	50.6 ± 1.1%

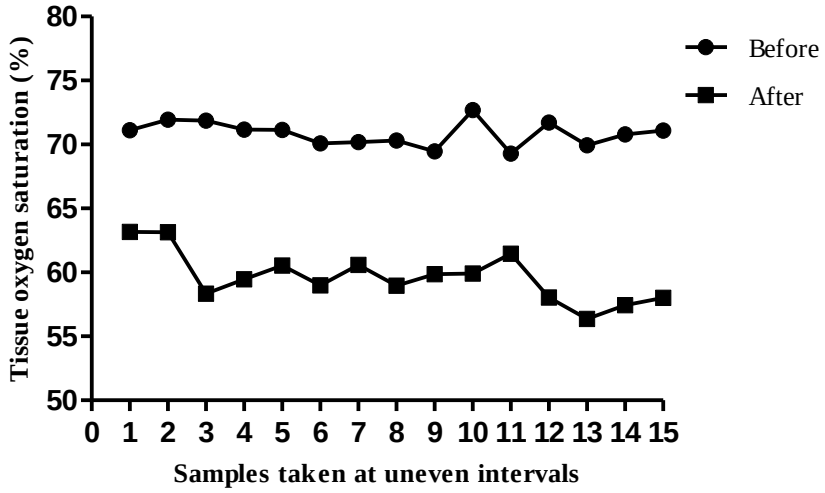

Figure 4.10 The tissue oxygen saturation in forearm of subject 1 before and after electrical stimulation induced muscle contraction. The tissue oxygen saturation reduced from 70.8 ± 1.0% to 59.6 ± 2.0% after electrical stimulation induced muscle contraction (n = 15).

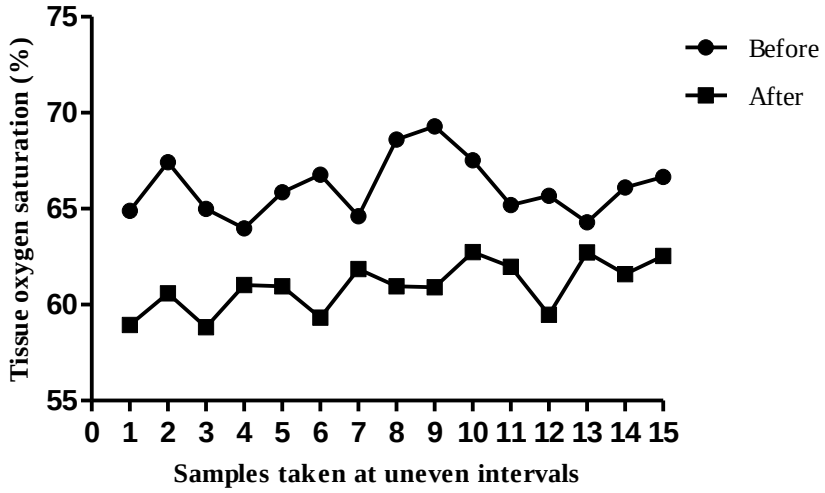

Figure 4.11 The tissue oxygen saturation in forearm of subject 2 before and after electrical stimulation induced muscle contraction. The tissue oxygen saturation reduced from 66.1 ± 1.6% to 61.0 ± 1.3% after electrical stimulation induced muscle contraction (n = 15).

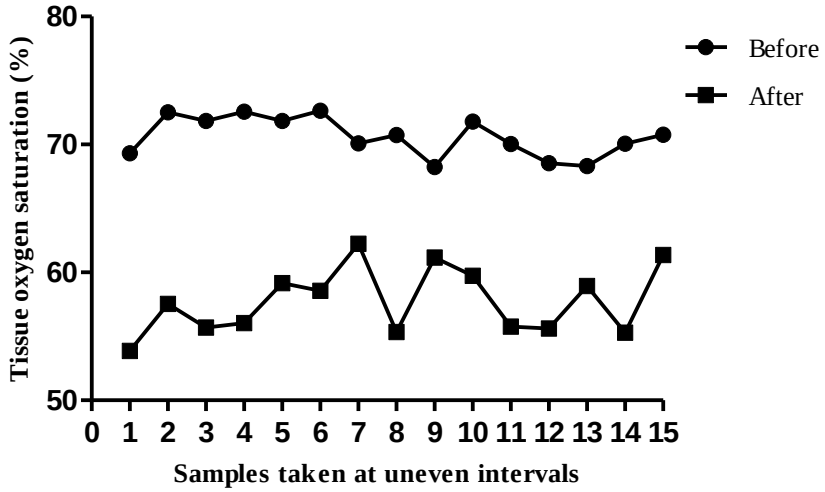

Figure 4.12 The tissue oxygen saturation in forearm of subject 3 before and after electrical stimulation induced muscle contraction. The tissue oxygen saturation reduced from 70.6 ± 1.6% to 57.8 ± 2.6% after electrical stimulation induced muscle contraction (n = 15).

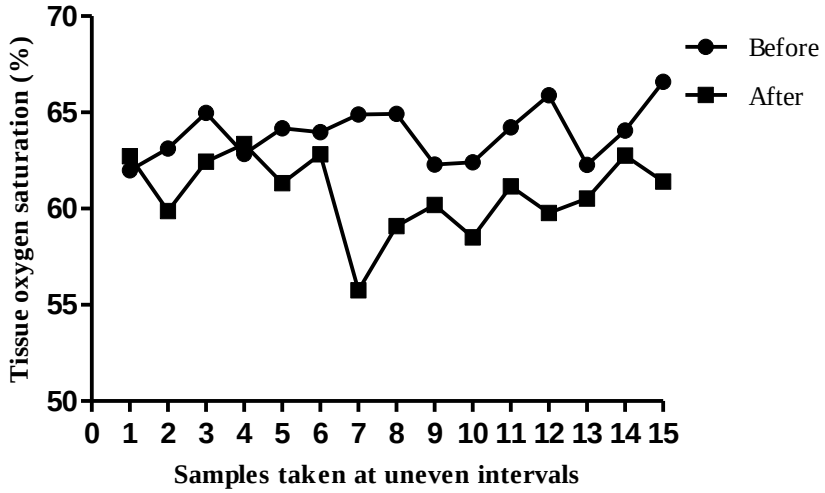

Figure 4.13 The tissue oxygen saturation in forearm of subject 4 before and after electrical stimulation induced muscle contraction. The tissue oxygen saturation reduced from 63.9 ± 1.4% to 60.8 ± 2.0% after electrical stimulation induced muscle contraction (n = 15).

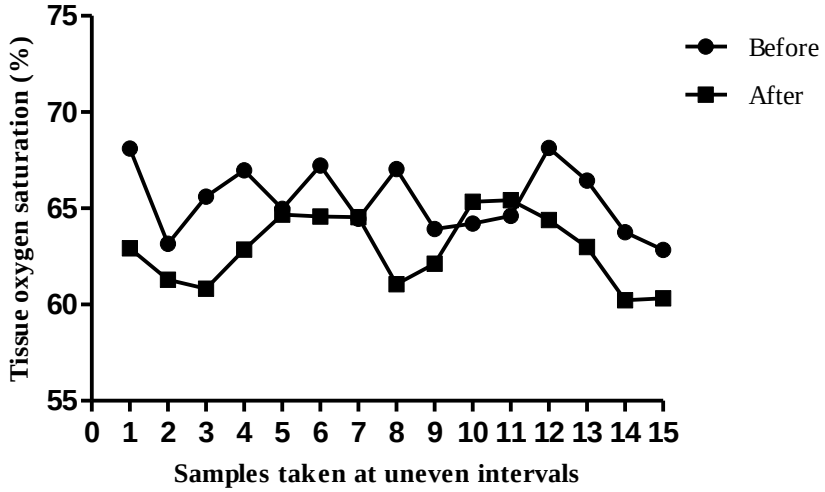

Figure 4.14 The tissue oxygen saturation in forearm of subject 5 before and after electrical stimulation induced muscle contraction. The tissue oxygen saturation reduced from 65.4 ± 1.8% to 62.9 ± 1.8% after electrical stimulation induced muscle contraction (n = 15).

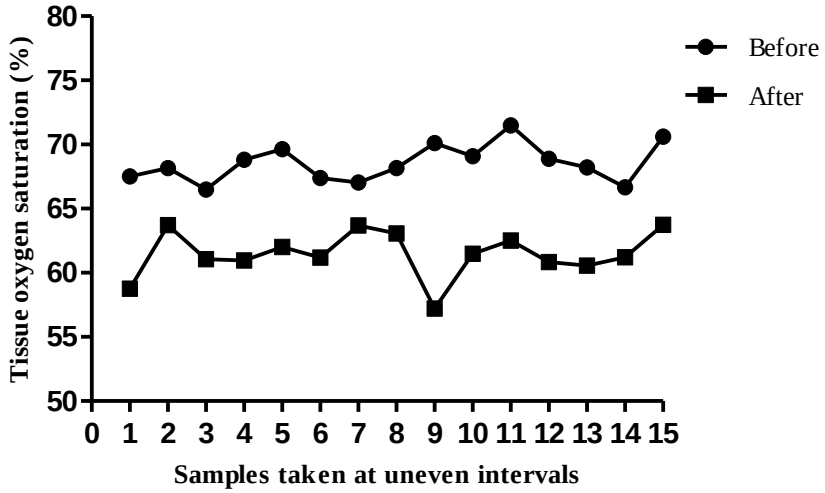

Figure 4.15 The tissue oxygen saturation in forearm of subject 6 before and after electrical stimulation induced muscle contraction. The tissue oxygen saturation reduced from 68.6 ± 1.5% to 61.5 ± 1.8% after electrical stimulation induced muscle contraction (n = 15).

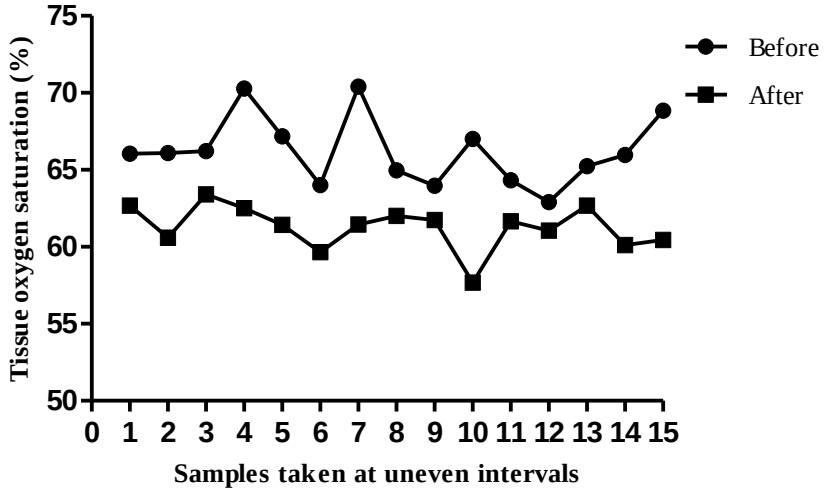

Figure 4.16 The tissue oxygen saturation in forearm of subject 7 before and after electrical stimulation induced muscle contraction. The tissue oxygen saturation reduced from 66.2 ± 2.2% to 61.3 ± 1.4% after electrical stimulation induced muscle contraction (n = 15).

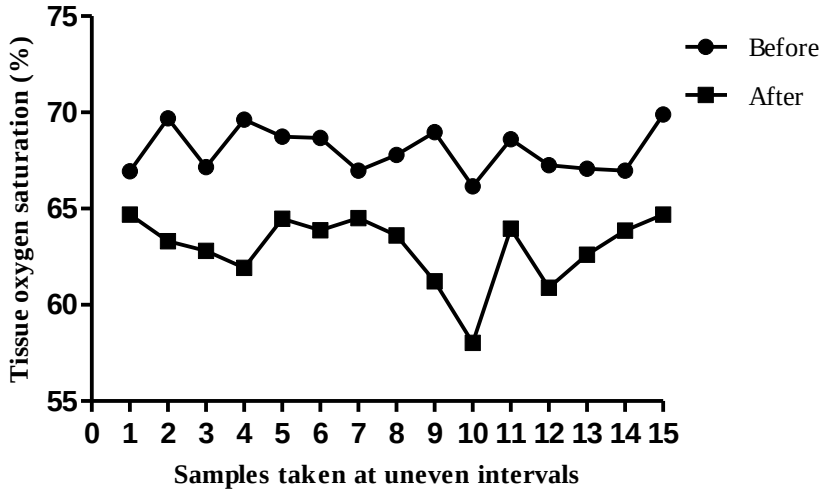

Figure 4.17 The tissue oxygen saturation in forearm of subject 8 before and after electrical stimulation induced muscle contraction. The tissue oxygen saturation reduced from 68.0 ± 1.2% to 63.0 ± 1.8% after electrical stimulation induced muscle contraction (n = 15).

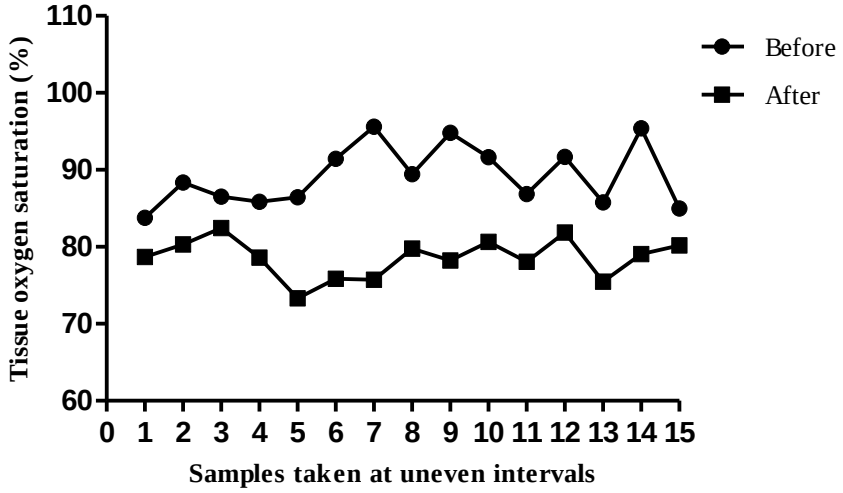

Figure 4.18 The tissue oxygen saturation in forearm of subject 9 before and after electrical stimulation induced muscle contraction. The tissue oxygen saturation reduced from 89.2 ± 4.0% to 78.5 ± 2.5% after electrical stimulation induced muscle contraction (n = 15).

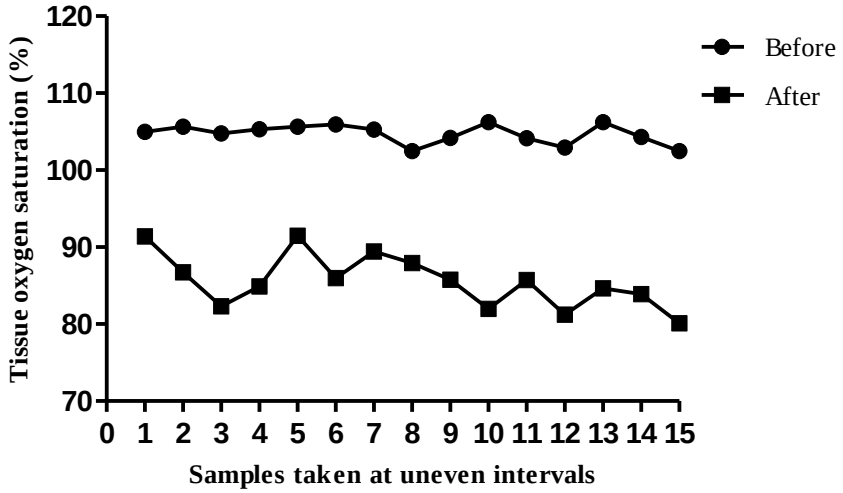

Figure 4.19 The tissue oxygen saturation in forearm of subject 10 before and after electrical stimulation induced muscle contraction. The tissue oxygen saturation reduced from 104.7 ± 1.3% to 85.6 ± 3.5% after electrical stimulation induced muscle contraction (n = 15).

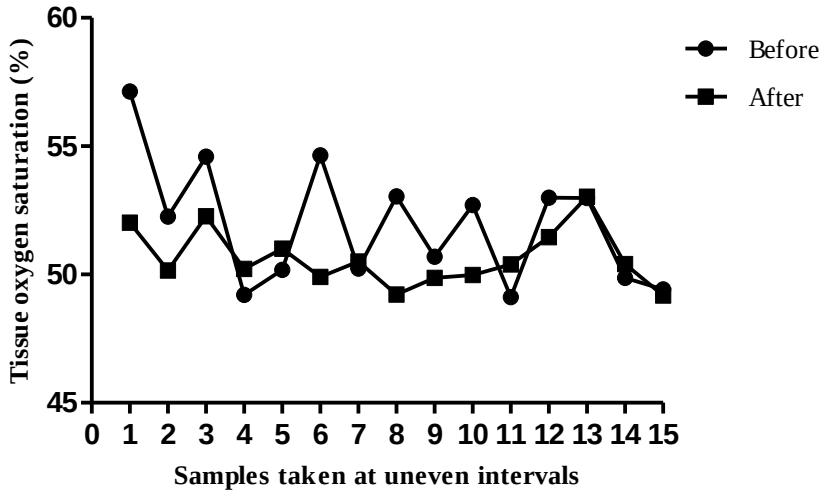

Figure 4.20 The tissue oxygen saturation in forearm of subject 11 before and after electrical stimulation induced muscle contraction. The tissue oxygen saturation reduced from 51.9 ± 2.4% to 50.6 ± 1.1% after electrical stimulation induced muscle contraction (n = 15).

Chapter 5

Discussion

The application of near infrared spectroscopy for tissue oxygenation measurement requires two essential procedures. The first one is to determine the absorption coefficients of tissues. Currently, there are three *in vivo* methods available, namely time resolved (TD), multi-distance frequency domain (FD) and spatially resolved (SR) method. The second procedure involves the evaluation of hemoglobin concentrations and tissues oxygen saturation by absorption coefficients based on Beer Lambert law. Of the three methods for absorption coefficient measurements, the instrumentation required by the spatially resolved (SR) method is relatively simple and can be conducted with less complicated instrumentation. Moreover, the SR method requires wavelength dependence of transport scattering coefficient $\mu_s'(\lambda)$ in the examination region to be consistent among subjects. This means that the value of $\frac{\mu_s'(\lambda_1)}{\mu_s'(\lambda_2)}$ in the examined region at any two wavelengths of near infrared light at λ_1 and λ_2 have to be consistent among different subjects. In this study, we examined the transport scattering coefficient at 690 nm and 830 nm, $\mu_s'(690\ \text{nm})$ and $\mu_s'(830\ \text{nm})$ in greater trochanter region. Our results of $\frac{\mu_s'(690\ \text{nm})}{\mu_s'(830\ \text{nm})}$ among eleven subjects were found to be 1.08 ± 0.09 cm^{-1} on average. The inter-subject variation, defined by the percentage of standard deviation from the mean value, was 8.3% in the greater trochanter region. This value was lower than the forearm (28% in five subjects), the scalp (13% in seven subjects) and the calf muscle (21% in

twenty one subjects) as reported by Matcher (47). Our result also indicated the consistent wavelength dependence of $\mu_s'(\lambda)$ in greater trochanter region. In equation [18], the algorithm of S_tO_2 depends on the ratio of absorption coefficients at any two wavelengths, $\frac{\mu_a(\lambda_1)}{\mu_a(\lambda_2)}$.

Using equation [62], $\frac{\mu_a(\lambda_1)}{\mu_a(\lambda_2)}$ is inversely proportion to the ratio of the $\frac{\mu_s'(\lambda_1)}{\mu_s'(\lambda_2)}$ (equation [77]).

$$\frac{\boldsymbol{\mu_a(\lambda_1)}}{\boldsymbol{\mu_a(\lambda_2)}} = \frac{\boldsymbol{\mu_s'(\lambda_2)}}{\boldsymbol{\mu_s'(\lambda_1)}} \frac{\left(\frac{\partial A(\rho,\lambda_1)}{\partial \rho} - \frac{2}{\rho}\right)^2}{\left(\frac{\partial A(\rho,\lambda_2)}{\partial \rho} - \frac{2}{\rho}\right)^2} \qquad [77]$$

When $\frac{\mu_s'(\lambda_2)}{\mu_s'(\lambda_1)}$ is a constant value with minimal variations (i.e. 1.08 ± 0.09 cm^{-1} in this case), then $\frac{\mu_a(\lambda_1)}{\mu_a(\lambda_2)}$ depends purely on the absorbance difference between the two source-detector distances at two wavelengths $\left(\frac{\partial A(\rho,\lambda_1)}{\partial \rho}$ and $\frac{\partial A(\rho,\lambda_2)}{\partial \rho}\right)$. In our result, consistent wavelength dependence of $\mu_s'(\lambda)$ is established (inter-subject variation of $\frac{\mu_s'(\lambda_2)}{\mu_s'(\lambda_1)}$ was found to be 8.3%). This indicated that SR method can be used to determine S_tO_2 at the greater trochanter region. Similarly, consistent wavelength dependence of $\mu_s'(\lambda)$ was also examined in the forearm region. Among the nine healthy subjects, the ratio $\frac{\mu_s'(690\ nm)}{\mu_s'(830\ nm)}$ was found to be 1.5 ± 0.12 cm^{-1}. Inter-subject

variation was found to be 8% which was much lower than the finding of Matchers (28% in five subjects)(47). The discrepancy could be due to the difference of subjects' gender between the two studies. Matchers separately determined the inter-subject variation in calf muscle on five male and six female subjects. The female subjects encountered 25% inter-subject variation which was 3.1-fold of male subjects (8%). The underlying reason of such difference in gender requires further investigation.

In present study, we have also investigated the applicability of using spatially resolved (SR) method to determine oxyhemoglobin ([Hb]) and deoxyhemoglobin concentrations ([HbO_2]) in the greater trochanter region. From equations [15] and [16], [Hb] and [HbO_2] were dependent on the measured absorption coefficients at two wavelengths $(\mu_a(\lambda_1)$ and $\mu_a(\lambda_2))$, which are inversely proportional to $\mu_s'(\lambda_1)$ and $\mu_s'(\lambda_2)$ respectively. Therefore, constant values of $\mu_s'(\lambda_1)$ and $\mu_s'(\lambda_2)$ among subjects are required for the determination of [Hb] and [HbO_2]. In this work, the $\mu_s'(690\ \text{nm})$ and $\mu_s'(830\ \text{nm})$ among eleven subjects were found to be 7 ± 1.7 cm^{-1} and 6.5 ± 1.5 cm^{-1}on average. The standard deviations were 23.6% and 24.6% of their mean respectively. Such large inter-subject variations of $\mu_s'(690\ \text{nm})$ and $\mu_s'(830\ \text{nm})$ in greater trochanter region indicated that the SR method could not be used to quantify the [Hb] and [HbO_2] in greater trochanter region. In general, our result suggested that SR method could only be applied to determine S_tO_2, but cannot be used to determine [Hb] and [HbO_2] in the greater trochanter region.

We also examined the variations of tissue optical parameters ($\mu_a(690\,\text{nm})$, $\mu_a(830\,\text{nm})$, $\mu_s'(690\,\text{nm})$, $\mu_s'(830\,\text{nm})$), hemoglobin concentration ([Hb], [HbO_2]), total hemoglobin concentration ([tHb]) and tissue oxygen saturation (S_tO_2) between the left and right side of the forearms and the greater trochanters. In general, there should be little variations between the two sides of the limbs. From our results, there is no statistical significant difference found among these parameters between the left and right side except at the greater trochanter region, where the hemoglobin concentrations (i.e. [Hb], [HbO_2] and [tHb]) were higher on the right side as compared to the left. Further, the difference of [HbO_2] between right and left greater trochanter was shown statistically significant (p=0.047). The underlying reason of such finding was unclear.

During examination, the left and right trochanters were alternately measured for three trials. Since the measurements were done in side-lying position, the tissues overlying the greater trochanter of the lower side were compressed. Compressive loading could occlude the capillaries in tissues and eventually lowered down the tissue oxygenation. After the removal of compressive loading, the blood flow restored and reactive hyperemia could occur to speed up the recovery of tissue oxygenation. The recovery time for healthy subjects was typically 1 to 2 minutes after 10 to 15 minutes of compressive loading in sacrum region (31). Mayrovitz (147) reported that hyperemia response at the heel after 140 mmHg of compression for 10 minutes can return to baseline after 5.71 minutes. At the greater trochanter

region, it has also demonstrated that after 3 minutes of external compression at 172 mmHg, blood flow of healthy subjects will be restored to baseline level after 5.15 minutes (148). Based on the result of above studies, 5 minutes of supine resting in between measurements can ensure the recovery of oxygenation for tissues overlying the greater trochanter after each experiment period. For assessment of patients who are at risk of pressure ulcers, longer resting time between measurements should be allowed. Bader (31) showed that debilitated subjects could not restore their blood flow and transcutaneous oxygen tension to the baseline level at the sacrum region within 5 minutes after the compressive loading was removed, whereas healthy subjects can regain their baseline condition within 1 to 2 minutes. Similar finding was also reported by Tam (148). Paraplegic subjects required on average 1 minute longer to restore their resting blood flow during hyperemia when compared with healthy subjects. Therefore, for subjects at risk of pressure ulcer, precautions should be made to allow sufficient resting time for tissue recovery in between assessments. It should also be noted that the measurement technique used in the above studies can only reflect the condition in skin level, the situation at deeper tissue was not revealed.

To ensure that the measurements from the spectrophotometer (Imagent, ISS, USA) that we used in this part of the study are comparable to those reported in literatures, we first evaluated the resting [tHb], [HbO_2] and S_tO_2 in the forearm and compared with results reported in literatures. From our results, the values of [tHb], [HbO_2]

and S_tO_2 in forearm region were found to be 94.5 ± 9.7 μM, 61.5 ± 7.0 μM and 65.0 ± 3.5% respectively. The average [tHb] and [HbO_2] in our results were slightly less than those reported in Hamaoka's study (113 ± 9 μM and 69 ± 13 μM) while the average S_tO_2 in our study was comparatively higher (61.1 ± 4.4%.) (149). When compared with S_tO_2 values at similar site, our result was within 2% variations to those findings reported in literatures (Table 5.1). Therefore, we believed that the spectrophotometer (Imagent, ISS, USA) was suitable for use to determine the optical properties of tissues at the greater trochanter region.

The concentration of hemoglobin molecules is generally constant in the bloodstream in different parts of body. Therefore, [tHb] can reflect the blood volume and the vascular network density at a localized anatomical site. Similarly, the amount of [HbO_2] in tissues can manifest the local oxygen storage condition. In our measurement, the [tHb] and [HbO_2] in the forearm were found to be 2.6-fold and 3.5-fold higher than those found at the greater trochanter region. These indicated that the localized blood volume and oxygen storage in the greater trochanter region were much lower than those in the forearm. These observations can be explained by the fact that forearm muscles are composed of a denser vascular network and higher oxygen storage are required to sustain the oxygen supply to meet the demand of wrist flexion (150). The availability of oxygen supply and oxygen storage could be key factors affecting the time-to-ischemia in tissues under compressive loading.

Table 5.1

Comparison of tissue oxygen saturation measurement on different target muscles in forearm of health subjects in our study and other studies.

Method	Target muscles	Mean S_tO_2 ± std	No of subjects	Reference
SR[a]	Flexor digitorum	71.4 ± 14.0%	11	Our study
FD[a]	Flexor digitorum	65.0 ± 3.5%	9	
SR[a]	Flexor digitorum	66.1 ± 4.0%	24	(37)
FD[a]	Brachioradialis	63.9 ± 4.9%	15	(41)
SR[a]	Brachioradialis	67.0 ± 5.0%	10	(42)
SR[a]	Brachioradialis	68.7 ± 5.2%	18	(151)
SR[a]	flexor digitorum	65.6 ± 5.6%	18	
SR[b]	Brachioradialis	72.1 ± 8.1%	17	
SR[b]	flexor digitorum	69.6 ± 8.5%	16	

std = standard deviation,

SR = spatially resolved near infrared spectroscopy,

FD = multi-distance frequency domain near infrared spectroscopy,

The superscript of a and b mean that the measurement was done by 2 wavelengths and 3 wavelengths near infrared light sources.

The tissues overlying bony prominence were known to be less tolerable to damage under externally compression. In present study, the soft tissue thickness (including skin, fat and muscles) overlying the greater trochanter was found to be 1.51 ± 0.4 cm. Therefore, by equation [63], a sensor probe with source-detector distance of approximately 32.5 mm was needed in order to examine the oxygenation at the

required sampling depth. However, the source-detector distance should be adjustable according to the thickness of the tissues at the measurement site. For example, under seating conditions, the soft tissues thickness overlying the ischial tuberosities was found to be 33.5 mm on average in healthy subjects while it was only 23.5 mm in spinal cord injuries patients (152). The thicknesses of tissue overlying the ischial tuberosities and sacrum in healthy subjects during side-lying with hip and knee flexed at 90° were found to be 43.8 mm and 13.8 mm from the skin (153)

Our NIR photometer was constructed based on the spatially resolved (SR) method. To satisfy the Beer Lambert's law, light passing through the absorbing mediums needs to be monochromic and coherent (43). Therefore, lasers were used in our SR-NIR photometer. To penetrate into the deep tissues, high intensity of light is required. However, continue illumination of tissues by strong intensity of light will lead to large energy absorption and could heat up the tissues. Therefore, laser light was pulsed at peak intensity instead (154). Owing to the availability of laser sources, the laser sources of our system were pulsed at 70 ns with half maximum intensity. To acquire the reflected light from the pulsed laser, a very high frequency A/D converter (>60 MHz) is needed. Such equipment was not available. Alternatively, we used an oscilloscope to capture the waveform of the reflected light intensity. The disadvantage of this approach was that our oscilloscope could only manually record the signal in a window of time. As a result, our measurement

cannot be conducted in real time.

In this study, a blood-Intralipid based tissue phantom was designed to evaluate the performance of our SR-NIR photometer. Ideally, the phantom should simulate all tissue optical properties of human tissues including absorption and scattering properties, refractive index and the wavelength dependence of these properties. Moreover, these properties should also be stable over time (140). Unfortunately, there was no such an ideal tissue phantom available. Similar to other tissue phantoms (138-141, 144), our phantom consists of two materials which simulate the required absorption and scattering properties. These materials were called absorber and scatter. There are several absorbers that are suitable for adding into aqueous tissue phantoms to simulate the absorption properties of biological tissues. These included whole blood, Indian ink, molecular dyes, fluorophores and heterogeneities (140). For simply mimicking the absorption properties of tissues, Indian ink and molecular dyes were commonly used (155). In the present study, the main purpose of our tissue phantom was to simulate different tissue oxygenation conditions. Therefore, hemoglobin must be presented in the phantom. Hemoglobin is the main absorber of near infrared light in biological tissues. However, pure hemoglobin molecules without the protection from cell membrane of red blood cells were not stable. The free iron in the heme-group of the hemoglobin molecules could be oxidized by air and lost its oxygen-binding ability (156). In view of that, whole blood has to be used in our phantom.

In literatures, there were three types of materials that can be used as scatters. These included: lipid microparticles, polymer microparticles and white metal oxide powder (140). Examples of lipid micoparticles are milk and Intralipid-10%. Common polymer includes polymer microspheres and quartz glass microspheres. White metal oxide is usually used to constructed solid phantom. Examples included Titanium oxide (TiO_2) and Aluminum oxide (Al_2O_3) powder. Of all these scatters, polymer microspheres and Intralipid-10% were widely used (137, 138, 140, 144, 145). In our tissue phantom, Intralipid-10% was selected due to its low cost and availability. Although scatters absorb near infrared light; under same concentration, the magnitude of absorption by the scatters is much smaller than the absorbers within the environment. Besides, the volume fraction of the scatters used in most tissue phantoms is comparatively low (1% to 5%). The absorption effect of these scatters can thus be neglected.

In contrast to the aqueous type tissue phantom, several studies have reported the use of solid tissue phantom (139, 141, 157). It was known that absorption and scattering properties were different among skin, subcutaneous tissues and muscles (40). The solid tissue phantom allows the feasibility of simulating different absorption and scattering properties in multi-layers, which mimic the *in vivo* conditions. However, our tissue phantom must be in aqueous form for red blood cells to survive. As soon as the red blood cell dies, hemoglobin within the cell will loss the protection of cell membrane and formed other by-products. Besides, gas perfusion cannot be

performed in solid tissue phantom and the deoxygenation process by yeast was also not feasible. Therefore, solid phantoms were unable to simulate different oxygenation levels.

There were several limitations in the experimental setup for validating our photometer. First, pure nitrogen gas was used to replace oxygen from the environment to allow natural decay of blood oxygenation. The disadvantage was that the decay rate of the oxygen saturation within the phantom cannot be controlled. It took approximately 30 minutes to reduce oxygen saturation by 5%. Some other reported studies used yeast to consume the oxygen in their tissue phantom (137, 151). However, it is not clear how yeast will affect the absorption and scattering of near infrared light. Second, the hemoglobin concentration that can be used in our blood-Intralipid tissue phantom was limited by the specification of the blood gas analyzer used in this work. This analyzer required that blood sample should have at least 15% of hematocrit. In normal human blood, the hematocrit is about 40%, so the blood concentration in the blood-Intralipid tissue phantom was diluted 50% using plasma. Human whole blood contains 8.56 to 11.3 mM of hemoglobin. After dilution by plasma, the hemoglobin concentration in the blood-Intralipid tissue phantom was reduced (ranging from 4.28 to 5.65 mM). However, this concentration was still much higher (i.e. 50 times and 135 times) than the values in forearm (94.5 ± 9.7 μM) and greater trochanter (36.4 ± 13.2 μM). This leaded to higher light absorption in our tissue phantom when compared with

biological tissues. In such high absorption condition, the power of laser diodes and the sensitivity of the photodetectors were insufficient to penetrate 1.5 cm depth during measurements on our tissue phantom. Because of this limitation, the maximum source-detector distance of the sensor probe was limited to 13 mm. Moreover, due to the physical dimension of the photodetectors (diameter = 6.3 mm), they can only be positioned at 6.5 and 13 mm from the laser source. Under such limitations, the average source-detector distance could only be limited to 9.5 mm with an estimated sampling depth of 3.4 mm (equation [63]). Fortunately, the absorption of hemoglobin concentration in our phantom was still much less than the NIR light attenuation caused by scattering. Estimated using the equation of van Staveren (143), transport scattering coefficients of Intralipid at 765 nm ($\mu_s(765\text{ nm}) = 18.3\text{ cm}^{-1}$) and 856 nm ($\mu_s(856\text{nm}) = 13.9\text{ cm}^{-1}$) in this concentration (60 ml/L) were much higher than 135-fold of absorption coefficient in greater trochanter region ($\mu_a \sim 2.7\text{ cm}^{-1}$). Thus, the scattering event within the phantom was dominant the light attenuation over the absorption which is a necessary assumption in the algorithm of SR-NIR spectroscopy.

Thirdly, the blood-Intralipid tissue phantom was not reusable. The life span of this aqueous phantom was less than one day (139-141). In our validation, as whole blood sample from one single donor was required, we only conducted the experiment for one time. During the measurement involving 82% oxygenation, eleven out of the twenty data sets were obtained (Figure 4.3). This was due to

human mistake in recording data from the oscilloscope. Despite of above limitations, high correlation (r^2 = 0.9718) was found between oxygen saturation measured by the NIR photometer using spatially resolved method and the commercial blood gas analyzer. Table 4.6 showed that there were good agreements between the measurement of the SR-NIR photometer and the commercial blood gas analyzer. The accuracy of the SR-NIR photometer was acceptable since the maximum variation of the measurement was within 7.5% of the results from blood gas analyzer.

After the *in vitro* validation in tissue phantom, we demonstrated the *in vivo* tissue oxygen saturation changes in forearm by passively exercising the forearm muscle through continuously electrical muscle stimulation. A number of literatures have shown that the muscle oxygen consumption increased with the level and duration of exercises. Compared with active exercise, passive exercise caused less change in superficial blood flow and thus had faster consumption of muscle oxygenation. This could reduce the exercise time for lower down the tissue oxygen level and increase the recovery time after the exercise (158). Table 5.1 showed the comparison of measurements on different targeted muscles in the forearm of health subjects among this work and other studies (37, 41, 42, 151). The mean resting S_tO_2 values of forearm muscles in other studies were ranged from 63.9% to 72.1%. The mean value of S_tO_2 in our measurement was similar to those measurements in other studies (37, 151). The average S_tO_2 in our SR-NIR photometer (71.4 ±

14.0%) was slightly larger than those reported in other studies with the same targeted muscles (ranged from 65.6% to 69.6%). A number of studies have showed that muscle oxygen saturation was reduced after active or passive exercises through the use of electrical stimulation (158-160). However, their conclusion was based on relative decrease in oxyhemoglobin concentration and increase in deoxyhemoglobin. The absolute change of the oxygen saturation has not been determined. In terms of the actual tissue oxygenation changes after exercise, Hamaoka (149) demonstrated that S_tO_2 was reduced after 2 minutes of handgrip contraction exercise using a time resolved NIR spectroscopy. The targeted forearm muscle was not mentioned. For 10%, 15% and 20% of maximum voluntary contraction, the S_tO_2 among five healthy subjects were reduced from 61 ± 4.4% to 31.6 ± 3.8%, 20.2 ± 1.2% and 22.5 ± 2.3% respectively. In our result, the average S_tO_2 was reduced from 71.4 ± 14% to 63.9 ± 9.7%. The reduction was only one-third of the Hamaoka study. This may due to the difference in exercise protocol. In Hamaoka study, subjects were required to perform sustained contraction which likely caused muscle to fatigue.

5.1. Suggestion for Future Research

In this study, we confirmed the applicability of using spatially resolved method to determine the tissue oxygen saturation (S_tO_2) in greater trochanter region. There are other common sites of pressure ulcer such as ischial tuberosites, sacrum and heel. Before we can apply the spatially resolved NIR spectroscopy to examine S_tO_2

in these regions, the consistency of the wavelength dependence of transport scattering coefficient $\left(\mu_s'(\lambda)\right)$ needs to be validated. The related parameter $\frac{\mu_s'(\lambda_1)}{\mu_s'(\lambda_2)}$ at any two wavelengths $(\lambda_1 \text{ and } \lambda_2)$ of NIR light can be examined using NIR spectroscopy in multi-distance frequency domain method or time resolved method in future studies.

The original application of this work is to develop a home care instrument to monitor tissue oxygenation changes at anatomical sits that are prone to pressure ulcer, so that preventive intervention can be applied at an early stage of tissue distress. At present, the penetration depth of the instrument is only 3.4 mm. Future work is required to increase the penetration power of the photometer, so that it can be used to assess deeper tissues.

Chapter 6

Conclusions

A new NIR photometer has been developed using the spatially resolved method. To validate the performance of this new photometer, an aqueous form tissue phantom using blood-Intralipid was constructed. High correlation (r^2 = 0.9718) was found between the oxygen saturation values measured by the new SR-NIR photometer and from blood gas analyzer. With the use of electrical muscle stimulation, we demonstrated that the new photometer was capable of detecting tissue oxygenation changes in subcutaneous tissue at a depth of 3.4 mm. In view of the difference in tissue optical properties, hemoglobin concentrations and oxygen saturations at different anatomical sites, we also examined these values at the greater trochanter region, which is an area prone to pressure ulcer. Our measures confirmed that the spatially resolved method is suitable for assessing tissue viability at the greater trochanter region.

References

1. Mak AF, Zhang M, Tam EW. Biomechanics of pressure ulcer in body tissues interacting with external forces during locomotion. Annual Review of Biomedical Engineering. 2010;12:29-53.

2. Bouten C, Oomens C, Baaijens F, Bader D. The etiology of pressure ulcers: skin deep or muscle bound? Archives of Physical Medicine and Rehabilitation. 2003;84:616-9.

3. Bader DL, Bouten CVC, Colin D, Oomens CWJ. Pressure ulcer research: current and future perspectives Berlin ; New York; 2005.

4. Evans J, Stephen-Haynes J. Identification of superficial pressure ulcers. Journal of Wound Care. 2007;16(2):54-6.

5. Defloor. T., Schoonhoven. L., Fletcher. J., Furtado. K., Heyman. H., Lubbers. M., et al. Pressure ulcer classification: differentiation between pressure ulcers and moisture lesions. EPUAU Review. 2005;6(3):81-5.

6. Ankrom MA, Bennett RG, Sprigle S, Langemo D, Black JM, Berlowitz DR, et al. Pressure-related deep tissue injury under intact skin and the current pressure ulcer staging systems. Advances in Skin & Wound Care. 2005;18:35-42.

7. Baumgarten M, Margolis DJ, Localio AR, Kagan SH, Lowe RA, Kinosian B, et al. Pressure ulcers among elderly patients early in the hospital stay. Journals of Gerontology - Series A Biological Sciences and Medical Sciences. 2006;61(7):749-54.

8. Russo A, Steiner C, Spector W. Hospitalizations Related to Pressure Ulcers among Adults 18 Years and Older, 2006. United States Agency for Healthcare Research and Quality. 2008.

9. National Pressure Ulcer Advisory Panel. Pressure ulcers incidence, economics, risk assessment: Consensus Development Conference Statement. Decubitus. 1989;2(2):24-8.

10. Graves N, Birrell F, W. M. Effect of Pressure Ulcers on Length of Hospital Stay. Infection Control and Hospital Epidemiology. 2005;26(3):293-7.

11. Kosiak M, Kubicek WG, Olson M, Danz JN, Kottke FJ. Evaluation of pressure as a factor in the production of ischial ulcers. Archives of Physical Medicine and Rehabilitation. 1958;39(10):623-9.

12. Koo TKK, Mak AFT, Lee YL. Posture effect on seating interface biomechanics: Comparison between two seating cushions. Archives of Physical Medicine and Rehabilitation. 1996;77(1):40-7.

13. Bader DL, Hawken MB. Pressure distribution under the ischium of normal subjects. Journal of Biomedical Engineering. 1986;8(4):353-7.

14. Daniel RK, Priest DL, Wheatley DC. Etiologic factors in pressure sores: An experimental model. Archives of Physical Medicine and Rehabilitation. 1981;62(10):492-8.

15. Swain ID, Bader DL. The measurement of interface pressure and its role in soft tissue breakdown. Journal of Tissue Viability. 2002;4:132-46.

16. Jonsson A, Lindén M, Lindgren M, Malmqvist L, Bäcklund Y. Evaluation of antidecubitus mattresses. Medical and Biological Engineering and Computing. 2005;43(5):541-7.

17. Kett RL, Levine SP. A dynamic model of tissue deflection in a seated individual. Proceedings of the 10th Annual RESNA; Washington DC1987. p. 524-6.

18. Liu MH, Grimm DR. Transcutaneous oxygen tension in subjects with tetraplegia with and without pressure ulcers: A Preliminary Report. Journal of Rehabilitation Research & Development. 1999;36(3):202-6.

19. Li ZY, Tam WC, Mak FT, Lau CY. Effects of prolonged compression on the variations of haemoglobin oxygenation—assessment by spectral analysis of reflectance spectrophotometry signals. Physics in Medicine and Biology. 2006;51(21):5707-18.

20. Bader DL, White SH. The viability of soft tissues in elderly subjects undergoing hip surgery. Age and Ageing. 1998;27(2):217-21.

21. Gute DC, Ishida T, Yarimizu K, Korthius RJ. Inflammatory responses to ischemia, and reperfusion in skeletal muscle. Molecular and Cellular Biochemistry. 1998;179(1):169-87.

22. Bennett L, Lee BY. Vertical shear existence in animal pressure threshold experiments. Decubitus. 1988;1(1):18-24.

23. Goossens RHM, Zegers R, van Dijke GAH, Snijders CJ. Influence of shear on skin oxygen tension. Clinical Physiology. 1994;14(1):111-8.

24. Ohura T, Takahashi M, Ohura JN. Influence of external forces (pressure and shear force) on superficial layer and subcutis of porcine skin and effects of dressing materials: Are dressing materials beneficial for reducing pressure and shear force in tissues? Wound Repair & Regeneration. 2008;16(1):102-7.

25. Zhang M, Roberts VC. The effect of shear forces externally applied to skin surface on underlying tissues. Journal of Biomedical Engineering. 1993;15(6):451-6.

26. Bergstrom N, Braden BJ. A prospective study of pressure sore risk among institutionalized elderly. Journal of the American Geriatric Society. 1992;40(8):747-58.

27. Lindgren M, Unosson M, Fredrikson M, Ek AC. Immobility - A major risk factor for development of pressure ulcers among adult hospitalized patients: A prospective study. Scandinavian Journal of Caring Sciences. 2004;18(1):57-64.

28. Christensson L. Malnutrition in elderly people newly admitted to a community resident home. Journal of Nutrition, Health and Aging. 1999;3(3):133-9.

29. Van Marum RJ, Meijer JH, Ooms ME, Kostense PJ, Van Eijk JT, Ribbe MW. Relationship between internal risk factors for development of decubitus ulcers and the blood flow response following pressure load. Angiology. 2001;52(6):409-16.

30. Stekelenburg A, Gawlitta D, Bader DL, Oomens CW. Deep tissue injury: How deep is our understanding? Archives of Physical Medicine and Rehabilitation. 2008;89(7):1410-3.

31. Bader D. The recovery characteristics of soft tissue following repeated loading. Journal of Rehabilitation Research and Development. 1990;27(2):141-50.

32. Reenalda J. Dynamic sitting to prevent pressure ulcers in spinal cord injuried [PhD thesis]. Enschede, The Netherlands: University of Twente 2009.

33. Colin D, Loyant R, Abraham P, Saumet J-L. Changes in Sacral Transcutaneous Oxygen Tension in the Evaluation of Different Mattresses in the Prevention of Pressure Ulcers. Advances in Wound Care. 1996;9(1):25-8.

34. Mathieu D, Mani R. A Review of the Clinical Significance of Tissue Hypoxia Measurements in Lower Extremity Wound Management. The International Journal of Lower Extremity Wounds. 2007;6(4):273-83.

35. Mehagnoul-Schipper DJ, Van Der Kallen BFW, Colier WNJM, Van Der Sluijs MC, Van Erning LJTO, Thijssen HOM, et al. Simultaneous measurements of cerebral oxygenation changes during brain activation by near-infrared spectroscopy and functional magnetic resonance imaging in healthy young and elderly subjects. Human Brain Mapping. 2002;16(1):14-23.

36. Kurihara. K, Kikukawa. A, Kobayashi. A. Cerebral oxygenation monitor during head-up and -down tilt using near-infrared spatially resolved spectroscopy. Clinical Physiology and Functional Imaging. 2003;23(4):177-81.

37. Yang Y, Soyemi O, Scott PJ, Landry MR, Lee SM, Stroud L, et al. Quantitative measurement of muscle oxygen saturation without influence from skin and fat using continuous-wave near infrared spectroscopy. Optics Express. 2007;15(21):13715-30.

38. Hoffman JR, Im J, Rundell KW, Kang J, Nioka S, Speiring BA, et al. Effect of muscle oxygenation during resistance exercise on anabolic hormone response. Medicine and Science in Sports and Exercise. 2003;35(11):1929-34.

39. Chance B, Nioka S, Kent J, McCully K, Fountain M, Greenfeld R, et al. Time-resolved spectroscopy of hemoglobin and myoglobin in resting and ischemic muscle. Analytical Biochemistry. 1988;174(2):698-707.

40. Niwayama M, Lin L, Shao J, Shiga T, Kudo N, Yamamoto K. Quantitative measurement of muscle oxygenation by NIRS: analysis of the influences of a subcutaneous fat layer and skin. Proceedings of SPIE. 1999;3597:291-9.

41. DeBlasi RA, Stefano P, Daniela A, Marco M, Rocco R, Saul C, et al. Microvascular dysfunction and skeletal muscle oxygenation assessed by phase-modulation near-infrared spectroscopy in patients with septic shock. Intensive Care Medicine. 2005;31(12):1661-8.

42. Girardis M, Rinaldi L, Busani S, Flore I, Mauro S, Pasetto A. Muscle perfusion and oxygen consumption by near-infrared spectroscopy in septic-shock and non-septic-shock patients. Intensive Care Medicine. 2003;29(7):1173-6.

43. Rolfe P. In vivo near-infrared spectroscopy. Annual review of biomedical engineering. 2000;2:715-54.

44. Patterson MS, Chance B, Wilson BC. Time resolved reflectance and transmittance for the non-invasive measurement of tissue optical properties. Applied Optics. 1989;28(12):2331-6.

45. Fantini S, Franceschini M, Maier J, Walker S, Barbieri B, Gratton E. Frequency-domain multichannel optical detector for noninvasive tissue spectroscopy and oximetry. Optical Engineering. 1995;34(1):32-42.

46. Matcher SJ, Kirkpatrick PJ, Nahid K, Cope M, Delpy DT. Absolute quantification methods in tissue near-infrared spectroscopy. Proceedings of SPIE; San Jose, CA, USA1995. p. 486-95.

47. Matcher SJ, Cope M, Delpy DT. In vivo measurements of the wavelength dependence of tissue-scattering coefficients between 760 and 900 nm measured with time-resolved spectroscopy. Applied Optics. 1997;36(1):386-96.

48. Gefen A. Risk factors for a pressure-related deep tissue injury: a theoretical model. Medical & Biological Engineering & Computing. 2007;45:563-73.

49. Gawlitta D, Oomens CWJ, Bader DL, Baaijens FPT, Bouten CVC. Temporal differences in the influence of ischemic factors and deformation on the metabolism of engineered skeletal muscle. Journal of Applied Physiology. 2007;103(2):464-73.

50. Husain T. An experimental study of some pressure effects on tissues, with reference to the bed-sore problem. The Journal of Pathology and Bacteriology. 1953;66(2):347-58.

51. Stockton L, Rithalia S. Pressure-reducing cushions: Perceptions of comfort from the wheelchair users' perspective using interface pressure, temperature and humidity measurements. Journal of tissue viability. 2009;18(2):28-35.

52. Salcido R, Donofrio J, Fisher S, LeGrand E, Dickey K, Carney J, et al. Histopathology of pressure ulcers as a result of sequential computer-controlled pressure sessions in a fuzzy rat model. Advances in Wound Care. 1994;7(5):23-4.

53. Kosiak M. Etiology and pathology of ischemic ulcers. Archives of Physical Medicine and Rehabilitation. 1959;40(2):62-9.

54. Dinsdale SM. Decubitus ulcers in swine: light and electron microscopy study of pathogenesis. Archives of Physical Medicine and Rehabilitation. 1973;54(2):51-6.

55. Dinsdale SM. Decubitus ulcers: role of pressure and friction in causation. Archives of Physical Medicine and Rehabilitation. 1974;55(4):147-52.

56. Reswick J, Rogers JE. Experience at Rancho Los Amigos Hospital with devices and techniques to prevent pressure ulcers. In: Kenedi R, Cowden J, Scales J, editors. Bedsore Biomechanics. London: University Park Press; 1976. p. 301-10.

57. Nola G, Vistnes L. Differential response of skin and muscle in the experimental production of pressure sores. Plastic and Reconstructive Surgery 1980;66(5):728-33.

58. Linder-Ganz E, Engelberg S, Scheinowitz M, Gefen A. Pressure–time cell death threshold for albino rat skeletal muscles as related to pressure sore biomechanics. Journal of Biomechanics. 2006;39(14):2725-32.

59. Sanders JE, Goldstein BS, Leotta DF. Skin response to mechanical stress: adaptation rather than breakdown--a review of the literature. Journal of Rehabilitation Research and Development. 1995;32(3):214-26.

60. Chow WW, Odell EI. Deformations and stresses in soft body tissues of a sitting person. Journal of Biomechanical Engineering. 1978;100(2):79-87.

61. Oomens CWJ, Bressers OFJT, Bosboom EMH, Bouten CVC, Bader DL. Can loaded interface characteristics influence strain distributions in muscle adjacent to bony prominences? Computer Methods in Biomechanics & Biomedical Engineering. 2003;6(3):171-80.

62. Reger SI, McGovern TF, Chung KC. Biomechanics of tissue distortion and stiffness by magnetic resonance imaging. In: Bader DL, editor. Pressure Sores: Clinical Practice and Scientific Approach. London: The Macmillan Press; 1990. p. 177-90.

63. Ceelen KK, Stekelenburg A, Loerakker S, Strijkers GJ, Bader DL, Nicolay K, et al. Compression-induced damage and internal tissue strains are related. Journal of biomechanics. 2008;41(16):3399-404.

64. Landis EM. Micro-injection studies of capillary blood pressure in human skin. Heart 1930;15:209-28.

65. McLennan CE, McLennan MT, Landis EM. Effect of external pressure on vascular volume of forearm and its relation to capillary blood pressure and venous pressure. The Journal of Clinical Investigation. 1942;21(3):319-38.

66. Bennett L, Kavner D, Lee BY, Trainor FS, Lewis JM. Skin stress and blood flow in sitting paraplegic patients. Archives of Physical Medicine and Rehabilitation. 1984;65(4):186-90.

67. Manorama AA, Baek S, Vorro J, Sikorskii A, Bush TR. Blood perfusion and transcutaneous oxygen level characterizations in human skin with changes in normal and shear loads — Implications for pressure ulcer formation. Clinical Biomechanics. 2010;25(8):823-8.

68. Brienza DM, Geyer MJ, Jan Y-K. A Comparison of Changes in Rhythms of Sacral Skin Blood Flow in Response to Heating and Indentation. Archives of Physical Medicine and Rehabilitation. 2005;86(6):1245-51.

69. Gefen A. Reswick and Rogers pressure-time curve for pressure ulcer risk. Part 2. Nursing Standard. 2009;23(46):40-4.

70. Fontaine R, Risley S, Castellino R. A quantitative analysis of pressure and shear in the effectiveness of support surfaces. Journal of Wound Ostomy & Continence Nursing. 1998;25(5):233-9.

71. Reger SI, Ranganathan VK, Orsted HL, Ohura T, Gefen A. Shear and Friction in Context. In: MacGregor L, Calne S, editors. Pressure Ulcer Prevention: Pressure, Shear, Friction and Microclimate in Context. London: Wounds International Enterprise House; 2010. p. 11-8.

72. Bennett L, Kavner D, Lee BK, Trainor FA. Shear vs pressure as causative factors in skin blood flow occlusion. Archives of Physical Medicine and Rehabilitation. 1979;60(7):309-14.

73. Linder-Ganz E, Gefen A. The effects of pressure and shear on capillary closure in the microstructure of skeletal muscles. Annals of Biomedical Engineering. 2007;35(12):2095-107.

74. Arthur PG, Giles JJ, Wakeford CM. Protein synthesis during oxygen conformance and severe hypoxia in the mouse muscle cell line C2C12. Biochimica et Biophysica Acta - General Subjects. 2000;1475(1):83-9.

75. Neumayer C, Fügl A, Nanobashvili J, Blumer R, Punz A, Gruber H, et al. Combined enzymatic and antioxidative treatment reduces ischemia-reperfusion injury in rabbit skeletal muscle. Journal of Surgical Research. 2006;133(2):150-8.

76. Tsuji S, Ichioka S, Sekiya N, Nakatsuka T. Analysis of ischemia-reperfusion injury in a microcirculatory model of pressure ulcers. Wound Repair and Regeneration. 2005;13(2):209-15.

77. Kukreja RC, Janin Y. Reperfusion injury: Basic concepts and protection strategies. Journal of Thrombosis and Thrombolysis. 1997;4(1):7-24.

78. Peirce SM, Skalak TC, Rodeheaver GT. Ischemia-reperfusion injury in chronic pressure ulcer formation: A skin model in the rat. Wound Repair and Regeneration. 2000;8(1):68-76.

79. McCord JM. Oxygen-derived radicals: a link between reperfusion injury and inflammation. Federation Proceedings. 1987;46(7):2402-6.

80. Gawlitta D, Li W, Oomens C, Baaijens F, Bader D, Bouten C. The relative contributions of compression and hypoxia to development of muscle tissue damage: an in vitro study. Annals of Biomedical Engineering. 2007;35:273-84.

81. Bouten CVC, Knight MM, Lee DA, Bader DL. Compressive deformation and damage of muscle cell subpopulations in a model system. Annals of Biomedical Engineering. 2001;29(2):153-63.

82. Stekelenburg A, Oomens CWJ, Strijkers GJ, Nicolay K, Bader DL. Compression-induced deep tissue injury examined with magnetic resonance imaging and histology. Journal of Applied Physiology. 2006;100(6):1946-54.

83. Gefen A, Cornelissen LH, Gawlitta D, Bader DL, Oomens CWJ. The free diffusion of macromolecules in tissue-engineered skeletal muscle subjected to large compression strains. Journal of Biomechanics. 2008;41(4):845-53.

84. van Nierop BJ, Stekelenburg A, Loerakker S, Oomens CW, Bader D, Strijkers GJ, et al. Diffusion of water in skeletal muscle tissue is not influenced by compression in a rat model of deep tissue injury. Journal of Biomechanics. 2010;43(3):570 -5.

85. Steinhardt RA. The mechanisms of cell membrane repair. Annals of the New York Academy of Sciences. 2006;1066(1):152-65.

86. Slomka N, Or-Tzadikario S, Sassun D, Gefen A. Membrane-stretch-induced cell death in deep tissue injury: Computer model studies. Cellular and Molecular Bioengineering. 2009;2(1):118-32.

87. Bergstrom N, Braden BJ, Laguzza A, Holman V. The Braden Scale for predicting pressure sore risk. Nursing Research. 1987;36(4):205-10.

88. Tam EW, Mak AF, Lam WN, Evans JH, Chow YY. Pelvic movement and interface pressure distribution during manual wheelchair propulsion. Archives of Physical Medicine and Rehabilitation. 2003;84(10):1466-72.

89. Defloor T, Grypdonck HF. Sitting posture and prevention of pressure ulcers. Applied Nursing Research. 1999;12(3):136-42.

90. National Pressure Ulcer Advisory Panel and European Pressure Ulcer Advisory Panel. Prevention and treatment of pressure ulcers: clinical practice guideline. Washington DC2009.

91. Defloor T, Bacquer D, Grypdonck MHF. The effect of various combinations of turning and pressure reducing devices on the incidence of pressure ulcers. International Journal of Nursing Studies. 2005;42(1):37-46.

92. Thompson G. Softform Premier Active mattress: a novel step-up/step-down approach. British Journal of Nursing. 2006;15(18):988-93.

93. Rithalia SVS, Kenney L. Mattresses and beds: reducing and relieving the pressure. Nursing Times. 2000;96:9-10.

94. National Pressure Ulcer Advisory Panel. Support surface standards initiative. Terms and definitions related to support surface. 2007.

95. Defloor T. The effect of position and mattress on interface pressure. Applied Nursing Research. 2000;13(1):2-11.

96. Defloor T, De Schuijmer JDS. Preventing pressure ulcers: An evaluation of four operating-table mattresses. Applied Nursing Research. 2000;13(3):134-41.

97. Krapfl L, Gray M. Does regular repositioning prevent pressure ulcers? Wound, Ostomy and Continence Nurses Society. 2008;35(6):571-7.

98. Vanderwee K, Grypdonck MHF, De Bacquer D, Defloor T. Effectiveness of turning with unequal time intervals on the incidence of pressure ulcer lesions. Journal of Advanced Nursing. 2007;57(1):59-68.

99. Belkin M, Brown RD, Wright JG, LaMorte WW, Hobson Ii RW. A new quantitative spectrophotometric assay of ischemia-reperfusion injury in skeletal muscle. The American Journal of Surgery. 1988;156(2):83-6.

100. Colin D, Abraham P, Preault L, Bregeon C, Saumet J-L. Comparison of 90[degrees] and 30[degrees] laterally inclined positions in the prevention of pressure ulcers using transcutaneous oxygen and carbon dioxide pressures. Advances in Wound Care. 1996;9(3):35-8.

101. van Geffen P, Reenalda J, Veltink PH, Koopman BFJM. The effects of a dynamic tuberal support on ischial buttock load and pattern of blood supply. IEEE Transactions on Neural Systems and Rehabilitation Engineering. 2010;18(1):29-37.

102. Li ZY, Tam WC, Lau YC, So KF, Wu W, Mak FT. Post pressure response of skin blood flowmotions in anesthetized rats with spinal cord injury. Microvascular Research. 2009;78(1):20-4.

103. Mars M, McKune A, Robbs JV. A comparison of laser doppler fluxmetry and transcutaneous oxygen pressure measurement in the dysvascular patient requiring amputation. European Journal of Vascular and Endovascular Surgery. 1998;16(1):53-8.

104. Nilsson GE, Salerud E.G., Stromberg NOT, Wardell K. Laser Doppler perfusion monitoring and imaging. In: Vo-Dinh IT, editor. Biomedical photonics handbook: CRC Press; 2003. p. 1-24.

105. Vongsavan N, Matthews B. Some aspects of the use of laser Doppler flowmeters for recording tissue blood flow. Experimental Physiology. 1993 January 1, 1993;78(1):1-14.

106. Obeid AN, Barnett NJ, Dougherty G, Ward G. A critical review of laser Doppler flowmetry. Journal of Medical Engineering & Technology. 1990;14(5):178-81.

107. Rajan V, Varghese B, van Leeuwen T, Steenbergen W. Review of methodological developments in laser Doppler flowmetry. Lasers in Medical Science. 2009;24(2):269-83.

108. Dowd G, Linge K, Bentley G. Measurement of transcutaneous oxygen pressure in normal and ischaemic skin. Journal of Bone & Joint Surgery. 1983;65-B(1):79-83.

109. Rithalia SVS. Developments in transcutaneous blood gas monitoring: A review. Journal of Medical Engineering and Technology. 1991;15(4-5):143-53.

110. Coggrave MJ, Rose LS. A specialist seating assessment clinic: changing pressure relief practice. Spinal Cord. 2003;41(12):692-5.

111. Feather JW, Hajizadeh-Saffar M, Leslie G, Dawson JB. A portable scanning reflectance spectrophotometer using visible wavelengths for the rapid measurement of skin pigments. Physics in Medicine and Biology. 1989;34(7):807-20.

112. Hagisawa S, Ferguson-Pell M, Cardi M, Miller SD. Assessment of skin blood content and oxygenation in spinal cord injured subjects during reactive hyperemia. Journal of Rehabilitation Research and Development. 1994;31(1):1-14.

113. Sprigle S, Linden M, Riordan B. Characterizing reactive hyperemia via tissue reflectance spectroscopy in response to an ischemic load across gender, age, skin pigmentation and diabetes. Medical Engineering and Physics. 2002;24(10):651-61.

114. Feather JW, Hajizadeh-Saffar M, Leslie G, Dawson JB. A portable scanning reflectance spectrophotometer using visible wavelengths for the rapid measurement of skin pigments. Physics in Medicine and Biology. 1989;34(7):807-20.

115. Moan J. Visible light and UV radiation. In: Brune D, Hellborg R, Persson BRR, Pääkkönen R, editors. Radiation at home, outdoors and in the workplace. Oslo: Scandinavian Science Publisher; 2001. p. 69-85.

116. Beer. Determination of the absorption of red light in colored liquids. Annalen der Physik und Chemie. 1852;86:78-88.

117. Cope M. The application of near infrared spectroscopy to non invasive monitoring of cerebral oxygenation in the newborn infant [PhD thesis]. London: The University of London; 1991.

118. van de Hulst HC. Light scattering by small particles. New York: Wiley & Sons; 1957.

119. Cheong WF, Prahl SA, Welch AJ. A review of the optical properties of biological tissues. IEEE Journal of Quantum Electronics. 1990;26(12):2166-85.

120. Gurnani PP. Near Infrared spectroscopic measurement of human and animal brain structures. Arlington: The University of Texas; 2003.

121. Jacques SL, Prahl SA. Reduced scattering coefficient. Notes on the Tissue Optics. Oregon 1998.

122. Jobsis F. Noninvasive, infrared monitoring of cerebral and myocardial oxygen sufficiency and circulatory parameters. Science. 1977;198(4323):1264-7.

123. Delpy DT, Cope M. Quantification in tissue near–infrared spectroscopy. Philosophical Transactions of the Royal Society of London Series B: Biological Sciences. 1997;352(1354):649-59.

124. Delpy DT, Cope M, Zee Pvd, Arridge S, Wray S, Wyatt J. Estimation of optical pathlength through tissue from direct time of flight measurement. Physics in Medicine and Biology. 1988;33(12):1433-42.

125. Fishkin JB, Gratton E. Propagation of photon-density waves in strongly scattering media containing an absorbing semi-infinite plane bounded by a straight edge. Journal of the Optical Society of America A. 1993;10(1):127-40.

126. Weiss GH, Nossal R, Bonner RF. Statistics of penetration depth of photons re-emitted from irradiated tissue. Journal of Modern Optics. 1989;36(3):349-59.

127. Cui W, Kumar C, Chance B. Experimental study of migration depth for the photons measured at sample surface. Proceedings of SPIE 1991;1431:180-91.

128. Stratonnikov A. Evaluation of blood oxygen saturation in vivo from diffuse reflectance spectra. Journal of Biomedical Optics. 2001;6(4):457-67.

129. Feng S, Zeng F, Chance B. Monte Carlo simulations of photon migration path distributions in multiple scattering media. Proceedings of SPIE. 1993;1888(1):78-89.

130. Meglinsky I, Matcher S. Modelling the sampling volume for skin blood oxygenation measurements. Medical and Biological Engineering and Computing. 2001;39(1):44-50.

131. Meglinskiĭ I, Matcher S. Analysis of the spatial distribution of detector sensitivity in a multilayer randomly inhomogeneous medium with strong light scattering and absorption by the Monte Carlo method. Optics and Spectroscopy. 2001;91(4):654-9.

132. Murkin JM, Arango M. Near-infrared spectroscopy as an index of brain and tissue oxygenation. British Journal of Anaesthesia. 2009;103(suppl 1):i3-i13.

133. Rolfe P. In vivo near-infrared spectroscopy. Annual Review of Biomedical Engineering. 2000:715-54.

134. Millington PF, Wilkinson R, editors. Skin: Cambridge University Press; 1983.

135. Laurent A, Mistretta F, Bottigioli D, Dahel K, Goujon C, Nicolas JF, et al. Echographic measurement of skin thickness in adults by high frequency ultrasound to assess the appropriate microneedle length for intradermal delivery of vaccines. Vaccine. 2007;25(34):6423-30.

136. Bozkurt A, Rosen A, Rosen H, Onaral B. A portable near infrared spectroscopy system for bedside monitoring of newborn brain. BioMedical Engineering OnLine. 2005;4(1):29-39.

137. Suzuki S, Takasaki S, Ozaki T, Kobayashi Y. A tissue oxygenation monitor using NIR spatially resolved spectroscopy. Proceedings of SPIE. 1999;3597:582-92.

138. Wagnières G, Cheng S, Zellweger M, Utke N, Braichotte D, Ballini JP, et al. An optical phantom with tissue-like properties in the visible for use in PDT and fluorescence spectroscopy. Physics in Medicine and Biology. 1997;42(7):1415-26.

139. Firbank M, Delpy DT. A design for a stable and reproducible phantom for use in near infra-red imaging and spectroscopy. Physics in Medicine and Biology. 1993;38(6):847-53.

140. Pogue B. Review of tissue simulating phantoms for optical spectroscopy, imaging and dosimetry. Journal of Biomedical Optics. 2006;11(4):1-16.

141. Rinaldo C, Antonio P, Paola T, Alessandro T, Gianluca V. A solid tissue phantom for photon migration studies. Physics in Medicine and Biology. 1997;42(10):1971-9.

142. Andreea D, Jarod CF, Timothy CZ. A method for determination of the absorption and scattering properties interstitially in turbid media. Physics in Medicine and Biology. 2005;50(10):2291-311.

143. van Staveren HJ, Moes CJM, van Marie J, Prahl SA, van Gemert MJC. Light scattering in Intralipid-10% in the wavelength range of 400 to 1100 nm. Applied Optics. 1991;30(31):4507-14.

144. Hunter RJ, Patterson MS, Farrell TJ, Hayward JE. Haemoglobin oxygenation of a two-layer tissue-simulating phantom from time-resolved reflectance: effect of top layer thickness. Physics in Medicine and Biology. 2002;47(2):193-208.

145. Cook JR, Bouchard RR, Emelianov SY. Tissue-mimicking phantoms for photoacoustic and ultrasonic imaging. Biomedical Optical Express. 2011;2(11):3193-206.

146. Irwin D, Dong L, Shang Y, Cheng R, Kudrimoti M, Stevens SD, et al. Influences of tissue absorption and scattering on diffuse correlation spectroscopy blood flow measurements. Biomedical Optical Express. 2011;2(7):1969-85.

147. Mayrovitz, Macdonald, Smith. Blood perfusion hyperaemia in response to graded loading of human heels assessed by laser-Doppler imaging. Clinical Physiology. 1999;19(5):351-9.

148. Tam EW. Response of Tissue to dynamic loading durign wheelchair propulsion: an investigation on the etiology of pressure sores [PhD thesis]. Hong Kong: Hong Kong Polytechnic University; 2002.

149. Hamaoka T, Osada T, Murase N, Sako T, Higuchi T, Kurosawa Y, et al. Quantitative Evaluation of OXygenation and Metabollsm in the Human Skeletal Muscle. Optical Review. 2003;10(5):493-7.

150. Martini FH. Fundamentals of Anatomy and Physiology: San Francisco: Benjamin Cummings; 2006.

151. Komiyama T, Quaresima V, Shigematsu H, Ferrari M. Comparison of two spatially resolved near-infrared photometers in the detection of tissue oxygen saturation: poor reliability at very low oxygen saturation. Clinical Science. 2001;101(6):715-8.

152. Linder-Ganz E, Shabshin N, Itzchak Y, Yizhar Z, Siev-Ner I, Gefen A. Strains and stresses in sub-dermal tissues of the buttocks are greater in paraplegics than in healthy during sitting. Journal of Biomechanics. 2008;41(3):567-80.

153. Tam WC, Kam LM, Cheung CH. Design of pressure relief Cushions [unpublished work]. 2003.

154. Letokhov VS. Laser Light in Biomedicine and the Life Sciences: From the Present to the Future. In: Vo-Dinh IT, editor. Biomedical Photonics Handbook: Boca Raton, Fla. : CRC Press; 2003.

155. Madsen SJ, Patterson MS, Wilson BC. The use of India ink as an optical absorber in tissue-simulating phantoms. Physics in Medicine and Biology. 1992;37(4):985-93.

156. Marrone A, Ballantyne J. Changes in dry state hemoglobin over time do not increase the potential for oxidative DNA damage in dried blood. PLoS ONE. 2009;4(4):e5110.

157. Sukowski U, Schubert F, Grosenick D, Rinneberg H. Preparation of solid phantoms with defined scattering and absorption properties for optical tomography. Physics in Medicine and Biology. 1996;41(9):1823-44.

158. Muraki S, Fornusek C, Raymond J, Davis GM. Muscle oxygenation during prolonged electrical stimulation-evoked cycling in paraplegics. Applied Physiology, Nutrition, and Metabolism. 2007;32(3):463-72.

159. Aldayel A, Muthalib M, Jubeau M, McGuigan M, Nosaka K. Muscle oxygenation of vastus lateralis and medialis muscles during alternating and pulsed current electrical stimulation. European Journal of Applied Physiology. 2011;111(5):779-87.

160. Leung TS, Wittekind A, Binzoni T, Beneke R, Cooper CE, Elwell CE. Muscle oxygen saturation measured using “cyclic NIR signals” during exercise. In: Takahashi E, Bruley DF, editors. Advances in Experimental Medicine and Biology: Oxygen Transport to Tissue XXXI: Springer US; 2010. p. 183-9.